REPORT DOCUMENTATION PAGE

Form Approved OMB NO. 0704-0188

1. REPORT DATE (DD-MM-YYYY)	2. REPORT TYPE	3. DATES COVERED (From - To)
22-10-2014	Ph.D. Dissertation	-

4. TITLE AND SUBTITLE
Micro-Magnetic Structures for Biological Applications

5a. CONTRACT NUMBER
W911NF-10-1-0353

5b. GRANT NUMBER

5c. PROGRAM ELEMENT NUMBER
611102

6. AUTHORS
Marci Howdyshell

5d. PROJECT NUMBER

5e. TASK NUMBER

5f. WORK UNIT NUMBER

7. PERFORMING ORGANIZATION NAMES AND ADDRESSES
Ohio State University
1960 Kenny Road

Columbus, OH 43210 -1016

8. PERFORMING ORGANIZATION REPORT NUMBER

9. SPONSORING/MONITORING AGENCY NAME(S) AND ADDRESS (ES)
U.S. Army Research Office
P.O. Box 12211
Research Triangle Park, NC 27709-2211

10. SPONSOR/MONITOR'S ACRONYM(S)
ARO

11. SPONSOR/MONITOR'S REPORT NUMBER(S)
56755-MS.19

12. DISTRIBUTION AVAILIBILITY STATEMENT
Approved for public release; distribution is unlimited.

13. SUPPLEMENTARY NOTES
The views, opinions and/or findings contained in this report are those of the author(s) and should not contrued as an official Department of the Army position, policy or decision, unless so designated by other documentation.

14. ABSTRACT
Developments in single-molecule and single-cell experiments over the past century have provided researchers with many tools to probe cellular response to stresses such as physical force or to the injection of foreign genes. Often these techniques target the cell membrane, although many are now advancing to probe within the cell. As these techniques are improved upon and investigations advance toward clinical studies, it has become more critical to achieve high-throughput outcomes which in turn lead to statistically significant results. The technologies developed in this thesis are targeted at transfecting large populations of cells with controlled doses of specific exogenic

15. SUBJECT TERMS
electroporation, magnetic tweezers, gene delivery

16. SECURITY CLASSIFICATION OF:			17. LIMITATION OF ABSTRACT	15. NUMBER OF PAGES	19a. NAME OF RESPONSIBLE PERSON
a. REPORT	b. ABSTRACT	c. THIS PAGE			R. Soorya kumar
UU	UU	UU	UU		19b. TELEPHONE NUMBER 614-292-3130

Report Title

Micro-Magnetic Structures for Biological Applications

ABSTRACT

Developments in single-molecule and single-cell experiments over the past century have provided researchers with many tools to probe cellular response to stresses such as physical force or to the injection of foreign genes. Often these techniques target the cell membrane, although many are now advancing to probe within the cell. As these techniques are improved upon and investigations advance toward clinical studies, it has become more critical to achieve high-throughput outcomes which in turn lead to statistically significant results. The technologies developed in this thesis are targeted at transfecting large populations of cells with controlled doses of specific exogenic material without adversely affecting cell viability. Underlying this effort is a platform of lithographically patterned ferromagnetic thin films capable of remotely manipulating and localizing magnetic microbeads attached to biological entities. A novel feature of this approach, as demonstrated here with both DNA and cells, is the opportunity for multiplexed operations on targeted biological specimens. This thesis includes two main thrusts: (1) the advancement of the trapping platforms through experimental verification of mathematical models providing the energy landscapes associated with the traps and (2) implementation of the platform as a basis for rapid and effective high-throughput microchannel and nanochannel cell electroporation devices. The electroporation devices have, in our studies, not only demonstrated to sustain cell viability with extremely low cell mortality rates, but are also found to be effective for various types of cells. The advances over current electroporation technologies that are achieved in these efforts demonstrate the potential for detection of mRNA expression in heterogeneous cell populations and probing intracellular responses to the introduction of foreign gene into cells.

Micro-magnetic Structures for Biological Applications

DISSERTATION

Presented in Partial Fulfillment of the Requirements for the Degree Doctor of Philosophy in the Graduate School of The Ohio State University

By

Marci L. Howdyshell, M.S., B.A.

Graduate Program in Physics

The Ohio State University

2014

Dissertation Committee:

Professor R. Sooryakumar, Advisor

Professor C. Jayaprakash

Professor M. Poirier

Professor K. Honscheid

Abstract

Developments in single-molecule and single-cell experiments over the past century have provided researchers with many tools to probe the responses of cells to stresses such as physical force or to the injection of foreign genes. Often these techniques target the cell membrane, although many are now advancing to probe within the cell. As these techniques are improved upon and the investigations advance toward clinical applications, it has become more critical to achieve high-throughput outcomes which in turn lead to statistically significant results. The technologies developed in this thesis are targeted at transfecting large populations of cells with controlled doses of specific exogenic material without adversely affecting cell viability. Underlying this effort is a platform of lithographically patterned ferromagnetic thin films capable of remotely manipulating and localizing magnetic microbeads attached to biological entities. A novel feature of this approach, as demonstrated here with both DNA and cells, is the opportunity for multiplexed operations on targeted biological specimens. This thesis includes two main thrusts: (1) the advancement of the trapping platforms through experimental verification of mathematical models providing the energy landscapes associated with the traps and (2) implementation of the platform as a basis for rapid and effective high-throughput microchannel and nanochannel cell electroporation devices. The electroporation devices have, in our studies, not only been demonstrated to sustain cell viability with extremely low cell mortality rates, but are also found to be effective for various types of cells. The advances over current electroporation technologies that are achieved in these efforts demonstrate the potential for detection of mRNA expression in heterogeneous cell populations and probing intracellular responses to the introduction of foreign genes into cells.

This document is dedicated to my family. To my parents, Sharon and Dennis Howdyshell, my sisters, Leah and Kristin Howdyshell, and my grandfather, Alvin C. Howdyshell for their loving support. In loving memory of Grandma Patricia J. Swain, Grandma Mary Ellen Howdyshell, Grandma Helen Vietzen Howdyshell, and Grandpa Kenneth C. Swain. Finally, to the large extended family who are too numerous to name.

Acknowledgments

There are many, many people I would like to acknowledge for the help provided during graduate school. First, I would like to thank my advisor, Dr. Sooryakumar, for his support, encouragement, and sound advice he has given during the five years I have been in his lab. I would also like to thank the other members of my committee, Dr. Jayaprakash, Dr. Poirier, and Dr. Honscheid. Thank you also to the faculty members at Ohio State with whom we have collaborated, who have been extremely supportive and helpful, including Dr. L. J. Lee, Dr. Brian Lower, Dr. Steven Lower, and Dr. Jeffrey Chalmers.

I'd also like to thank my undergraduate professors, without whom I may never have pursued physics, let alone graduate school. Thank you to Dr. David Seely, Dr. Aaron Miller, Dr. Nicolle Zellner, Dr. Charles Moreau, and Dr. David Anderson. Thank you also to Dr. Bridget Ingham, my mentor during my summer internship at SLAC. I truly appreciate the guidance and support provided as I pursued of my bachelor's degree, my first research experiences, and graduate school applications.

I'd like to thank all of the graduate students, postdocs, undergraduates, and high school students that I have collaborated with on research projects during graduate school, including Dr. Greg Vieira, Dr. Aaron Chen, Mike Prikockis, Lingqian Chang, Stephanie Lauback, Dr. Daniel Gallego-Perez, Xi Zhao, Kylienne Clark, Carrie Gerding, Dr. Marek Šimon, Dr. Justin North, Kyoung-Joo Jenny Park, Yongqi Wu, Dr. Veysi Malkoc, Christopher Pease, Chris Pierce, George Vogt, Tom Byvank, Sam Stuard, Anand Harvind, Paul Zivick, Tom Henighan, Manjari Randeria, Bavi Sadayappan, Mudd Hussain, Dan Giglio, Eric Suchyta, Cherry Gupta, Jeremiah Shley, and Mike Hudoba. Jon Zizka, it was great having you on the "other side" of the lab!

Thank you to the staff members who have trained me on equipment and helped create the parts necessary for experiments, including Tom Kelch, Peter Janney, Derek Ditmer, Paul Steffen, Denis Pelekov, Pete Gosser, and Jon Shover. Thank you also to Theresa Gordon, Kris Dunlap, Trisch Longbrake, and Layla Mohmmad-Ali.

Outside of research, a very special thank you to Dr. Nandini Trivedi, Michelle McCombs, Theresa Barber, Marisa Mulac, and Alex Reed. It was a pleasure working with you all and truly awesome to see Scientific Thinkers take shape! Thank you to Dr. Susan Olesik and all those working at the Ohio House of Science and Engineering—Rocquel Walker, Dr. Sevinc Erdal, and Mirella Harrington—for helping us along the way.

Thanks to all the members of the Association for Women in Science, especially Komal Rombani, Richelle Teeling-Smith, Aleya Dhanji, Jessica Rakijas, Toni Newsome, and Serena Chang, and to the members of the Graduate Women in Physics group.

Thank you to all the friends who have supported me during graduate school. In particular, "The M's," Marissa Rodenburg and Morgan Welsh Bernier, who have been there from the beginning. I'm so lucky to have had your company for everything from working on Jackson problems to crafting and running! Most importantly, thank you so much for the moral support. Christopher Wolfe, thank you so much for your love and support (and for putting up with all of the conversations about electroporation lately)!

Grant funding was provided by the U.S. Army Research Office under Contract W911NF-10-1-053 and in part by the National Science Foundation under grant EEC-0914790.

Vita

2011.....M.S., The Ohio State University, *Physics*
2008.....B.A., Albion College, *Major: Physics, Spanish; Minor: Applied Mathematics*
2004.....Notre Dame Preparatory High School

Awards

2012.....Bunny Clark Scholarship
Mar 2011, Nov 2011, Mar 2013 .....Ray Travel Award
2009.....Hazel Brown Outstanding Teaching Award

Publications

M. L. Howdyshell, M. Prikockis, S. Lauback, G. B. Vieira, K. Mahajan, J. Winter, and R. Sooryakumar. "Deterministic and stochastic trajectories of magnetic particles: Mapping energy landscapes for technology and biology." *IEEE Transactions on Magnetics*, Accepted for publication, May 2014.

A. Chen, G. Vieira, T. Henighan, M. Howdyshell, J. A. North, A. J. Hauser, F. Y. Yang, M. G. Poirier, C. Jayaprakash, and R. Sooryakumar. "Regulating Brownian fluctuations with tunable microscopic magnetic traps." *Physical Review Letters* **107**, 087206 (2011).

B. Ingham, B. N. Illy, M. F. Toney, M. Howdyshell, and M. P. Ryan. "In situ synchrotron X-ray diffraction experiments on electrochemically deposited ZnO nanostructures." *The Journal of Physical Chemistry C*, **112**, 14863-14866 (2008)

Conference Presentations

Scientific Thinkers at Innis Elementary The Second Annual Ohio State University Outreach and Engagement Forum, 2014.

M. Howdyshell, D. Gallego-Perez, G. Vieira, V. Malkoc, L. J. Lee, R. Sooryakumar. *High*

throughput transfection of cells: nano-electroporation and mobile magnetic traps. APS March Meeting 2014, Denver, Colorado. Abstract Q45.00004.

M. Howdyshell, G. Vieira, D. Gallego-Perez, X. Zhao, L. J. Lee and R. Sooryakumar. *Multiplexing nano-electroporation for simultaneous transfection of multiple cells.*APS March Meeting 2013, Baltimore, Maryland. Abstract M46.00002.

M. Howdyshell, D. Gallego-Perez, G. Vieira, X. Zhao, R. Sooryakumar, and L. J. Lee. *High-throughput nanoelectroporation for simultaneous transfection of multiple cells.* Poster, Ohio State University Materials Week, 2013.

M. Howdyshell, M. Šimon, M. Poirier, and R. Sooryakumar. *Dual microbead-labeled DNA manipulation with magnetic traps in a microfluidic device.* APS March Meeting 2012, Boston, Massachusetts. Abstract D9.00001.

M. Howdyshell, G. Vieira, A. Chen, M. Šimon, M. Poirier, R. Sooryakumar. *Forces due to patterned magnetic traps within microfluidic channels.* APS March Meeting 2011, Dallas, Texas. Abstract W19.00008.

Science Fellows Supporting Elementary School Teachers (SFST): The Ohio State University GK-12 Program, Annual Conference for Graduate STEM Fellows in K-12 Education 2010, Washington, D.C.

Fields of Study

Major Field: Physics

Table of Contents

List of Figures

List of Tables

Chapter 1
Introduction

Motivated by a drive to better understand the human cell and its components, there are many techniques that have been developed and modified over the past several decades for manipulating, localizing, and performing in vitro measurements on biological materials such as cells, proteins, and DNA. These techniques allow for careful single-molecule experiments to be performed on micrometer- or nanometer-sized biological entities and have been at the forefront of answering basic questions about structure and function of cellular components [1]. Single-cell and single-molecule manipulation techniques include micropipettes [2, 3, 4], optical tweezers [5, 6, 7], and conventional magnetic tweezers [8, 9, 10, 11], among others. Each of these techniques offers the ability to localize and manipulate individual cells or molecules for careful studies of properties such as elastic properties [10, 11, 12] and response to externally applied stresses [4, 13].

Development of these individual techniques has been accompanied by an expansion in applications; in particular, single-molecule techniques have been incorporated into complex biomedical devices capable of sorting [14, 15, 16, 17], transfecting [6, 18, 19, 20], and performing measurements and other analyses [21, 22, 23] on biological entities. This expansion into the realm of clinical studies necessitates more statistically significant experiments to complement single-cell and single molecule studies. To do so, these applications must be scaled up to efficiently multiplex experiments without compromising individual control on each entity.

In this thesis, a previously developed series of magnetic disk and zigzag wire micromagnetic traps, or magnetic tweezers [24, 25, 26], will be presented as a basis for multiplexing

various biological experiments. This technology is capable of precisely localizing and manipulating magnetic objects of micrometer or nanometer scale, accompanied with real-time microscope imaging. The device has been previously shown to be capable of single-cell experiments [24, 25]. However, an important advantage of this magnetic platform over other techniques is that the traps are fabricated using lithography and may be easily scaled up. The number of patterned magnetic traps is limited in size only by the wafer onto which they are patterned. To demonstrate that effective multiplexing is readily accessible with magnetically labeled biomolecules, multiplexed DNA stretching experiments are demonstrated in Chapter 4. Magnetic-tweezers based multiplexing is also demonstrated with magnetically labeled cells in Chapter 6.

Because weak (<200 Oe) magnetic fields are used to control the magnetic tweezers platform, there should be no damage to biological material. However, an understanding of the forces applied to molecules is important both to ensure viability of molecules studied and to know the limitations of the platform (i.e which force regimes may be accessed). Previous studies [24, 25] rely primarily on mathematical modeling to estimate the forces applied by the magnetic traps. Advancing this technology to more precise biological manipulation experiments, however, requires a careful experimental verification of these mathematical models. In Chapter 5, quantitative analysis of the motion of superparamagnetic microbeads during magnetically actuated travel from one vertex to the next on the zigzag wire traps provides an experimental analysis of the potential energy landscape and subsequent forces along the trajectory. This was accompanied by a similar qualitative analysis using Janus-type beads (see Chapter 2 and Chapter 5) to understand the complete motion of the microbeads during these trajectories. The force values determined in these experiments agree with preliminary force calculation results from DNA experiments in Chapter 4.

The final application of the magnetic tweezers platform presented in this thesis is in devices aimed at probing the interior of cells, a recent advance in cell manipulation technologies [6, 27, 28, 29]. While studies of cell populations and single-cell studies of cell membranes provide much insight into cellular responses to external factors, such studies

fail to give a complete picture of internal and external cell activity. They must therefore be complemented with an experimental analysis of intracellular response that specifically probes the cell interior. For example, fluorescent nanoparticle tracking inside living cells [30] has been used to compare the internal structure of the cytoskeleton of metastatic cancer cells to that of noncancerous cells and complements previous studies on cell membrane rigidity [31]. Additionally, intracellular studies on live cells are important for determining behaviour and functionality of components such as proteins and enzymes, differentiating the behavior of purified proteins from that of proteins inside live cells [32]. Intracellular studies have progressed significantly in the past two decades with the introduction of molecular beacons [33], which fluoresce only when hybridized to targeted structures. Molecular beacons are capable of detecting targeted messenger RNA (mRNA) populations inside the cell [34, 35] to differentiate heterogeneous cell populations based on expression of different molecules within the cytosol.

Accessing intracellular components provides new challenges for cell probing technologies. In addition to carefully controlling applied forces, it is necessary to penetrate the protective phospholipid bilayer cell membrane without causing long-term damage. One widely studied technology capable of targeting the interior of the cell is transfection, the introduction of foreign genes into the cell. Electroporation, which transfects cells using controlled voltage pulses that reversibly porate the cell membrane, is a rapidly developing method of transfection [36, 37]. Both single-cell [38, 39, 40] and high-throughput [36] electroporation technologies have been developed. Single-cell technologies, which may be capable of precise delivery [18], are limited by their low-throughput nature. However, current high throughput techniques are limited by a lack of dosage control and high cell mortality rates [41].

In chapter 6, the magnetic disk traps are implemented as a foundation for microchannel and nanochannel electroporation technologies. A large arrayed magnetic tweezer platform is paired with previously developed technologies [18] to manipulate and localize cells for precise electroporation, thus advancing the electroporation technologies to be more high throughput without sacrificing cell viability or transfection efficiency. In particular, the magnetic tweezers-based 3D microchannel electroporation device presented is capable of

simultaneously transfecting on the order of 10^4 cells/cm^2 with >90% cell viability [42]. In this device, we transfect targeted molecular beacons into cells to demonstrate distinction of different cell populations by detection of GATA2 mRNA levels.

Chapter 2
Experimental Methods

2.1 Micro-scale manipulation techniques for biological materials

Before discussing the zigzag wire and magnetic disk trap-based magnetic tweezers, a few current technologies in cellular and biomolecule manipulation and localization will be briefly discussed.

2.1.1 Microfluidics

In the field of biotechnology, microfluidics are often integrated into devices because biological materials such as cells and DNA must remain in solution. While most microfluidic devices integrate one or more other techniques as well [2], several rely on microfluidics alone to manipulate and study cells. These techniques utilize carefully controlled fluid flow rates to maneuver targeted objects through specially designed channels. For example, microfluidic sorting devices are capable of selectively sorting and/or localizing specific cells based on immunocytochemical targeting of cell membrane receptors [43] or on physical features such as cell stiffness [44] or cell size [45]. Microfluidic devices are also capable of analyzing membrane response to external stresses applied by fluids in the channel [46].

2.1.2 Micropipettes

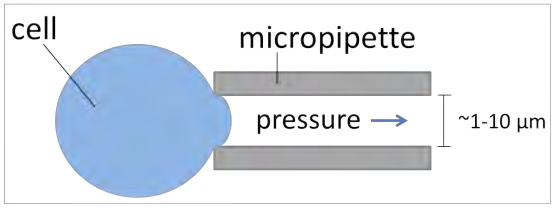

Figure 2.1: Micropipette aspiration. A negative pressure is applied to a small area of a cell membrane (as determined by the diameter of the micropipette, usually 1-10 μm) to localize or deform the cell.

A micropipette is a tool that can be used to isolate a single biological entity (usually a cell) approximately micrometers in dimension for localization or manipulation [2, 3]. The micropipette itself is a thin glass capillary with a tip diameter on the order of micrometers (Figure 2.1) capable of applying a negative pressure onto the cell. The applied force is tunable in the range of approximately 10 to 10^3 pN, resulting in pressures of ∼1-1,000 Pa [4]. Although a weak pressure (1 Pa) will suffice to localize and manipulate cells, a higher pressure (1,000 Pa) will further aspirate the cell into the pipette. This is desireable in some circumstances because a quantitative study of the deformation of the cell membrane during aspiration allows for characterization of the membrane response to stresses [2, 4].

Although biomolecules such as DNA and proteins are too tiny to be individually manipulated by micropipettes, any molecule that can be attached to a microbead can be manipulated or localized with micropipettes [7]. Additionally, studies in the past decade have produced functional nanopipettes [27, 28], which offer promise of more precise applications by targetting smaller sized objects.

Micropipettes have also been successfully utilized to hold a cell in place during microinjection (see Chapter 6) for in vitro fertilization, gene therapy, and other dosage-controlled injection techniques [6]. However, micropipettes require a skilled user [4] and are difficult to integrate into a standard microfluidic channel because the pipette itself must extend into the fluidic environment [7]. Another drawback of micropipettes is that they are limited to single-cell experiments. Furthermore, the physical nature of micropipette aspiration makes it potentially harmful to the cell memrane [4].

2.1.3 Optical tweezers

Another technique that, like micropipette manipulation, is generally limited to single-cell or single-molecule manipulations is optical tweezers. Unlike micropipettes, optical tweezers are contact-free, with all manipulation controlled by a laser beam. Microfluidic channels are often made of glass or quartz surfaces and with features molded into polydimethylsiloxane (PDMS, see Chapter 2), all of which are optically transparent and thus readily integrable into optical tweezer setups.

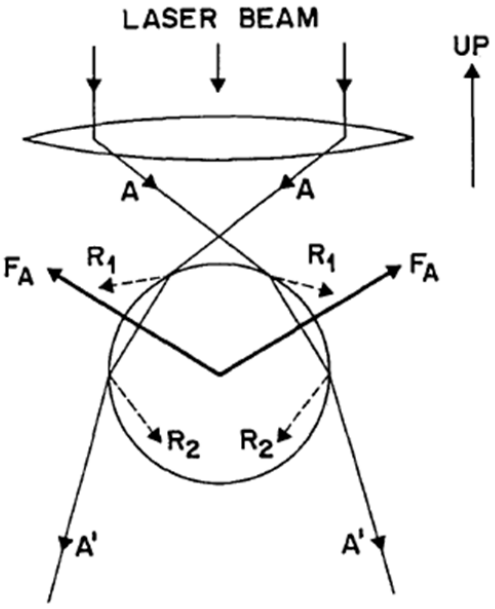

Figure 2.2: Optical tweezers. Two rays (A) from a laser are traced for a spherical microbead of approximately 10 μm diameter. The rays are refracted and upon exiting the bead, emergent rays (A') transfer momentum to the bead. Surface reflections (R) also contribute to scattering. The net force (F) on the bead will be toward the beam focus. Image from Ashkin et al, *Optics Letters*, 1986.

The basic principal of optical trapping for a cell or dielectric particle ($\sim$10 μm) is shown in Figure 2.2. A highly focused laser beam near the dielectric sphere will exert a gradient force on the bead, pushing it toward the highest intensity at the center of the beam [5]. This force is primarily due to refraction of the light rays through the bead [47] (see emergent rays A' in Fig. 2.2).

The forces applied by optical tweezers may be used to very precisely manipulate and localize cells or biomolecules attached to polystyrene microbeads, though the throughput is limited. Another drawback of optical tweezers is the potential damage caused to cells by heating from the laser beam.

2.1.4 Conventional magnetic tweezers

The term "conventional magnetic tweezers" generally applies to an experimental method that utilizes the magnetic field gradient from a permanent magnet to apply a force (generally from 1 - 1,000 pN) onto a magnetic microbead attached to a biomolecule [8, 9] or cell membrane [13]. The the other end of the strand of DNA or cell is often attached to a suface.

The schematic of Figure 2.3 shows the basic setup, where the macroscopic permanent magnet is held at some distance from the substrate. Adjusting the distance between the magnet and the microbead will adjust the gradient. A tapered tip at one pole of the permanent magnet increases the magnetic field gradient near the tip and potentially allows the tip to be closer to the magentic bead(s), resulting in stronger magnetic forces [13]. One major limitation of conventional magnetic tweezers is that they are limited to one small region in which they may perform experiments.

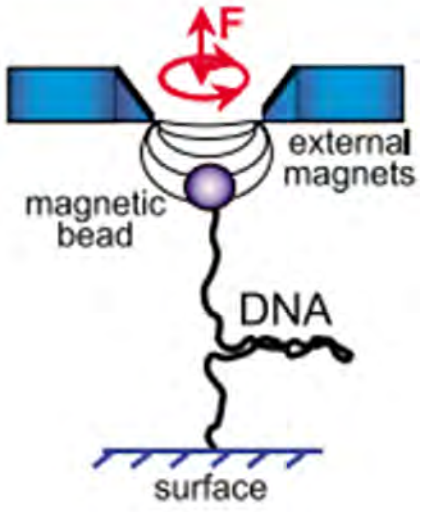

Figure 2.3: Conventional magnetic tweezers. Permanent magnets are held above the sample to induce a magnetic moment in a superparamagnetic microbead attached to a biomolecule. The magnets may be moved vertically or rotated to apply a force or torque to the bead and biomolecule. Image from Zlatanova et al, *Biochemistry and Cell Biology*, 2003.

2.2 Magnetic disk and zigzag wire traps: structure and fabrication

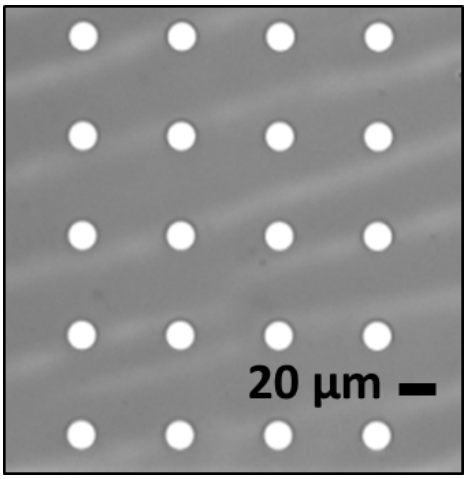

Figure 2.4: An array of permalloy magnetic disk traps patterned onto a silicon wafer.

The traps used in the experiments presented in this thesis are previously developed magnetic thin film-based trapping structures [24, 25, 48]. Thin film-based surface traps such as these and similar designs have been utilized in the past for their capabilities to trap and transport superparamagnetic microbeads [49, 50, 51, 52, 53, 54].

2.2.1 Magnetic disk traps

Magnetic disk traps (Figure 2.4) are fabricated on silicon, quartz, or glass wafers with basic cleanroom photolithography techniques. After solvent-based cleaning and a 5 minute bake (115^{o}C) to

dry, the wafers are spin coated (CE 100CB Resist Coater and Hot Plate) with two layers of positive photoresist: first LOR2A (3,000 rpm, 10,000 rpm/s, 60 s; 2 minute 190^{o}C bake) and then S1813 (500 rpm, 300 rpm/s, 5 s; 3,000 rpm, 10,000 rpm/s, 45 s; 60-90s 115^{o}C bake). An aligner (EV Group 620 Advanced Contact Aligner) is used to expose ultraviolet light through a pre-designed mask (hard contact mode, exposure time 3.5 s). Development with Microposit^{TM} MF^{TM}-319 developer for 45 s with gentle agitation removes photoresist in disk regions.

After developing the sample, 50-60 nm of permalloy ($Ni_{0.81}Fe_{0.19}$) is sputtered (AJA Orion RF/DC Sputter Deposition Tool, DC, Ar 20 sccm, 3 mTorr, 200 W) onto the surface of a silicon wafer. However, if quartz or glass wafers are used, a 2 nm seed layer of titanium (RF, Ar 20 sccm, 3 mTorr, 300 W) is deposited prior to the permalloy to assist with adhesion. N-Methyl-2-Pyrrolidone (NMP) is used for a ∼20 minute lift-off, which removes the remainder of the photoresist as well as any sputtered material on it, leaving only permalloy disks on the surface.

A 100 - 500 nm SiO_2 layer can then be deposited with Silicafilm (Emulsitone) using a spin-coater (3,000 rpm, 5,000 rpm/s, 60 s) followed by a 15 minute 180^{o}C bake with 5 minute gradual cool-down

2.2.2 Zigzag wire traps

$Co_{0.5}Fe_{0.5}$ wires are patterned onto a silicon wafer using electron beam lithography. After sonicating in acetone and isopropanol for 2-3 minutes each, the silicon wafer is placed into the UV-Ozone cleaner (UVO Cleaner 42, Jelight Company Inc, see "Nonspecific binding and surface treatments" section in this chapter) for 20 minutes. Two e-beam resists are then spin-coated onto the wafer. First MMA (methyl methacrylate, 4500 rpm, 60 s) is spun on, followed by a 60-90 s bake at 180^{o}C, then PMMA (plymethyl methacrylate, 4500 rpm, 60 s), followed by another 60-90 s bake at 180^{o}C.

Electron beam lithography is used to pattern the zigzag wires onto the resist. Then a 1:2 ratio mixture of MIBK and Isopropanol is used to develop for 45 s with gentle agitation. Sputter deposition of the $Co_{0.5}Fe_{0.5}$ wires is followed by lift-off with acetone. The surface is

coated in a 100 - 500 nm protective layer of Silicafilm as described in the previous section for magnetic disk traps.

Wires are initially magnetized (perpendicular to the length of the wire) by a momentary 1 Tesla field (Figure 2.5 (a)) that leads to either a head-to-head (HH) or tail-to-tail (TT) domain wall at each vertex (Figure 2.5 (b)) and generation of a field $\mathbf{H}_{dw}$ [24] as will be discussed in Chapters 3 and 4.

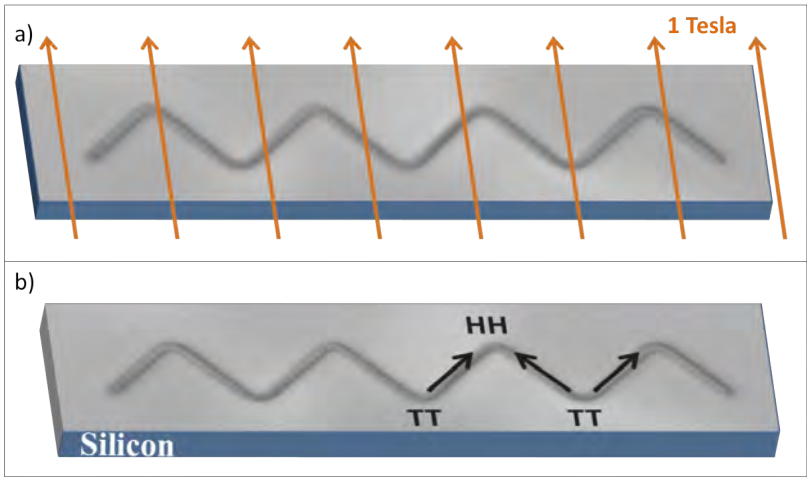

Figure 2.5: Zigzag wire traps. (a) Initial magnetization of zigzag wire traps with a momentary 1 T magnetic field perpendicular to the length of the wire. (b) Upon removal of the 1 T field, head-to-head (HH) and tail-to-tail (TT) domain walls are formed at the vertices.

2.3 Electromagnetic control for external magnetic fields

The magnetic tweezer platforms are placed within an electromagnet setup that provides the x-, y-, and z-components of the external magnetic field. Four orthogonal opposite-pole electromagnets (Magnetech, cat. no. OP-2025) create the in-plane external magnetic fields ($\mathbf{H}_x$ and $\mathbf{H}_y$) for the setup and a wound copper wire solenoid (z-coil) supplies the out-of-plane field ($\mathbf{H}_z$). Because the sample is placed directly in the center of the z-coil and midway between each pair of electromagnets (Figure 2.6 (a) and (b)), the field is approximately spatially uniform. Fields were calibrated with a gaussmeter (F.W. Bell Series 9550 Gauss/Teslameter).

Current is delivered to the electromagnets using three power supplies (solenoid, Kepco BOP 20-10ML; electromagnets, Kepco BOP 20-10ML4886), Figure 2.6 (c). Programmed LabView software (National Instruments) allows for pre-programmed routines to be controlled in real time by the user interface on the computer (Figure 2.6 (d)) or a game controller

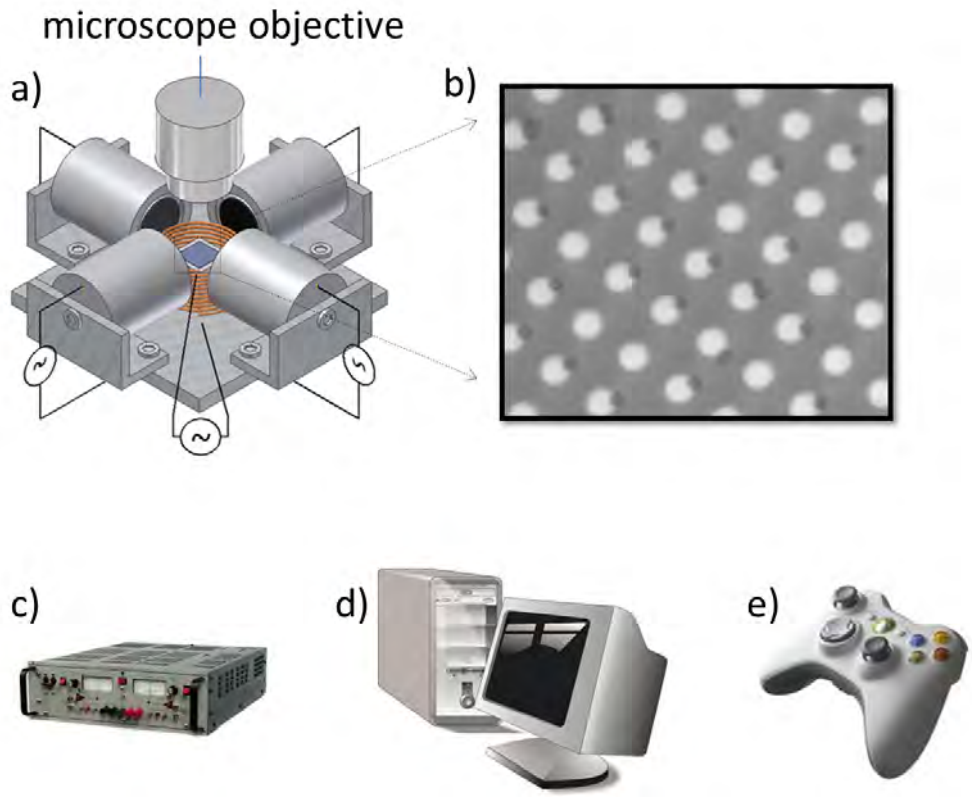

Figure 2.6: Electromagnet setup. (a) External fields are provided by 4 orthogonal electromagnets and a solenoid. (b) Magnetic disk traps (white) manipulate many magnetic microbeads (dark) simultaneously. (c) Current is provided by a power supply (d) remotely controlled by LabView programs. (e) To facilitate ease of use, a game controller is utilized as a user interface to call specific pre-programmed routines.

interface (Figure 2.6 (e)).

2.4 Microchannel devices

2.4.1 Compression channels

Early microchannel designs used for DNA studies (see Chapter 4) are compression channels. The silicon wafer, which serves as the floor of the channel, is tightly compressed between two interlocking aluminum pieces (labeled "base" and "lid" in Figure 2.7(a)) and tightened with screws in countersunk holes in the base. An O-ring or silicon glue (DAP® cat. no. 00688) is used to cushion the silicon chip against the base. The channel walls (milled through the aluminum lid) are approximately 250 μm high and on either side is a fitted hole for input

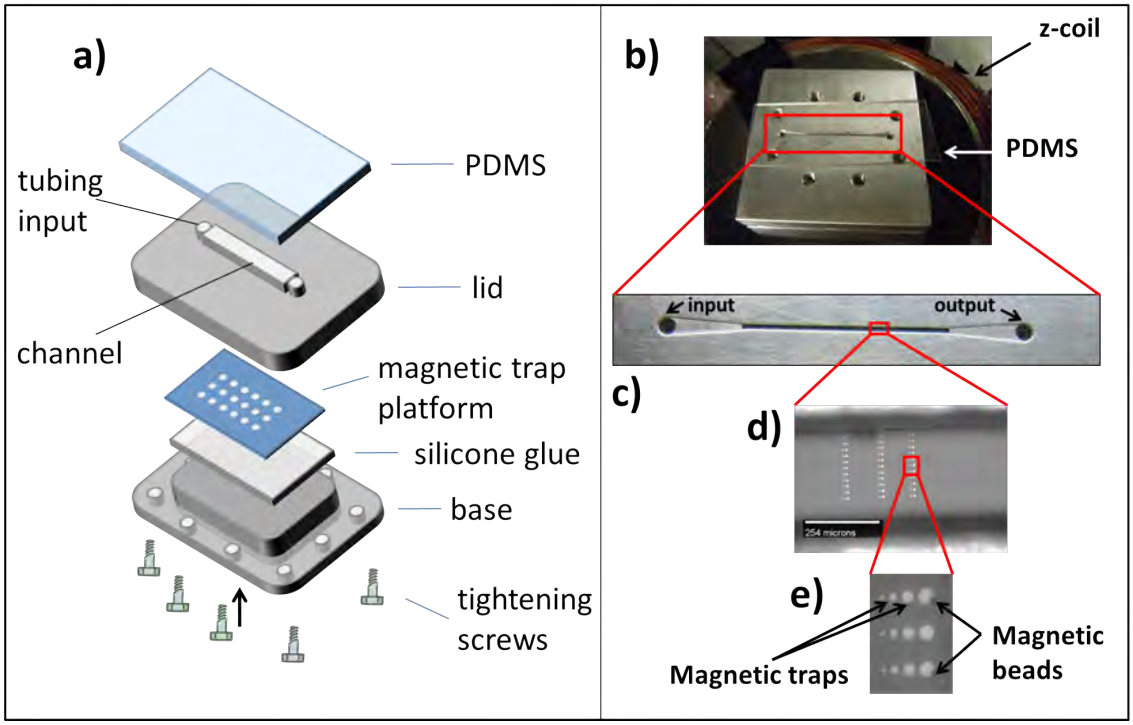

Figure 2.7: Compression channel. (a) This channel consists of two interlocking pieces ("base" and "lid") that are compressed with tightening screws to hold the magnetic trap platform in place. Between them, silicone glue cushions the magnetic trap platform, which serves as the base of the channel. A piece of PDMS placed on top creates the ceiling of the channel. Drilled holes allow tubing to enter through the bottom of the lid (through "tubing input"). (b) Photograph of device at the center of the z-coil. (c) Tubing is fitted through holes in the aluminum to the input and output reservoirs. (d) Channel is approximately 250 μm wide and 250 μm deep, with (e) patterned magnetic traps on the silicon wafer that sit at the floor of the microchannel.

and output tubing (Fig. 2.7 (a) and (c)). A ∼1 mm thick piece of polydimethylsiloxane (PDMS) placed over the top completes the rectangular channel (Figure 2.7(a) and (b)). Thus the channel is bounded by aluminum walls on the sides and PDMS on top. The silicon chip with magnetic disk traps makes the floor of the channel (Figure 2.7(d) and (e)).

Compression channels allow for fluid control via syringe pumps (Harvard Apparatus PHD Ultra programmable syringe pump). Design assistance and machining was carried out by Mr. John Gosser and Mr. Jonathon Shover in the OSU physics machine shop.

2.4.2 Molded PDMS channels

Molded PDMS channels can be used to completely replace the necessity for the base and lid of the compression channels. Furthermore, a mold can be made in nearly any shape, offering

variations from the basic straight rectangular flow channel of the compression channel. The depth of the compression channels was limited to ~250 μm while PDMS channels are easily fabricated to be only micrometers (or even tens to hundreds of nanometers [18, 55]; also see Chapter 6) in dimension.

As PDMS can be easily cut with a razor blade or PDMS punch (Ted Pella, Inc.), these devices can be modified (e.g. using a coring punch to add a particular size of input tubing). PDMS is also optically transparent and can be easily integrated with existing devices (e.g. used in conjunction with an upright optical microscope to visualize microbeads within the channel).

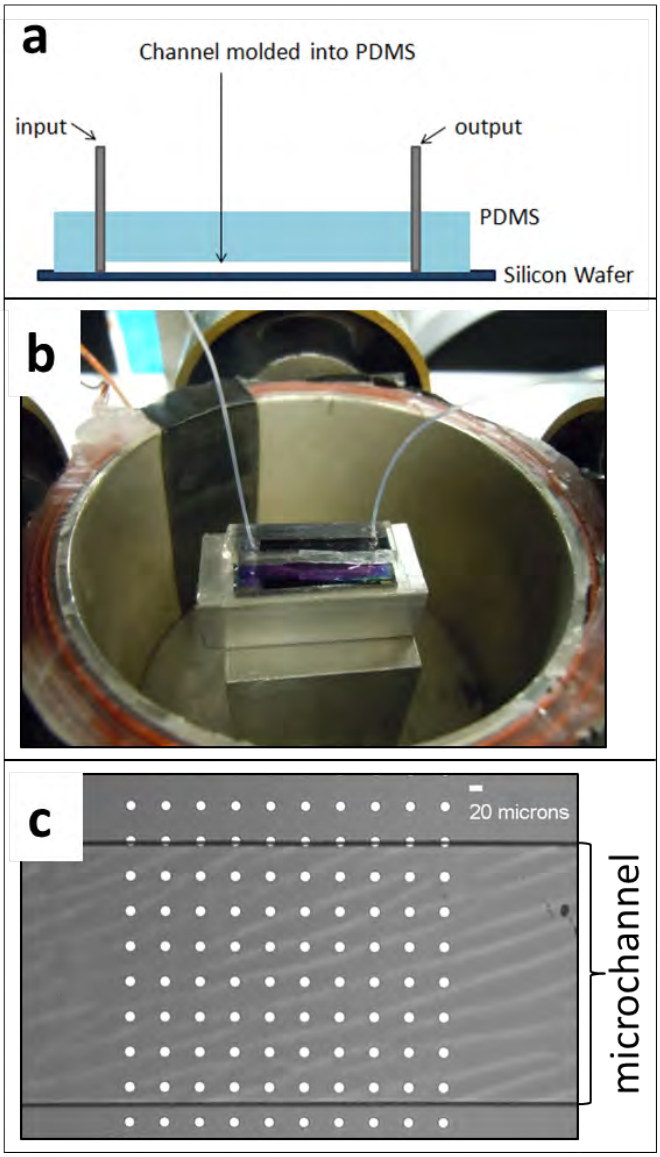

Figure 2.8: Molded PDMS Channels. (a) Schematic of simple 1 cm x 100 μm x 100 μm (check depth) microchannel with tubing through PDMS for input and output. (b) Photograph of microchannel described in (a), placed within the electromagnet setup. (c) Micrograph of one region of the microchannel shown in (b), with disks patterned on the silicon chip.

PDMS channels are created using molds. A mold can be made with photolithography. Regions of photoresist exposed to UV light will crosslink and remain on the surface of the wafer. Upon development, regions that were not exposed will be removed and a mold will remain with the thickness at which the photoresist was spun onto the device. After the mold is complete, it is silanized to prevent permanent adhesion of PDMS to the surface. A mixture of curing agent to liquid

PDMS in a 1:1 ratio is then poured onto the mold, bubbles removed in vacuum for 30 minutes, and baked at 60^{o}C for 30 minutes. In the case of more detailed or nanoscale-sized structures, such as those described in Chapter 6, a mixture of curing agent to PDMS in a 1:10 ratio may be poured and baked prior to the 1:1 ratio to ensure that the smaller features are properly molded into the device. After the PDMS has hardened, it may be gently peeled off of the mold and then baked for 15 hours at 170^{o}C (BlueM Resist Bake Oven) before use.

The most basic PDMS channels used in this paper are similar in design to the compression channels but smaller in dimensions (Figure 2.8). A single straight channel (100 μm wide, $\sim$100 μm deep and $\sim$1 cm long), with holes punched for tubing at either end, was used for DNA experiments following the experiments in compression channels (Chapter 5). Other, more complex designs used for electroporation studies will be presented in Chapter 6.

2.4.3 Bonding

An additional benefit of PDMS channels is that they adhere well to silicon, glass, and quartz surfaces. In fact, low-pressure microfluidic devices can be made with no additional bonding of the PDMS to the chip. However, to ensure that leaking will not occur, as is required for high flow rate microfluidics and high voltage electroporation experiments, PDMS can be permanently bonded to the surface of the chip.

To bond the PDMS to the chip, the chip is first sonicated or cleaned with acetone, isopropanol and DI. The PDMS surface is cleaned with Scotch® tape. Both are oxidized with an oxygen plasma cleaner (PTS Oxygen Plasma System) and then pressed together gently. If precise alignment is required (as with magnetic tweezers-assisted 2D nanochannel electroporation, Chapter 6), methanol is used as a lubricant between the two as they are carefully aligned by hand under a microscope. After the methanol is dry, a 10 minute 70^{o}C bake ensures contact for bonding between the PDMS and the chip. Devices are then used a few hours following the bonding procedure. If nanochannel electroporation devices are not to be used that day, they may be filled with methanol to prevent collapse of the nanochannel

prior to use.

2.5 Microbeads

2.5.1 Polystyrene microbeads

Nonmagnetic microbeads are often made of the polymer polystyrene. Magnetic microbeads, which range in size from about 0.5 μm to 100 μm in diameter, are also polystyrene. To make them magnetic, iron oxide nanoparticles are embedded in the polystyrene matrix (Fig. 2.9), often suspended in a smaller core region of the microbead that is then coated in an outer layer of polystyrene.

Though most of the experiments utilizing micro-magnetic traps in this thesis require the use of magnetic microbeads (∼1 - 10 μm diameter) it is occasionally helpful to also make use of the nonmagnetic polystyrene beads. For example, as described in Chapter 4, DNA can be labeled with a magnetic bead on one end and a nonmagnetic bead on the other end. In this way, magnetic traps can localize one end of the DNA on a magnetic trap while drag force due to fluid flow on the nonmagnetic microbead applies a force to the other end. Because only one end is attached to a magnetic microbead, there is no magnetic coupling between the beads, which could in turn cause the DNA to remain coiled.

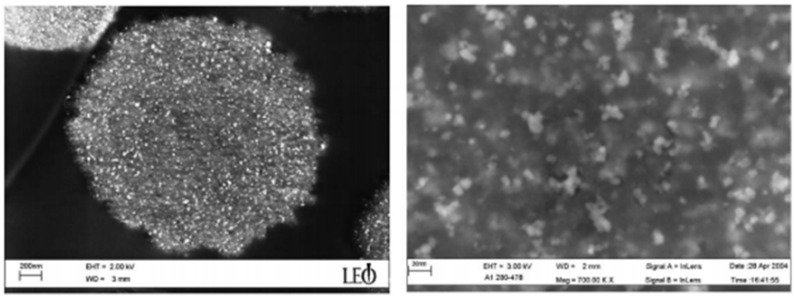

Figure 2.9: Superparamagnetic microbeads. Two SEM images show different magnifications of Dynabeads M280 superparamagnetic microbeads (see Chapter 4). In the image on the right, the brighter spots are the superparamagnetic nanoparticles. Image from Fonnum et al, *Journal of Magnetism and Magnetic Materials*, 2005

Both magnetic and nonmagnetic beads are available commercially and can be functionalized with a number of different molecules. Most common are amine (NH_2) and carboxyl (COOH) groups, which provide a potential linker for attachment to various other molecules. Furthermore, these beads can be functionalized with antibodies to be attached to surface receptors on cell membranes (see Chapter 6).

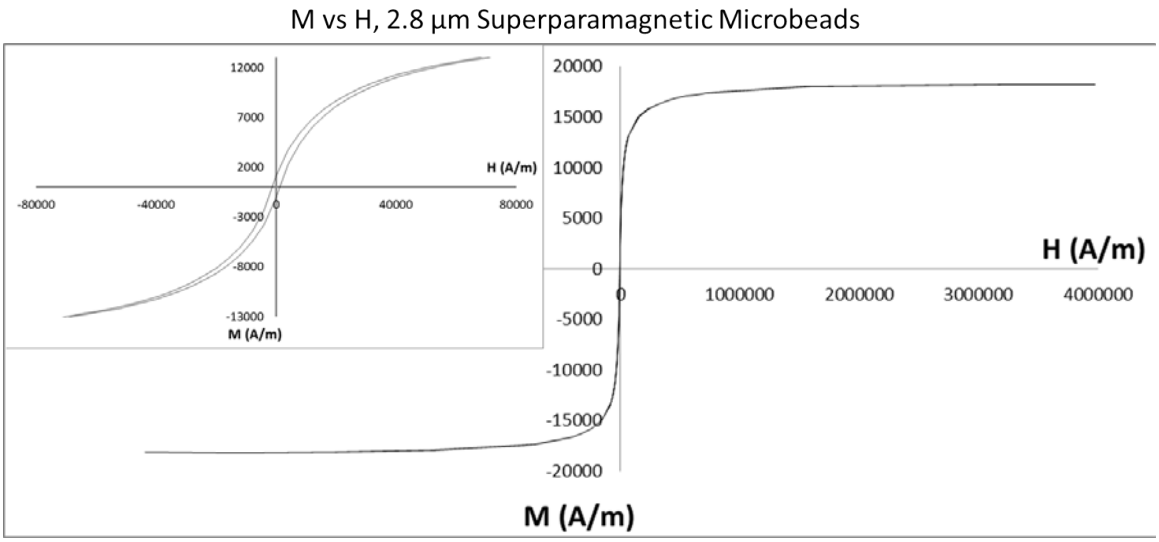

Figure 2.10: SQUID data. The SQUID measurements indicate that the 2.8 μm microbeads are largely superparamagnetic. Inset shows the zoomed-in low-field regime. The linear region (see Chapter 3) is from approximately -15,915 A/m to 15,915 A/m (or -200 Oe to 200 Oe).

2.5.2 Superparamagnetic microbeads

The microbeads used in the experiments presented are superparamagnetic. Each microbead is a spherical polystyrene matrix within which iron oxide nanoparticles are suspended (Figure 2.9). These single-domain iron oxide nanoparticles are approximately $<$ 100 Å [56], which is below both the single-domain limit and the superparamagnetic limit, (roughly on the order of 100 nm and 10 nm, respectively, for iron oxide) [57, 58]. Because the embedded nanoparticles are below the superparamagnetic limit, the microbead itself will exhibit superparamagnetic properties. In particular, each bead will magnetize rapidly in the presence of even a weak magnetic field and, upon removal of the field, retain little to no remanent magnetization. These attributes are particularly useful on the magnetic tweezer platforms because weak fields are able to magnetize the microbeads and the beads do not aggregate when the field is removed.

To ensure that the microbeads are in fact superparamagnetic, SQUID measurements (SQUID magnetometer, Ohio State NanoSystems Laboratory) were taken to confirm the expected properties. Measurements were taken on a volume of 50 μL (approximately 1 $\times$

10^8 microbeads) M270 superparamagnetic microbeads (Dynabeads cat. no. 14305D). These beads were dried into a small container to reduce bead movement during the measurement. The results, which confirm largely superparamagnetic behaviour, are shown in Figure 2.10.

2.5.3 Janus particles

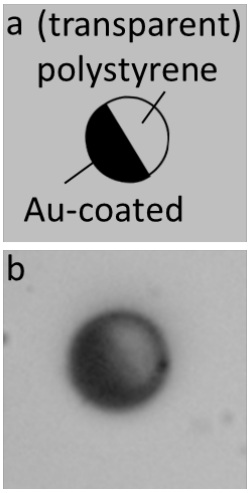

Figure 2.11: Janus Particle. (a) Schematic and (b) microscope image of a 8.5 μm diameter Janus particle coated in 100 nm Au. Microscope image provided by Mrs. Stephanie Lauback.

The Janus particles used in Chapter 5 are microbeads that are optically asymmetric, i.e. one side is opaque and the other is not, thus appearing dark- and light-colored, respectively. This assists in visual determination of the orientation of the bead when it is moving, specifically to differentiate between rolling motion and purely translational motion. To create Janus particles, magnetic microbeads (Spherotech or Dynabeads) with carboxyl group functionalization are washed in IPA and dried with nitrogen gas onto the surface of a clean silicon wafer. That wafer is then coated in 100 nm Au with an evaporator (Denton DV-502A E-Gun Evaporator). Particles are then removed from the wafer with a DI rinse. Sonication can assist in dislodging particles, but often small pieces of gold will also flake off during the process, which are difficult to separate from the microbeads. A wash procedure with centrifugation is then used to place the Janus particles in the desired buffer. A Janus particle is shown in Figure 2.11. Polystyrene is translucent, thus appearing lightly colored adjacent to the darker gold side of the bead. Janus particles may be nonmagnetic polystyrene or magnetic beads. For the studies presented in this document, magnetic beads are used.

2.5.4 Labeling DNA and cells with microbeads

Both DNA and cells can be labeled with magnetic and nonmagnetic microbeads of various sizes to enable manipulation on the magnetic tweezer platform.

DNA labeling

Either single-stranded or double-stranded DNA can be attached to microbeads if first labeled with a ligand. In the studies presented here, DNA primers labeled with digoxigenin and biotin were first kinased and then ligated to either end of double-stranded lambda DNA (16.5 μm), leaving the DNA strand labeled with a different ligand on each end. In this way, for example, one end could be attached to the surface of a flow channel while the other is attached to a microbead. Or, the ends could both be attached to beads (e.g. one end attached to a magnetic bead and the other to a nonmagnetic bead). Digoxigenin on one end of the DNA strand will attach, for example, to an anti-digoxigenin coated surface and biotin on the other end will attach to a streptavidin coated magnetic microbead (see Appendix for protocol details).

Cell labeling

The cells used in the studies presented in this document were linked with magnetic beads to enable remote control of the cells by magnetic tweezers. Dextran-coated magnetic microbeads (1 μm diameter, StemCell Technologies, Cat. No. 19250) are attached to cells via CD45 antigen, which is an antigen commonly expressed on human leukocytes. This encompasses the purified human white blood cells, Jurkat human T lymphocyte cell lines, KG1a leukemic cell lines, and K562 human myelogenous leukemia cell lines utilized in Chapter 6. To attach these beads, depletion cocktail (EasySepTM Human CD45 Depletion Kit, Stem Cell Technologies, Cat. No. 18259) containing tetrameric antibody complexes targeting CD45 antigens is mixed with cells in phosphate buffered saline (PBS) and allowed to incubate for 30 minutes at room temperature with regular mixing. Dextran coated magnetic microbeads are then added and incubated for 15 minutes at room temperature. Unlabeled cells are removed with 1-2 wash steps, using a magnet to prevent the loss of labeled cells.

2.6 Surface functionalization for DNA binding

2.6.1 Functionalization

Surfaces such as silicon, quartz, or glass chips patterned with magnetic traps may be functionalized for attachment to a labeled strand of DNA. For the DNA studies presented in Chapter 4, flow channels (silicon surface) were coated in antidigoxigenin to attach to the digoxigenin-labeled lambda DNA. Syringe pumps using 50 μL syringes connected to tubing (Hamilton Company USA) were used to controllably inject liquids into the channel. 8% glutaraldehyde in PBS is followed by 0.1 mg/mL antidigoxigenin which is then linked to the silicon surface. Following incubation, BSA is added to block any surfaces not covered in antidigoxigenin. Strands of DNA labeled with digoxigenin can then be attached by flowing in and allowing them to settle on the functionalized surface. See Appendix A for more details.

2.6.2 Nonspecific binding and surface treatments

Nonspecific binding is very common in experiments involving biological materials such as cells and DNA. For example, both adherent and suspension cells will often adhere to surfaces. This should be avoided or reduced as much as possible. Below are a few techniques that can be used to reduce or eliminate nonspecific binding.

UV-ozone is a dry surface treatment process combining UV light with atmospheric oxygen (0_2) to create ozone (0_3), which will then break down and remove any organic compounds on the surface. The resulting surface is clean and, as a secondary effect, less hydrophobic. Due to the decontamintation abilities, the UV treatment is useful prior to any experiments involving live cells (see Chapter 6) as it will prevent contamination for further culturing of the cells. It further assists with other surface modifications and bonding (i.e. PDMS, see "Bonding" section of this chapter). Treatment with UV-ozone is preceded by cleaning with DI water or solvents to remove large dust particles and salts. UV-ozone treatment of 5-10 minutes is done prior to all PEG modifications and long-term cell experiments, as well as experiments that would benefit from a hydrophilic surface (e.g. improved fluid

flow for microfluidics).

UV-ozone treatment is often followed by a Polyethylene glycol (PEG) surface modification for any cell experiments. PEG reduces non-specific binding of cells on surfaces [59, 60]. The polymer chains attach to the surface, making it hydrophilic and reducing protein adsorption, thus reducing nonspecific cell adhesion to the surface via cell membrane proteins. For the nanochannel electroporation studies presented in Chapter 6, PEG-Silane (Laysan Bio, Inc., MW 2000, lot #114-08) was used to modify surfaces prior to experiments. The procedure (following UV-ozone for 5-10 minutes) consists of (1) a 30 minute room temperature incubation with 1 mM PEG-Silane in ethyl alcohol, (2) an ethyl alcohol rinse, and (3) a 30 minute bake at 110^{o}C.

Buffer choice

Various buffers have been used in the studies presented. For most cell experiments, phosphate buffered saline (PBS), pH 7.4, is used. However, for some experiments a reduction in nonspecific binding of cells to not only the surface but also to beads, to one another, and to various other surfaces (e.g. tubing) is critical. For example, blockages can form in tubing with small inner diameter due to cells and/or microbeads sticking to one another and to the inner surface of the tubing. Additives to the PBS buffer used can help reduce this. The experiments of Chapter 4 utilize pluronic, a surfactant, to reduce adhesion. For electroporation experiments (Chapter 6), the buffer used to reduce adhesion contains 5 mg/mL Pluronic F-68 (Sigma Aldrich, P1300), 1% bovine serum albumin (BSA), and 5mM ethylene-diamine-tetraacetic acid (EDTA) in PBS.

Chapter 3
Theoretical basis for micro-magnetic traps

3.1 Superparamagnetic microbeads

Based on superparamagnetic theory, it is assumed that in the region from -200 Oe to 200 Oe (or in Figure 2.10, see Chapter 2, from -15,915 A/m to 15,915 A/m), known as the linear regime, the magnetization (**M**) of a bead is approximately linear in applied field, **H**:

$$\mathbf{M_{bead}} = \chi \mathbf{H}$$

The linear regime encompasses the highest fields used in the magnetic tweezer platform and yields an approximate susceptibility χ of 0.5 for the 2.8 μm beads.

3.2 Zigzag Wires

3.2.1 Point Charge Approximation for fields from Wire Traps

After initial magnetization (Chapter 2) of the zigzag wires, domain walls will exist at the vertices and are labeled as either head-to-head (HH) or tail-to-tail (TT) based on

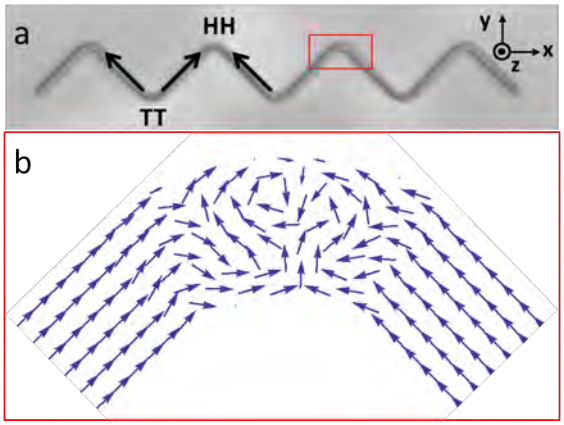

Figure 3.12: Domain walls in zigzag wires. (a) After magnetization, domain walls will be located at vertices, referred to as head-to-head (HH) or tail-to-tail (TT). (b) A sample OOMMF simulation shows the magnetization within a CoFe wire HH domain wall (outlined in red in part (a)). OOMMF simulation provided by Mr. Michael Prikockis.

the relative orientation of the domains in the length of the wire (Figure 3.12 (a)). Object oriented micromagnetic framework (OOMMF) simulations of the magnetization in a 1 μm wide wire at a HH domain wall in the presence of an out-of-plane external field of 75 Oe is shown in Figure 3.12 (b).

A point charge approximation may be used to determine the total field and hence the energy landscape along the wires. This approximates the wires to be infinitely thin and each domain wall to be a monopole-like point charge located at the center of the vertex. The effective magnetic charge of each domain wall can then be calculated by:

$$q_m = 2 \cdot M_s \cdot b \cdot w$$

in which M_s is the saturation magnetization ($\sim 16 \times 10^5$ A/m), b is the thickness (here $\sim$12 nm), and w is the width ($\sim$1.3 μm) of the $Co_{0.5}Fe_{0.5}$ wire. From this, the domain wall field

$$\mathbf{H}_{dw} = \frac{q_m}{4\pi} \cdot \frac{\mathbf{r} - \mathbf{r}_0}{|\mathbf{r} - \mathbf{r}_0|^3} \tag{3.1}$$

can be determined, where $|\mathbf{r} - \mathbf{r}_0|$ is the distance of the bead from the vertex. For the following potential energy calculations, only the vertices in question are considered (i.e. the initial and final vertex for the bead's trajectory from one vertex to a neighboring vertex).

3.2.2 Potential energy landscape and resulting forces on beads

Once the position dependent total field, which includes both the external field $\mathbf{H}_{ext}$ and the domain wall field ($\mathbf{H}_{tot} = \mathbf{H}_{ext} + \mathbf{H}_{dw}$) is known, the magnetic potential energy on the point-like superparamagnetic bead can be determined using

$$U(\mathbf{r}) = -\frac{1}{2}\mu_0 V \chi_{eff} \boldsymbol{H}_{tot}^2 \tag{3.2}$$

where μ_0 is the permeability of free space and V and χ_{eff} are the volume and effective susceptibility of the bead, respectively.

In Figure 3.13, the magnetic potential energy is plotted for three different external field configurations for a 2.8 μm superparamagnetic bead.

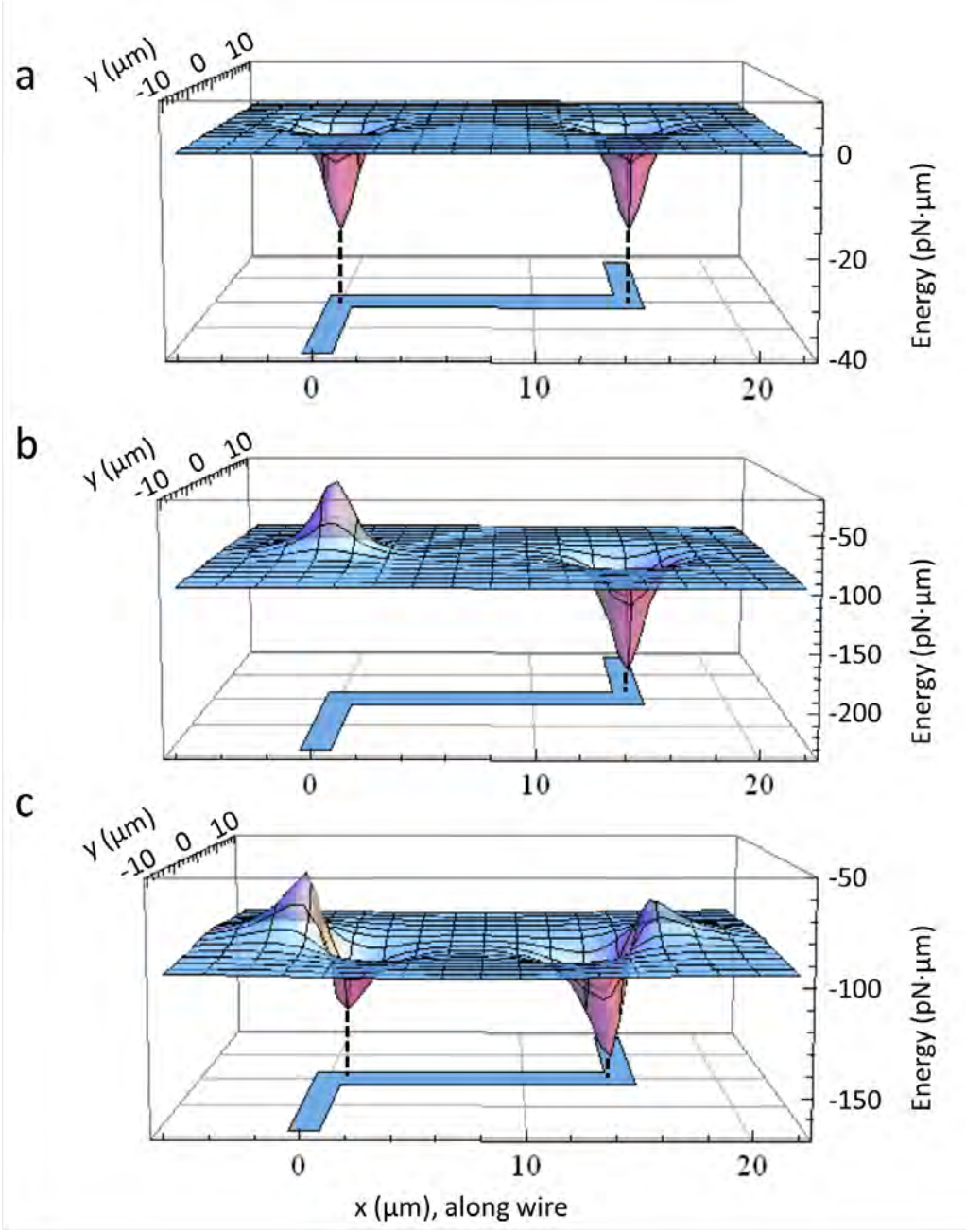

Figure 3.13: Magnetic potential energy plots. Here plots are shown for (a) no external field (all vertices will trap magnetic beads), (b) $\mathbf{H}_{ext}$ = (10 Oe, 0 Oe, 50 Oe) (one vertex will repel beads while the other traps beads), and (c) $\mathbf{H}_{ext}$ = (50 Oe, 0 Oe, 10 Oe). Dashed black lines show approximate locations on the wire of magnetic potential energy traps.

In Figure 3.13 (a), there is no external field ($\mathbf{H}_{ext}$ = (0 Oe, 0 Oe, 0 Oe)). The corresponding magnetic potential energy plot shows potential energy wells at both vertices. Nearby super-

paramagnetic beads will align with the stray fields from the domain walls at both HH and TT vertices. When an out-of-plane field $\mathbf{H}_z$ is applied in the presence of a weak in-plane field (Figure 3.13 (b), $\mathbf{H}_{ext}$ = (10 Oe, 0 Oe, 50 Oe)), one domain wall will become repulsive while the other becomes a deeper well, or trap. However, if the in-plane field is larger than the out-of-plane field (Figure 3.13 (c), $\mathbf{H}_{ext}$ = (50 Oe, 0 Oe, 10 Oe)), two potential energy traps will appear, with one being stronger than the other. These different configurations will be explored in Chapter 5.

Using Equation 3.2 for the potential energy, the force experienced by the superparamagnetic bead at weak fields can then be calculated [48]:

$$\mathbf{F}(\mathbf{r}) = -\boldsymbol{\nabla} U(\mathbf{r}) = \frac{1}{2}\mu_0 \chi_{eff} V \boldsymbol{\nabla} \mathbf{H}(\mathbf{r}) \tag{3.3}$$

3.3 Magnetic Disk Traps

When a weak external field (< 200 Oe) is applied to permalloy, it will readily magnetize almost entirely in the direction of the in-plane field due to the small relative thickness of the disk (∼40-60 nm). The resulting magnetization of the disks is determined using a two-dimensional Object Oriented Micromagnetic Framework (OOMMF) simulation program. Figure 3.14 shows a sample OOMMF simulation for a 10 μm diameter disk 60 nm thick, 8.6×10^5 A/m saturation magnetization, beginning with random magnetization. The simulation is for an applied constant in-plane field $\mathbf{H}_{xy}$ = 60 Oe in the +x-direction in the absence of an out-of-plane field ($\mathbf{H}_z$ = 0 Oe).

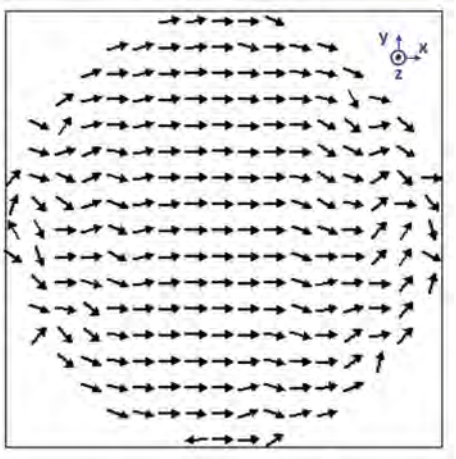

Figure 3.14: OOMMF simulation. The magnetization is shown for a 10 μm diameter, 60 nm thick magnetic permalloy disk in a constant external field of $\mathbf{H}_{xy}$ = 60 Oe in the + x direction and $\mathbf{H}_z$ = 0 Oe.

The resulting magnetization $\mathbf{M}(x, y, z)$ across the surface of the disk, which is broken up into cells sized 50 nm x 50 nm, each 60 nm thick, allows for a magnetic charge density $\rho_m = \boldsymbol{\nabla} \cdot \mathbf{M}(x, y, z)$ to be calculated. As with the zigzag wires, an effective magnetic

charge q_m can be determined for each cell with:

$$q_m = \rho_m V_{cell}$$

where V_{cell} is the volume of the cell. The field $\mathbf{H}_{disk}$ can be calculated using Equation 3.1. From combined magnetic field $\mathbf{H}_{tot} = \mathbf{H}_{ext} + \mathbf{H}_{disk}$, the potential energy (Equation 3.2) and force on the superparamagnetic bead (Equation 3.3) can be determined.

3.4 Drag forces in low Reynolds number environnments

An important consideration when studying forces on microbeads in microfluidic devices is the Reynolds number. Microbeads in microfluidic channels are in a low Reynolds number environment [61]. The Reynolds number may be calculated with:

$$Re = \frac{a\rho v}{\eta}$$

where a is the radius of the bead, ρ the density of the fluid, v the velocity of the bead and η is the dynamic viscosity of the fluid. For a 2.8 μm diameter bead moving at 20 μm/s through water ($\rho \approx 1000 kg \cdot m^{-3}$ and $\eta \approx 10^{-3}$ Pa·s), Re $\sim 10^{-6}$. For comparison, a human swimming in water would have a Reynolds number on the order of 10^4. In the low Reynolds number environment, viscous forces dominate and inertial forces are often approximated to be zero [61, 62].

In addition to the magnetic forces, hydrodynamic drag forces will dominate and oppose the motion of microbeads. The drag forces can be approximated using Stokes' Law [63]:

$$F_{drag} = 6\pi\eta a v. \tag{3.4}$$

where η is the dynamic viscosity of the fluid, a is the radius of the microbead, and v is the velocity of the microbead. Here near-surface effects are neglected.

Chapter 4
DNA Manipulation

4.1 Introduction

The array design of the micromagnetic structures renders a platform that is conducive to multiplexing single-molecule DNA force and elasticity experiments. The field of DNA elasticity measurements has been well-studied [64, 65]. Experiments utilize force-transmitting handles (e.g. a microbead) attached to one or both ends of a strand of DNA to apply a series of controlled forces and stretch the DNA. The most common technologies used are optical tweezers [66], atomic force microscopy [67] conventional magnetic tweezers [68], and hydrodynamic forces [69, 70].

Although the elastic properties of DNA are already well-studied, there are a few unique benefits offered by the array of micromagnetic traps for these experiments. First, the platform allows for multiplexing of single-molecule experiments, which is difficult to do with the techniques mentioned above, particularly AFM and optical tweezers. Secondly, all experiments on the magnetic tweezer platform take place on a single horizontal plane (at the surface of the platform), which allows for realtime observation of the experiments and the potential to integrate fluorescent markers for targeting specific sites along the molecules. Lastly, the fact that DNA has been well characterized with other methods suggests that the studies may instead use known elastic properties of DNA to validate the theoretical model of forces exerted by magnetic traps [71].

The experiments presented in this chapter act as preliminary studies to confirm that DNA experiments are accessible on the disk-based micromagnetic trap platform. These

experiments offer a starting point with potential for future studies.

4.2 Experimental Setup

Magnetic disk traps patterned onto silicon wafers and placed into either microfluidic compression channels (see Chapter 2) or molded PDMS channels (see Chapter 2) were used for these experiments. Tubing at input and output reservoirs (Figure 4.15) allows for DNA to be introduced into the device and removed from the device by controlling the rate and direction of flow with a syringe pump (PHD Ultra, Harvard Apparatus) attached to the tubing. With the syringe pump controlling the flow rate, the hydrodynamic drag force (Chapter 3) can be applied to all microbeads linked to DNA strands within the channel to aid in magnetic force based stretching experiments. Double-stranded lambda DNA (48.5 kbp, corresponding to an end-to-end length of approximately 16.5 μm) was the biomolecule utilized for all experiments in this chapter.

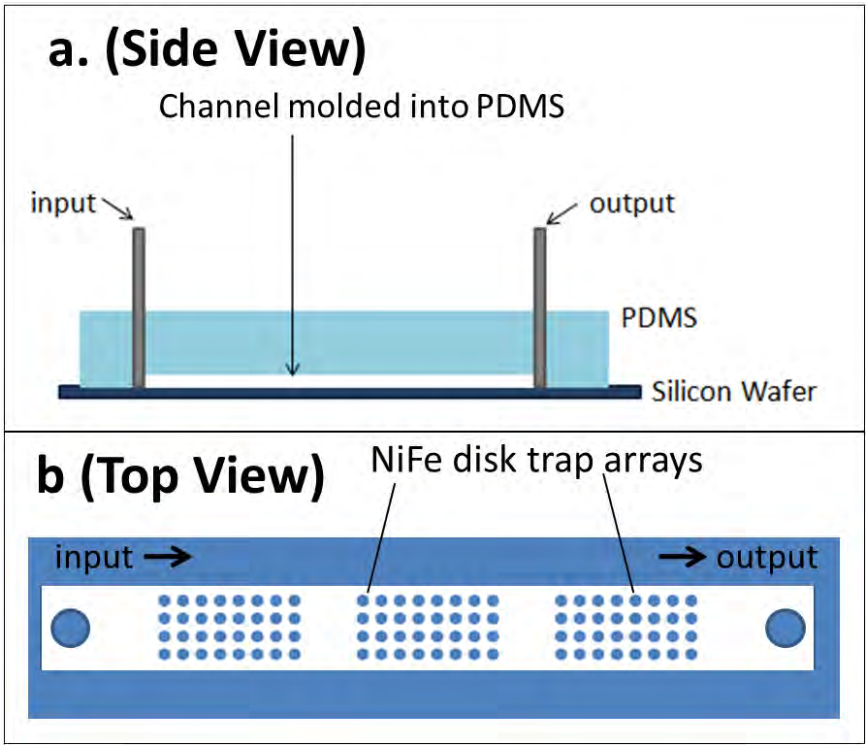

Figure 4.15: Flow channel. (a) Side view and (b) top view of molded PDMS straight channel, 100 μm wide, ~30 μm deep, and ~1 cm long. Input and output tubing supplies DNA and microbeads into the channel and patterned magnetic disk traps are located on the floor of the channel itself.

Three different design implementations for DNA tethers were investigated: (a) tethering one end of the DNA strand to the silicon surface and the other end to a magnetic microbead,

(b) tethering one end to a magnetic microbead and the other to a nonmagnetic microbead, and (c) tethering both ends to magnetic microbeads. Tethering was performed as described in Chapter 2 by attaching antidigoxigenin (on silicon surface or nonmagnetic bead) to digoxigenin (on DNA) or streptavidin (on magnetic microbead) to biotin (on DNA).

4.3 Results

4.3.1 Surface and microbead

A common technique with most DNA elasticity experiments is to anchor one end of the DNA strand to a surface [8, 67, 68, 69] while a force is applied to the other end to stretch the molecule. Preliminary experiments with surface tethers in a microfluidic channel are shown in Figure 4.16. Here, lambda DNA labeled with digoxigenin primers on one end were attached to an antidigoxigenin-coated surface (see Chapter 2 and Appendix A). The DNA was also fluorescently labeled with SYBR® Gold (Life Technologies, intercalating dye, excitation ~495 nm, emission ~537 nm). The figure shows fluorescing DNA with no fluid flow (coiled, Fig. 4.16 (a)) and in the presence of fluid flow (stretched in the direction of fluid flow, Fig. 4.16 (b)). Although no magnetic traps were present in this experiment, it is important to note one of the clear benefits of multiplexing in this microfluidic channel device: because all the strands of DNA are in the same horizontal plane, it is possible to visualize them simultaneously.

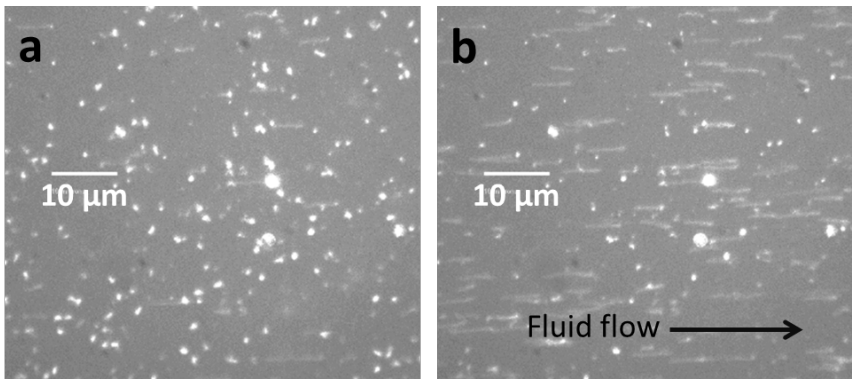

Figure 4.16: Surface DNA tethers with fluorescently labeled lambda DNA. (a) In the absence of fluid flow, bright spots indicate coiled DNA strands. (b) In the presence of fluid flow (irregular flow rate) most strands of DNA are visibly stretched in the direction of the fluid flow. Experiment performed in collaboration with Dr. Marek Šimon.

After confirming that surface tethers are possible in this device, a similar approach was attempted with magnetic beads attached to the other end of each surface

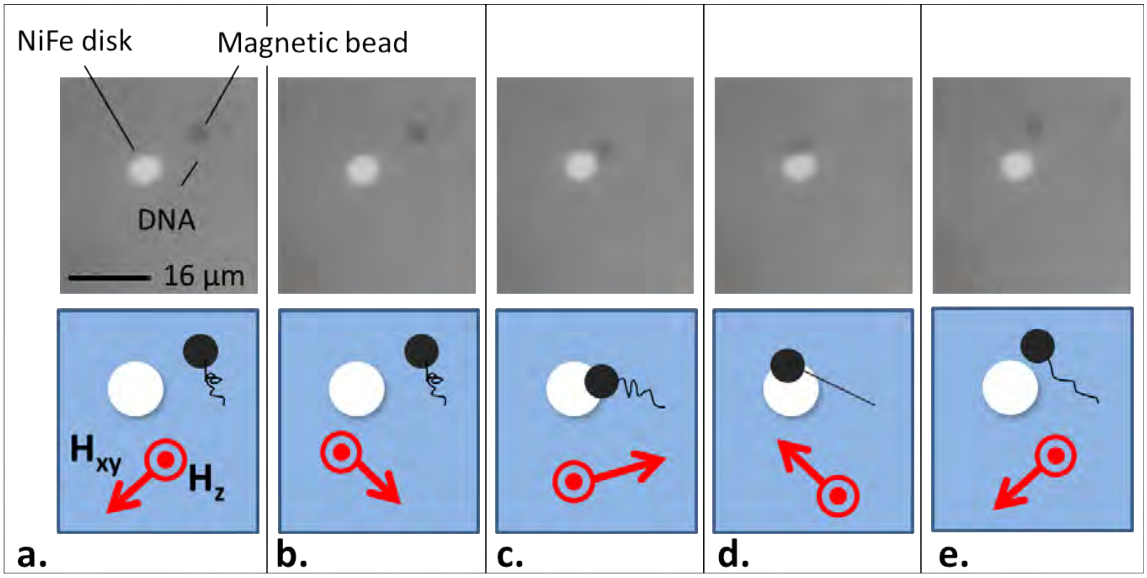

Figure 4.17: Surface tether near a disk. (a) A strand of ds-lambda DNA is tethered to the Si surface on one end and a 2.8 μm magnetic bead on the other end, near a NiFe disk. (b) While the in-plane field is directed away from the region of disk near the bead, it will not be attracted to the disk. (c) As the in-plane field continues to rotate, it will attract the bead and (d) stretch out the piece of DNA. (e) The magnetic trap is unable to stretch the strand of DNA further, and so the bead falls off the trap. Each rotation period around the disk is 1 second long, i.e. H_{xy} rotates at a frequency of 1 Hz.

tether. The magnetic beads enable DNA stretching either with hydrodynamic forces or magnetic forces. The video frames and corresponding schematic of Figure 4.17 show a situation in which a strand of DNA is tethered to the surface (tether location determined by hydrodynamic flow experiments, not shown) on one end and a magnetic bead on the other, near a permalloy magnetic disk. The in-plane field rotates with a constant out-of-plane field. In Fig. 4.17 (a) and (b), the trap is located on the side of the disk furthest from the bead, and so the bead is not attracted to the disk until the in-plane field is rotated (Fig. 4.17 (c)). As the field continues to rotate (Fig. 4.17 (d)), the DNA strand is stretched until it reaches a point that the strength of the rotating magnetic trap is not sufficient to stretch the DNA strand further and the bead is then released from the disk (Fig. 4.17 (e)).

This experiment demonstrates the ability to combine hydrodynamic forces (which were used to determine the tether location, not shown) and magnetic forces (Figure 4.17) to stretch DNA. Future work on this device would benefit from additional control over the

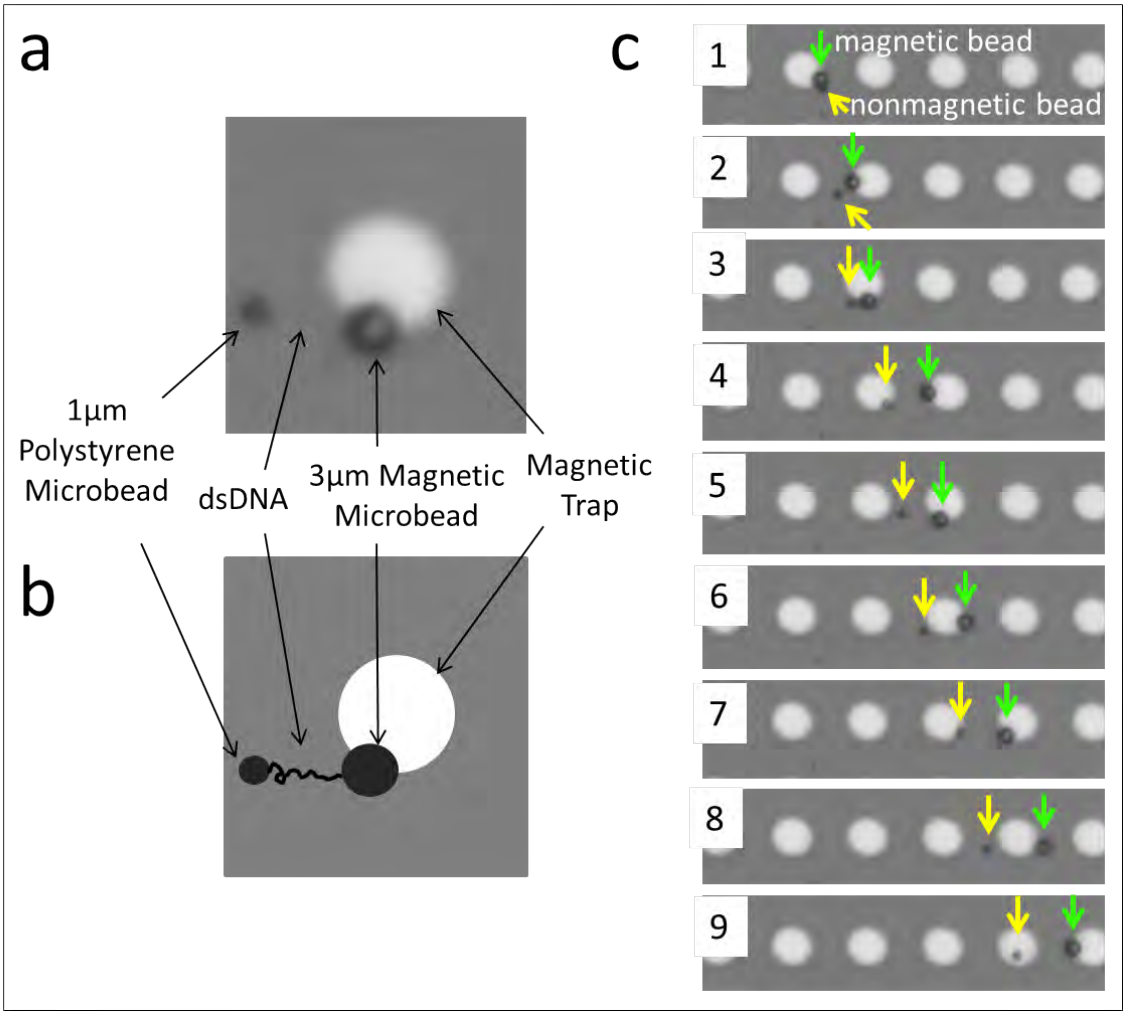

Figure 4.18: Magnetic-nonmagnetic dual tether. (a) Microscope image and (b) corresponding schematic of a strand of lambda DNA tethered between two beads, one magnetic (2.8 μm diameter) and one nonmagnetic (1 μm diameter). (c) As the magnetic tweezers are activated to pull the magnetic bead across the array, the DNA strand stretches between the magnetic bead (green arrow) and nonmagnetic bead (yellow arrow).

location of the DNA surface tethers, which is possible with an added lithographic patterning step [8].

4.3.2 Magnetic and Nonmagnetic microbeads

A second method of DNA manipulation on the micro-magnetic trap platform is to tether a magnetic microbead (2.8 μm diameter) to one end of the DNA strand and a nonmagnetic polystyrene microbead (1 μm diameter) to the other end, allowing the DNA to be manipu-

lated onto any region of the magnetic disk array without the constraint of a surface tether. The microscope image of Figure 4.18 (a) and corresponding schematic (Fig. 4.18 (b)) show the basic setup. In the absence of fluid flow, the magnetic bead may be manipulated with the mobile magnetic traps; in this case the nonmagnetic bead lags behind the magnetic bead, as seen in the sequence of images of Figure 4.18 (c). Here, the traps are used to transport the magnetic bead from one disk to the next (frames 1-2), the bead is then rotated around the outer edge of the disk (frame 3), with subsequent repetition of the process (frames 4-6 and 7-9). The frequency of hopping between disks and (full) rotation are both 0.4 s^{-1}. In the first frame (Fig. 4.18 (c1)), in which the bead-DNA-bead construct is at rest, the DNA is coiled and the magnetic and nonmagnetic beads are therefore very close to one another. However, as the magnetic bead gains momentum, a separation between the two beads is quickly established. In this case the magnetic force on the magnetic bead propels the bead forward, pulling the DNA strand and nonmagnetic bead with it. Due to this motion, a hydrodynamic drag force in the stationary fluid will oppose the motion. While the magnetic force overcomes this drag force for the magnetic bead, the nonmagnetic bead will now exert a force backwards on the DNA strand, resulting in forces acting on either end of the strand of DNA.

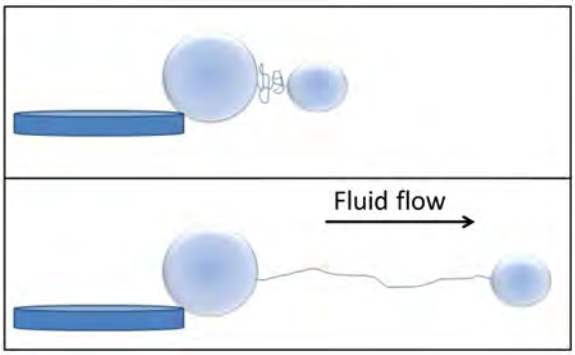

Figure 4.19: When tethered by a magnetic bead on one end and a nonmagnetic bead on the other, a strand of DNA will remain coiled with no fluid flow and will stretch with an applyed hydrodynamic force as controlled by fluid flow.

A different technique of DNA stretching with the nonmagnetic bead and magnetic bead force handles is to apply a force concentrated at one end (the nonmagnetic end) while the other end (magnetic) is held stationary by a magnetic trap (Figure 4.19). In Figure 4.20, sequential frames from a 2 second-long video show the initial stretch on a tethered strand of DNA in fluid flow. Here the magnetic bead is held on the trap by magnetic forces while the flow is gradually increased to exert increasing forces on the nonmagnetic bead. This in turn stretches the DNA between the two beads.

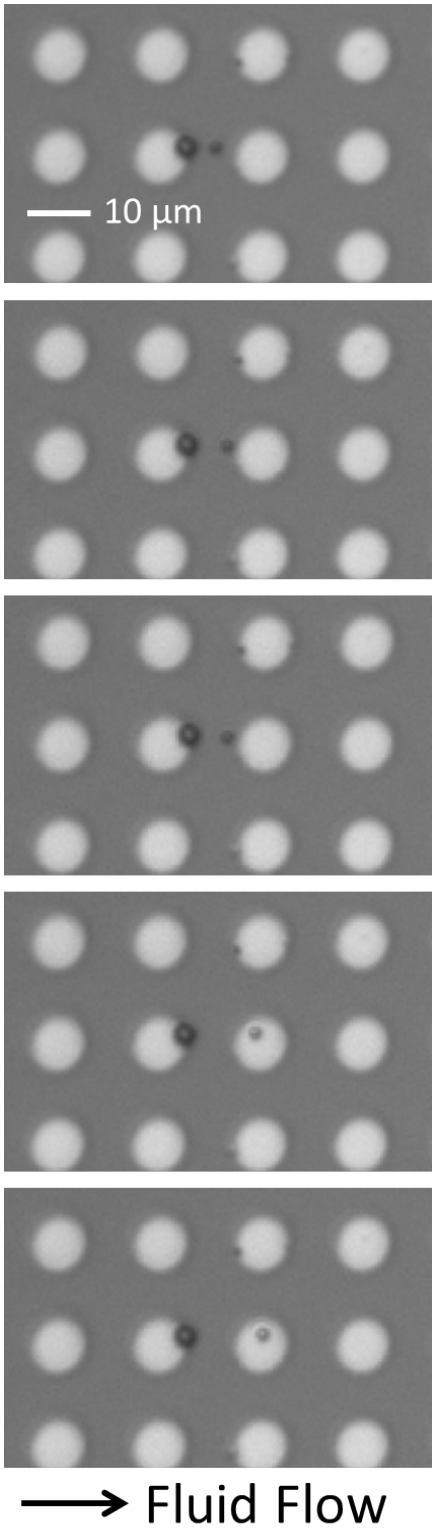

Figure 4.20: Fluid flow stretches DNA. Sequential frames from a 2-second video show a 2.8 μm diameter magnetic bead that is held at a disk trap while a tethered DNA strand is stretched by the hydrodynamic force created by fluid flow moving the 1 μm diameter nonmagnetic polystyrene bead attached to the other end. The fluid flow rate, as determined by the speed of other beads in the channel, was approximately 2 μm per second.

The advantage of techniques with only bead attachments (no surface tethers) is that following the experiment, the DNA strand may be manipulated to a different location for downstream processing. This serves two purposes: the device may be used repeatedly and the DNA strand may be further analyzed.

4.3.3 Two magnetic beads

The most technically challenging approach of DNA tethering on the magnetic trap platform is to attach a magnetic bead to each end of a strand of DNA. The idea behind this technique is to use a specially designed trap pattern to stretch the DNA at different predetermined lengths, as shown in the schematic of Figure 4.21. Here, disks of different sizes are utilized to stretch the DNA strand at different lengths as the magnetic beads rotate around the edge of either disk. This is a challenge because in the presence of a magnetic field, the two beads will couple. The first step in all procedures is to ensure that a strand of DNA is attached between the beads (generally with fluid flow) and the second step is to use the two beads to stretch the DNA strand. Both steps are done in the presence of a magnetic field.

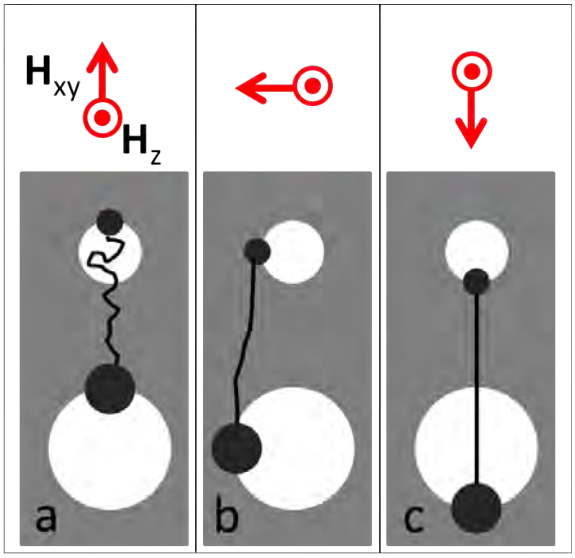

Figure 4.21: Schematic shows disks of different sizes utilized to stretch DNA at specified (a) short, (b) medium, and (c) long lengths which depend entirely on the magnetic trap pattern and external field configuration (red arrows).

Figure 4.22 shows a magnetic bead-DNA-magnetic bead tether in a microfluidic channel. In Figure 4.22 (a), one bead is trapped on a magnetic disk while the other is pulled away by fluid flow, remaining tethered and thus confirming the presence of the DNA strand between the two beads. The in-plane magnetic field is then reversed (Fig. 4.22 (b)), releasing the construct to flow in the direction of fluid flow until it is again trapped by disks (Fig. 4.22 (c)), with each end on a different magnetic trap. In this case, the two disks on which the beads are trapped are 3 μm and 5 μm in diameter, with 7.5 μm center-to-center spacing,

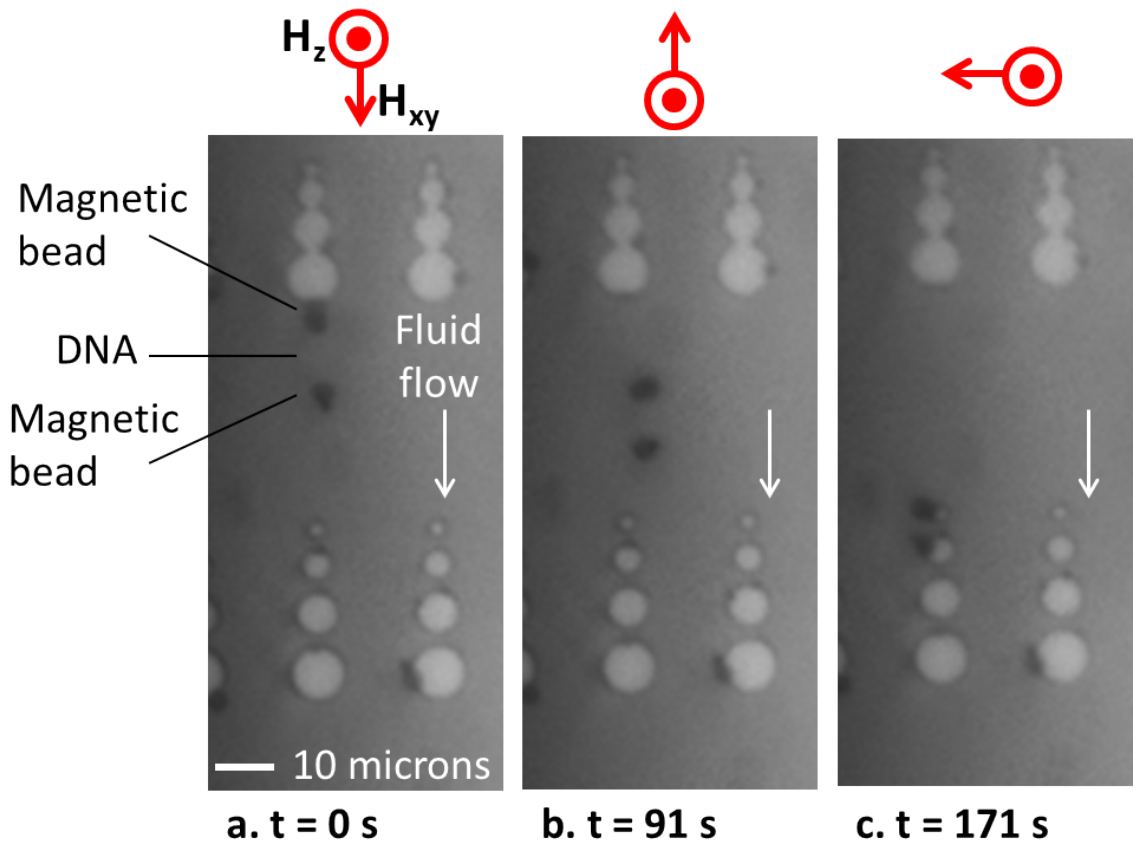

Figure 4.22: Lambda DNA tethered between two magnetic microbeads. (a) Fluid flow stretches the strand of DNA between the beads. (b) When the in-plane field is reversed, the trapped bead is released and the construct flows in the direction of fluid flow until (c) it is again captured by magnetic traps, this time with one bead on each trap.

resulting in a maximum possible stretch of 8.5 μm. The length at which the DNA will stretch can however be tuned with disk size and center-to-center spacing.

As mentioned above, this dual magnetic bead approach is challenging without a means of reducing bead-to-bead magnetic interactions. However, if some method of reducing these interactions, such as a more rigid structure between the two beads (e.g. DNA origami, see Conclusions and Future Work), were integrated into the experiment, then this approach would be a potentially useful method of manipulating both ends of the DNA structure on the magnetic tweezer platform.

4.4 Conclusions and Future Work

This chapter has demonstrated the ability of a magnetic tweezer platform to be utilized for force experiments with DNA. By measuring the extent of the stretch of lambda DNA in flow and comparing to previously reported DNA force-extension experiments [65, 69, 70], forces on the order of 1-5 pN were estimated.

One of the main benefits of this system is its potential for multiplexing experiments, which is a challenge to achieve with optical tweezers and conventional magnetic tweezers. Although some progress has been made toward multiplexing with conventional magnetic tweezers [8, 72], it is difficult to apply a completely identical force to all DNA strands when scaling up to much larger amounts of DNA. In the magnetic tweezer setup, the patterned traps are each identical and the external fields are spatially uniform across the region of the traps. This allows for the application of identical forces on each DNA strand on the platform.

In addition to DNA, this application could readily be extended to other types of biomolecules capable of conjugation to magnetic microbeads. An emerging field of DNA study is DNA origami, which consists of carefully designed scaffolds of folded single-stranded DNA held together by base-pair interactions and constructing larger (nm to μm sized) objects [73]. DNA origami structures range from unique shapes (such as stars and smiley faces with dimensions around 100 nm [74]) to moveable structures with mechanical functionality [75]. Just as with the double-stranded DNA presented in this chapter, a DNA origami construct can easily be attached to a magnetic microbead and manipulated on the magnetic tweezer platform, with the added functionality of the more rigid structure.

Chapter 5
Magnetic field landscapes and forces from zigzag wires

5.1 Introduction

The patterned micromagnetic traps presented in Chapters 1-3 are integrated into various devices to carefully manipulate, localize, and investigate biomolecules and cells. To exploit the full capabilities of the mobile magnetic wire traps, it is important to analyze the energy landscapes both on and around the wire structure for various external field configurations. Furthermore, for careful measurements (such as DNA stretching, Chapter 4), the validity of such measurements is ensured by understanding the characteristics and magnitudes of the forces applied to biomolecules. When utilizing the traps in experiments involving the manipulation of live cells (Chapter 6), an understanding of the forces applied is critical to ensure that they are sufficiently weak to not damage the cells.

Theoretical modeling (Chapter 3) has provided estimates of both the energy landscapes and the forces associated with magnetic traps along the zigzag wires. In order to validate this model, experiments were performed to carefully analyze energies and forces associated with the zigzag wire traps. The field-controlled dynamics of magnetic microbeads are utilized to characterize the energy landscape and the associated transformations that occur during remotely activated transport of the bead across the platform. These modifications to the trapping sites provide for the deterministic forces that guide and maneuver the individual beads.

5.1.1 Energy Landscapes

A high-speed camera (Phantom Miro M120, Vision Research) was used to capture data as various superparamagnetic microbeads were transported along the wires from vertex to vertex. Experiments are performed with superparamagnetic microbeads of mean diameter of 2.8 μm (Dynabeads cat. no. 14305D) and 11 μm (Spherotech cat. no. CM-80-10). It should be noted that there is a distribution in sizes of the beads that, for Dynabeads®, typically range between ±1.4% of the mean diameter of 2.8 μm [56, 76]. The Spherotech beads (used for Janus-type particles) vary in diameter between approximately 8.0 - 9.9 μm [77], although the specific bead used in the experiments presented in this chapter was measured to be 11 μm in diameter. Additionally, it is likely that the magnetic content in each bead is not exactly the same and thus the magnetic susceptibility may also vary from bead to bead [78, 79]. To reduce variations in the experiments presented, the same bead was used for each set of velocity and force measurements.

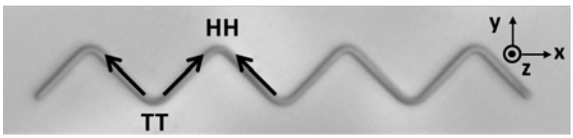

Figure 5.23: Zigzag wires are magnetized perpendicular to the length of the wire (in the y-direction). The resulting domain walls are located at the vertices and are either head-to-head (HH) or tail-to-tail (TT).

In transporting a superparamagnetic (SPM) bead from one vertex to an adjacent vertex on the zigzag wires (Figure 5.23), the external field $\mathbf{H}_{ext}$, with in-plane component $\mathbf{H}_{xy}$ and out-of-plane component $\mathbf{H}_z$, are tuned. These weak fields ($<$ 200 Oe) do not modify the general location of the domain walls in the zigzag wires in any significant way [48] and thus the associated domain wall fields $\mathbf{H}_{dw}$ are determined solely by the CoFe wire dimensions and initial magnetization. The moment induced in a SPM bead located at a given height above the wires is determined by the total field, $\mathbf{H}_{ext}+\mathbf{H}_{dw}$. In the absence of $\mathbf{H}_{ext}$, adjacent vertices and their associated $\mathbf{H}_{dw}$ fields act as primary trapping sites for the bead (see also Figure 3.13 in Chapter 3). If the out-of-plane field $\mathbf{H}_z$ is increased, the bead moment is proportionally determined by $\mathbf{H}_{ext}$ and the energy landscapes of adjacent head-to-head (HH) and tail-to-tail (TT) vertices steadily transform to become attractive and repulsive, respectively.

The relative contributions of $\mathbf{H}_{dw}$ and $\mathbf{H}_{ext}$ to the total field $\mathbf{H}_{tot}$ $(= \mathbf{H}_{ext} + \mathbf{H}_{dw})$ acting on the bead depend on the strength and configuration of the external field as well as the location of the bead relative to the vertex. For example, Figure 5.24 shows the relative contribution (in percentage of total field) of each field for various heights directly above the vertex for external field strengths $H_{xy} = 0$ Oe and $H_z = 70$ Oe. The external field begins to dominate for heights approximately 0.8 μm above the vertex and higher. Beyond a height of approximately 10 μm, the external field completely dominates ($H_{tot} \approx H_{ext}$). In the experiments presented, the beads settle to the surface of the platform due to gravity. The magnetic material in each bead is approximated to be located, on average, at the center of the bead. Therefore the height above the vertex is determined by the bead radius (in experiments below, the corresponding heights are 1.4 μm and 5.5 μm).

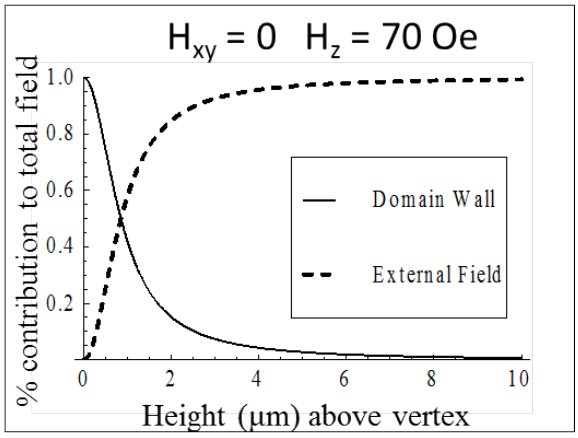

Figure 5.24: Contributions of domain wall (solid line) and external field (dashed line) sensed by a bead sitting directly above the vertex for external field strength $H_{xy} = 0$ Oe and $H_z = 70$ Oe. The relative contributions will vary depending on the bead height above the vertex.

The introduction of $\mathbf{H}_{xy}$ in the presence of $\mathbf{H}_z$, with $\mathbf{H}_{xy}$ oriented along the straight segment of the zigzag wire, further transforms the character and location of the traps. In particular, the primary traps weaken and shift away from the zigzag vertex to positions that lie between vertices. The resulting secondary traps (S) are crucial elements to the transport of the beads, which, depending on the depth of the trapping potential, can be slowed down, momentarily stalled, or completely halted in their movement between vertices.

Figure 5.25 illustrates the influence of $\mathbf{H}_{xy}$ and $\mathbf{H}_z$ on the energy landscape during transport of a bead (diameter 2.8 μm; susceptibility ~0.5 determined by SQUID measurements detailed in Chapter 2) along the wire between adjacent vertices. In Fig. 5.25 (a), the out-of-plane field $\mathbf{H}_z$ is reversed from +40 (dotted curve) Oe to -40 Oe (solid curve) for a fixed in-plane field $\mathbf{H}_{xy}$= 10 Oe. For $\mathbf{H}_z$= +40 Oe, the bead (dark circle) sits in a potential energy minimum (initial trap S_0) near the first vertex. When $\mathbf{H}_z$ is reversed to

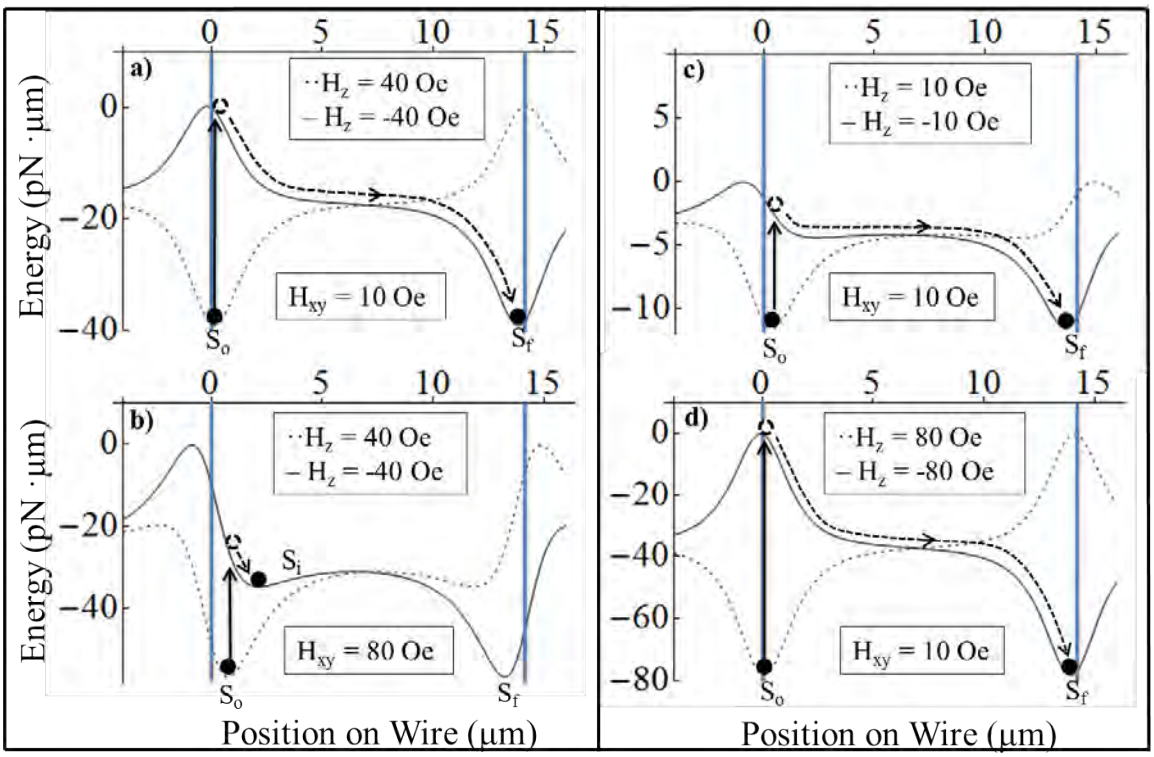

Figure 5.25: Potential energy landscapes for a 2.8 μm bead on a wire. Field configurations are (a) $\mathbf{H}_z$= ±40 Oe and $\mathbf{H}_{xy}$ = 10 Oe; (b) $\mathbf{H}_z$= ±40 Oe and $\mathbf{H}_{xy}$ = 80 Oe; (c) $\mathbf{H}_z$= ±10 Oe and $\mathbf{H}_{xy}$ = 10 Oe; (d) $\mathbf{H}_z$= ±80 Oe and $\mathbf{H}_{xy}$ = 10 Oe. In the presence of a positive $\mathbf{H}_z$ field, the initial position of the bead (expected position indicated by dark circle) is at the initial trap S_0. $\mathbf{H}_z$ is then reversed, causing the bead to move to the lower energy at S_f. The movement of the bead along the energy profile is indicated by arrows. S_0, S_i and S_f indicate initial, intermediate and final traps. Vertical lines (blue) indicate locations of wire vertices. The largest deviation of S_i and S_f from the vertices occurs at large H_{xy} values ($H_{xy} > H_z$).

-40 Oe, this vertex becomes repulsive and, since no intermediate traps are stabilized between the vertices, the bead moves steadily from this unfavorable energy state toward the neighboring final trap S_f located at the other vertex. In contrast, when $|\mathbf{H}_{xy}| > |\mathbf{H}_z|$, as in Figure 5.25 (b) ($\mathbf{H}_{xy}$ = 80 Oe, $\mathbf{H}_z$ = ±40 Oe), two secondary traps of different energy depths occur. The intermediate trap (S_i) nearer to the initial vertex is weakened by the repulsive contribution of $\mathbf{H}_z$ to the potential energy while the constructive superposition of $\mathbf{H}_z$ and $\mathbf{H}_{dw}$ at the second vertex renders a deeper secondary trap (S_f). For a given $\mathbf{H}_z$ and steadily increasing $\mathbf{H}_{xy}$, the intermediate trap S_i becomes more pronounced, transforming from a weak shoulder (Fig. 5.25 (c)) to a distinct trap (as in Fig. 5.25 (b)) that slows the bead's motion. For weak planar fields ($|\mathbf{H}_{xy}| \leq |\mathbf{H}_z|$), $\mathbf{H}_{xy}$ is not strong enough to

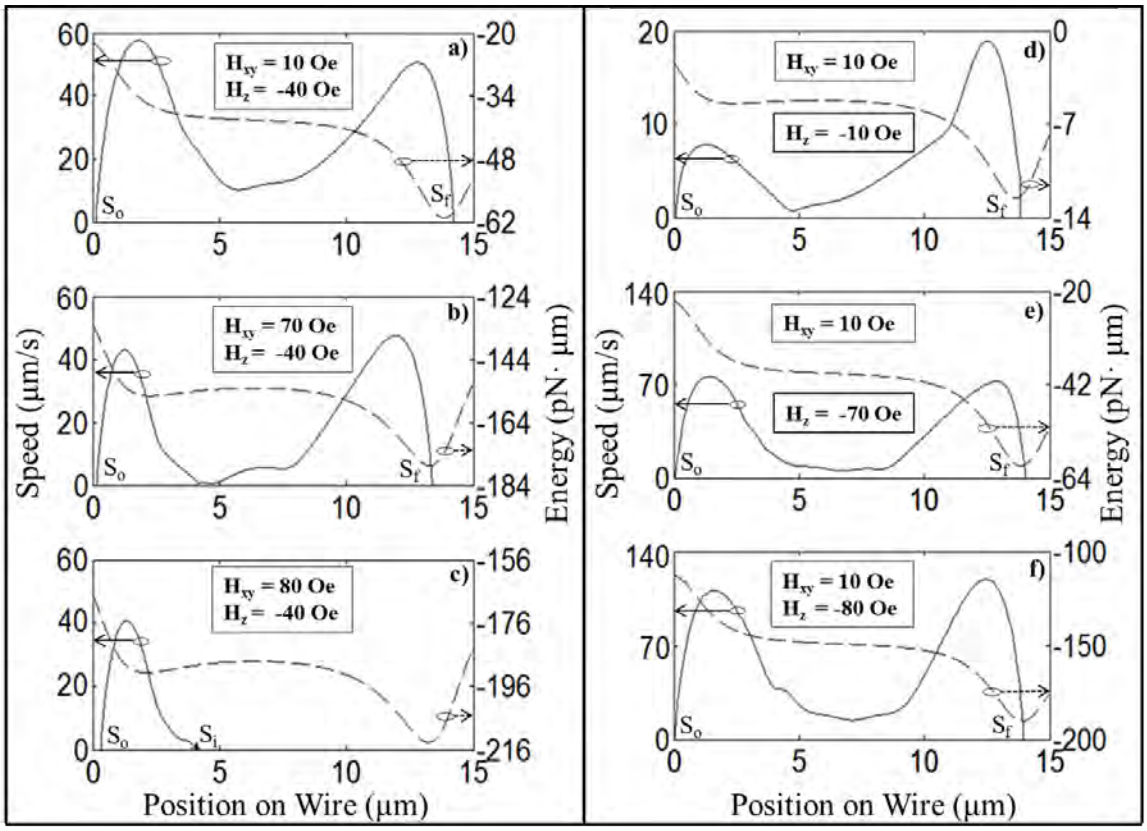

Figure 5.26: Experimentally measured speed of 2.8 μm bead moving along the wire (solid lines) and corresponding potential energies (dashed lines) calculated from the model. Plots (a-c) are for $\mathbf{H}_z$ = -40 Oe and $\mathbf{H}_{xy}$ = (a) 10 Oe, (b) 70 Oe, and (c) 80 Oe. As $\mathbf{H}_{xy}$ increases, an intermediate secondary trap S_i emerges, causing the bead to slow (b) or come to rest (c). Experiments on the same bead with $\mathbf{H}_{xy}$ = 10 Oe and $\mathbf{H}_z$ = (d) -10 Oe, (e) -70 Oe, and (f) -80 Oe do not result in intermediate traps and the bead reaches the destination vertex.

effectively influence the orientation of the bead's induced magnetic moment to generate a clear intermediate trap, as evidenced in Figure 5.25 (d) where $\mathbf{H}_{xy}$ = 10 Oe and $\mathbf{H}_z = \pm 80$ Oe.

As illustrated in Fig. 5.26, the energy profiles presented in Fig. 5.25 are consistent with the measured speeds of the bead. These speeds are determined by first tracking the particle location at each frame using a LabView tracking routine. From the resulting position vs time data, the velocity can then be determined for each point along the trajectory. In Figure 5.26, the calculated energy profile (dashed line) is plotted on top of the measured speed (solid line) of the bead as it moves from one vertex to the next with the given external field. Fig. 5.26 (a) confirms that for low $\mathbf{H}_{xy}$ (10 Oe) and $\mathbf{H}_z$ = -40 Oe, the bead initially

accelerates, reaching speeds of ∼60 μm/s as it moves away from the initial trap S_0, which is transformed to a repulsive site upon reversal of $\mathbf{H}_z$. The motion is then slowed as the bead encounters a flatter energy landscape before emerging and gaining speed as it moves toward the deeper final trap S_f where it is rapidly brought to rest. In Fig. 5.26 (b), however, $\mathbf{H}_{xy}$= 70 Oe ($|\mathbf{H}_{xy}| > |\mathbf{H}_z|$) and thus an intermediate trap arises, causing the bead to be temporarily localized before eventually escaping from S_i to reach target destination S_f. For $\mathbf{H}_{xy}$ = 80 Oe (Fig. 5.26 (c)), the intermediate trap is sufficiently deep that the bead is, as expected, permanently halted at S_i well before reaching the adjacent vertex.

In Figure 5.26 (d), $|\mathbf{H}_{xy}| = |\mathbf{H}_z|$ and the weak shoulder is seen in both the theoretical energy landscape and the slowing of the microbead about 5 μm from the initial vertex S_0. Fig. 5.26 (e-f) demonstrate experimental confirmation that when $|\mathbf{H}_{xy}| < |\mathbf{H}_z|$, intermediate traps are not evident, thereby enabling the bead to easily reach the next vertex.

5.1.2 Wire transport of 11 μm Janus particles

Similar experiments were performed with 11 μm beads on identical wires to those used to transport the 2.8 μm beads. The larger beads were utilized because the height of the magnetic material above the wire, on average, is higher (5.5 μm as compared to 1.4 μm for the 2.8 μm diameter beads), thus allowing for a particular aspect of wire theory, the effects of the height above the platform, to be studied. Furthermore, the outer structure of the larger beads is much more easily discernible under the microscope because they are Janus particles (see Chapter 2), with a half-shell Au coating. Thus the 11 μm beads also allowed for careful analysis of the exact orientation of the bead during its motion from one vertex to the next.

The 11 μm bead offers different responses compared to its 2.8 μm counterpart. These changes can be traced to the effective bead moment above the vertex. The 11 μm beads experience weaker effective fields and broader primary traps due to the large field gradients associated with $\mathbf{H}_{dw}$. The initial (S_{01}, S_{02}) and final (S_{f1} and S_{f2}) traps are located along the wire a few micrometers from the vertex center (Fig. 5.27); this distance increases with increasing $\mathbf{H}_{xy}$. On 14.5 μm long wires, the broadened primary traps approach each other

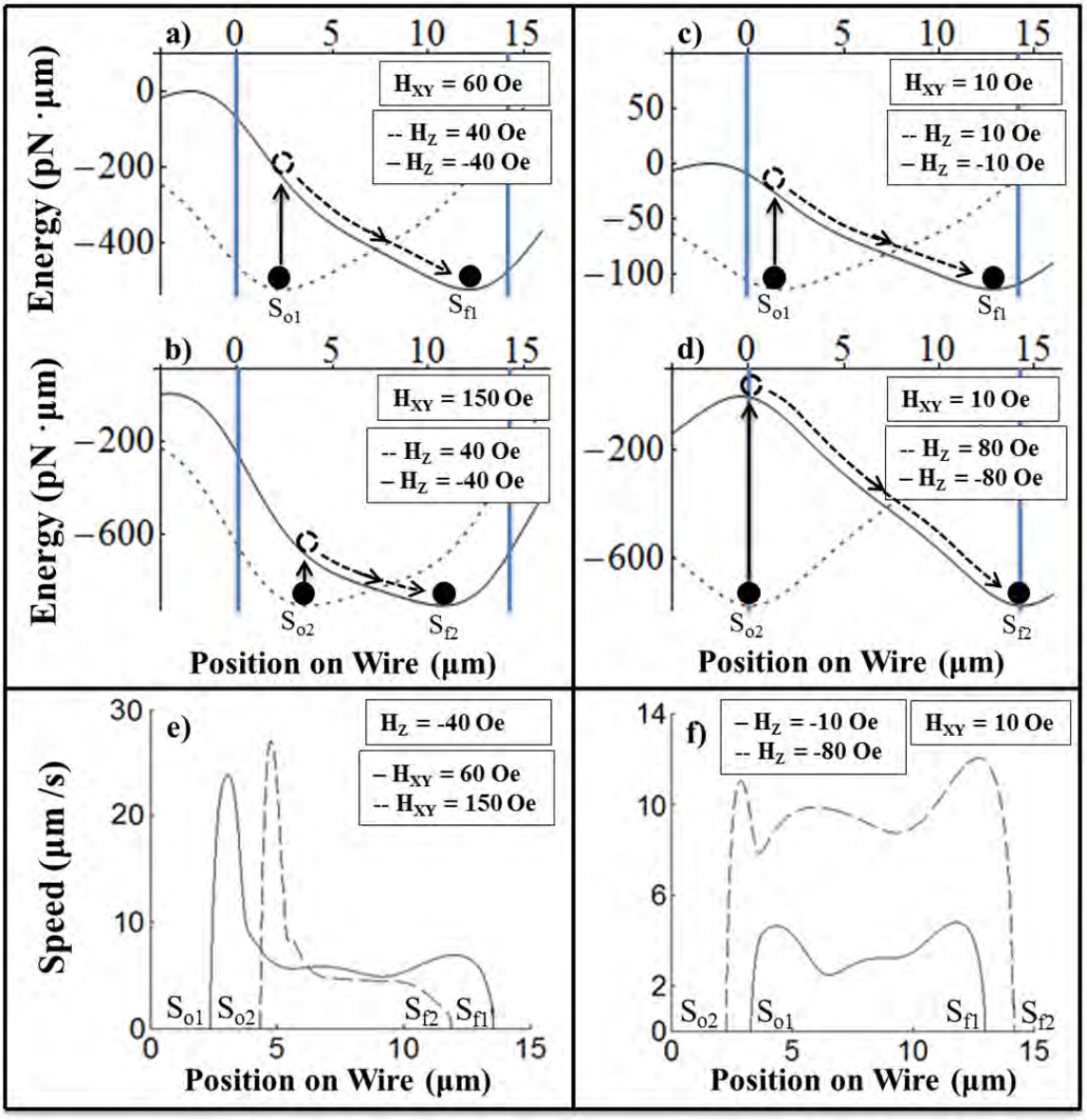

Figure 5.27: Experimentally measured speed of the 11 μm bead along the wire and corresponding potential energy landscape calculated from the model. (a) and (b): $\mathbf{H}_z = \pm 40$ Oe and $\mathbf{H}_{xy} = 60$ Oe and 150 Oe, respectively. (c) and (d): $\mathbf{H}_{xy}$=10 Oe and $\mathbf{H}_z = \pm 10$ and ± 80 Oe, respectively. Vertical blue lines indicate locations of wire vertices. Corresponding experiments determined particle speed for (e) $\mathbf{H}_z$ = -40 Oe and $\mathbf{H}_{xy}$ = 60 Oe and 150 Oe and (f) $\mathbf{H}_{xy}$= 10 Oe and $\mathbf{H}_z$ = -10 Oe and -80 Oe. As $\mathbf{H}_z$ increases relative to $\mathbf{H}_{xy}$ secondary traps shift closer to wire vertices and, as predicted in (a)-(d), the bead travels a larger distance. $S_{01}, S_{02}, S_{f1}, S_{f2}$ are the initial (S_{01} and S_{02}) and final traps (S_{f1} and S_{f2}) for different field values.

with no intermediate traps evident (Fig. 5.27 (a-d)). According to the model, for wires ~40 μm and longer, the initial and final traps are more separated, enabling an intermediate trap to emerge for the 11 μm sized beads (Figure 5.28).

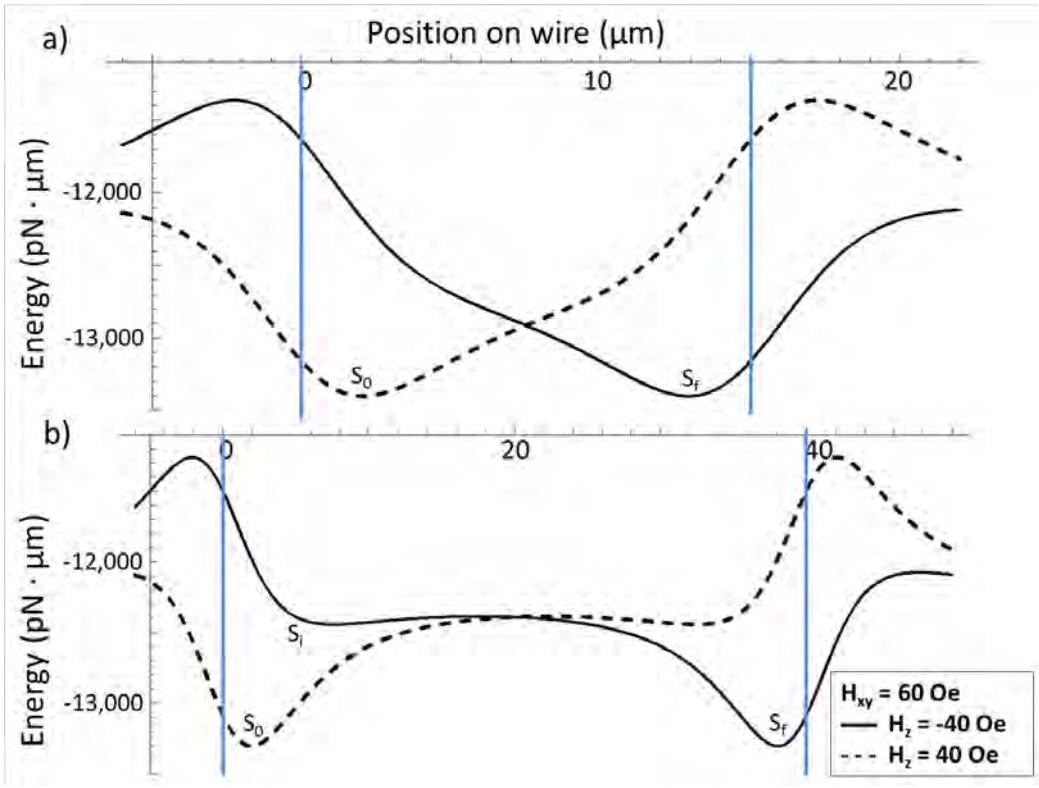

Figure 5.28: Theoretical calculations of energy landscapes for an 11μm bead. External fields $\mathbf{H}_{xy}$=60 Oe and $\mathbf{H}_z = \pm 40$ Oe for (a) 15 μm and (b) 40μm long wires. With longer wires, an intermediate trap S_i appears near the first vertex and between the initial (S_0) and final (S_f) positions of the bead, as occured in the case of the 2.8μm bead with the 14.5 μm long wires. Blue vertical lines identify the locations of the vertices.

The experimental results of Fig. 5.27 (e) and (f) for the 11 μm beads confirm that the corresponding translational speeds are smaller than those of the 2.8 μm beads for the same external field configuration. The smaller measured speeds and reductions in the distance traveled along the wire with increasing $\mathbf{H}_{xy}$ are in line with the model. Confirmation of theoretical predictions (Figs. 5.26 and 5.27) of the measured starting and ending locations, as well as recorded changes in the particle speed with applied fields for the different beads thus validates the models related to (1) domain wall-generated fields ($\mathbf{H}_{dw}$), (2) response of the energy landscape to $\mathbf{H}_{xy} + \mathbf{H}_z$ and (3) the magnetic properties of the beads.

The contrast between the light and dark regions of the Janus particles allows for a qualitative understanding of the orientation of the bead to differentiate between rolling and sliding motions. As shown in Figure 5.29, it was observed that the 11 μm Janus particles

exhibit an initial rolling motion prior to sliding along the wire from the first vertex (Fig. 5.29 (a) (i and v)) to the second vertex (Fig. 5.29 (b) (iv and viii)). Upon the reversal of $\mathbf{H}_z$, (Figure 5.29 (a) (i-iv) and (v-viii)), the entire bead is observed to rotate to align with the net field. It subsequently slides along the wire to reach the neighboring vertex, maintaining its orientation during this motion (Fig. 6.35 (b) (i-iv) and 6.35 (b) (v-vii)).

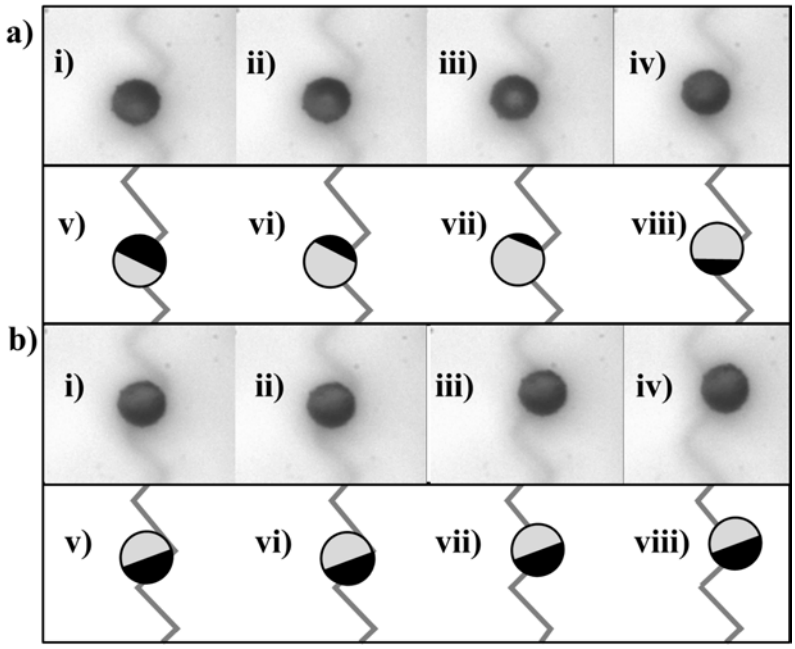

Figure 5.29: Janus particle transport. An 11μm Janus particle exhibits (a) rolling and (b) sliding motion during vertex-to-vertex transport. Microscope images (i-iv) are paired with schematics (v-viii) illustrating orientation of dark- and light (translucent)-colored regions during rolling and translational motion.

These findings reveal a field-induced rotational torque on the microbead immediately after the field is reversed. This torque in turn suggests the presence of a small ferromagnetic character for the bead, which is likely due to a size distribution in the embedded magnetic nanoparticles. Despite the weak ferromagnetic character, the overall field response of the beads is largely in agreement with that of a superparamagnetic microbead.

5.1.3 Forces

The velocity data obtained from experiments presented above (Figure 5.26) also allow for an experimental determination of in-plane forces exerted by wire traps on microbeads. Here a simple model is assumed, in which two opposing in-plane forces are exerted on the bead along the horizontal direction of motion. The magnetic force, which propels the bead along the wire from one vertex to the next, is opposed by the hydrodynamic drag force (see Chapter 3), which is determined by Stokes' Law (Equation 3.4), neglecting near-wall

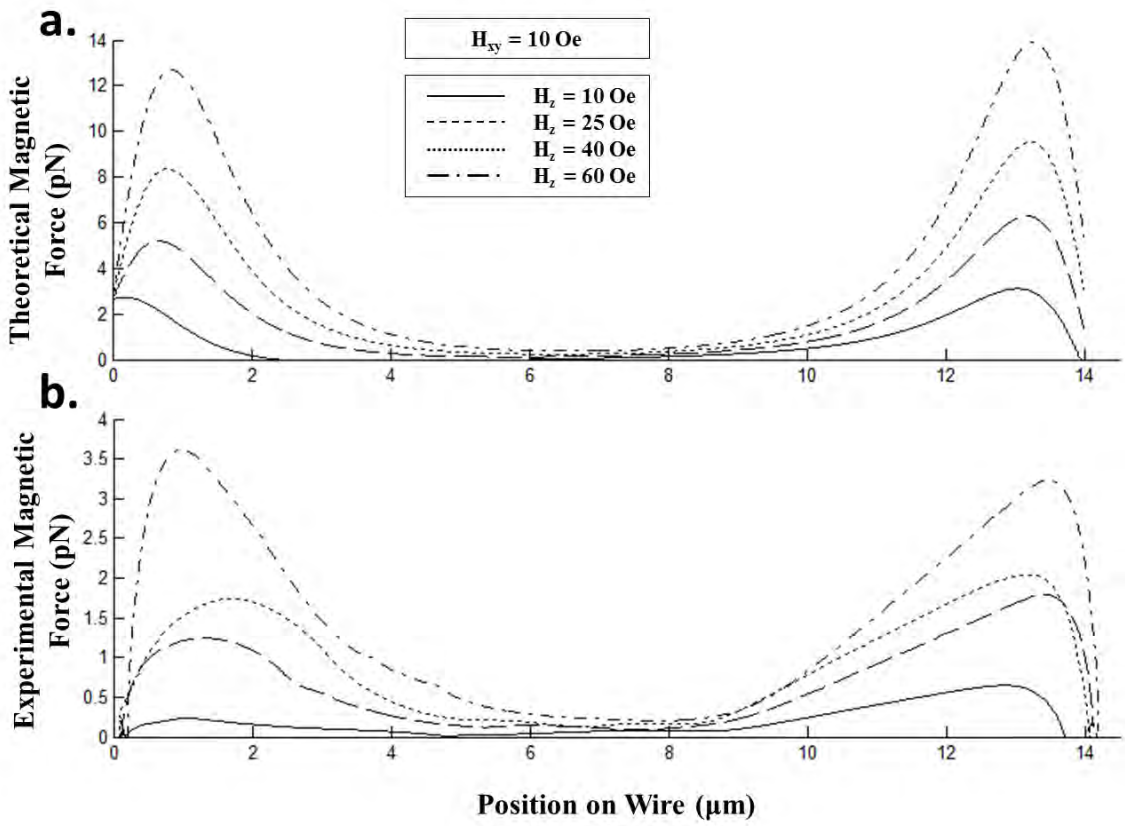

Figure 5.30: Magnetic forces associated with zigzag wires. (a) Theoretically calculated (see Chapter 3) in-plane magnetic force applied to a 2.8 μm microbead for field strengths H_{xy} = 10 Oe and H_z = 10, 25, 40, and 60 Oe. (b) Experimentally determined in-plane magnetic force applied to a 2.8 μm magnetic microbead in the same fields shown in (a). Both plots correspond to a 14.5 μm long CoFe wire.

effects. The position vs time data that is collected allows for calculation of velocity and acceleration of the bead along the trajectory, thus allowing determination of the net force on the bead. The magnetic force opposing the calculated drag force can then be evaluated, as shown in Figure 5.30 for a 2.8 μm bead during its motion along a 14.5 μm long CoFe wire.

The calculated magnetic force, given the magnetic potential energy determined by the point-charge theory (Chapter 3), is shown in Figure 5.30 (a) for external field strengths H_{xy} = 10 Oe and H_z = 10, 25, 40, and 60 Oe. Larger forces are predicted near the vertices with weaker forces along the wire between the vertices. The experimentally determined

magnetic forces corresponding to these fields are shown in Figure 5.30 (b). Qualitatively, the experimental graph of Fig. 5.30 (b) shows a striking resemblance to those calculated through the point charge method (Fig. 5.30 (a)).

Though the force graph qualitatively corresponds well to the theoretical predictions, there is approximately a 20-30% difference in the values of the experimentally determined in-plane forces, which were found to be as high as about 3 pN in this study. The theoretically predicted forces were determined to be as high as about 14 pN. These differences could arise from a number of factors. As discussed previously in this chapter, the Janus particle experiments revealed an initial rolling motion in the trajectory, which we were unable to detect prior to this study and is thus not accounted for in the theory. The extent of this rolling motion depends on the initial orientation of the magnetic moment of the bead (as determined by the external field) as well as the diameter of the bead. The friction coefficient, μ_k, will also be different depending on whether the motion is rolling or sliding motion [80]. The resulting near-wall effects, which were not accounted for in the theoretical approximation, will be different in each portion (rolling vs sliding) of the trajectory and will affect the value of the drag force.

The forces that have been determined through these experiments are on the order of magnitude (1-10 pN) of forces associated with cellular components [63, 81], which makes this setup ideal for safely manipulating cells and probing the internal cellular structure. Similarly, such forces are capable of stretching double-stranded DNA to nearly their full contour length [63, 65] in what is known as the low-force regime. However, forces an order of magnitude larger would be required to perform studies analyzing the overstretching transition of double-stranded DNA, in which molecules are observed to extend beyond their contour lengths [65]. Although an upper limit has not been experimentally determined, higher forces are achievable on this platform, most readily by increasing the applied external magnetic field.

5.2 Potential energy landscapes associated with magnetic disk traps

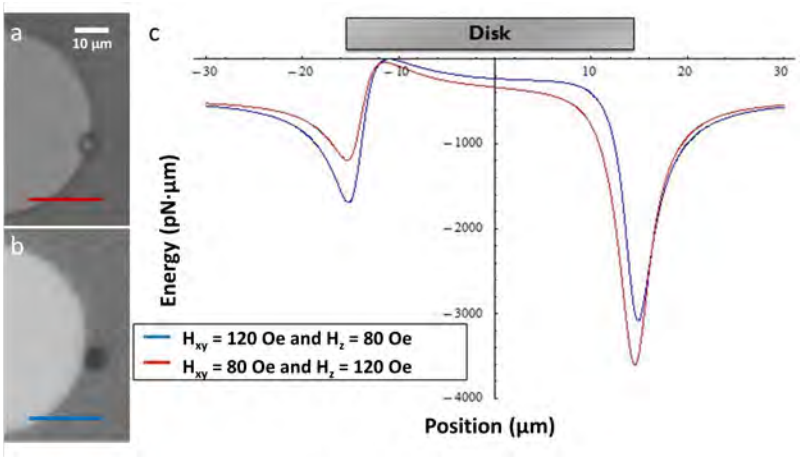

Figure 5.31: Magnetic disk trap localization. Microscope images of a 2.8 μm bead in external field (a) H_{xy} = 80 Oe and H_z = 120 Oe and (b) H_{xy} = 120 Oe and H_z = 80 Oe. (c) Corresponding magnetic potential energy plots are shown for these field configurations. As predicted, the beads sit nearer to the center of the disk when $H_{xy} < H_z$ and further outside the edge of the disk when $H_{xy} > H_z$.

To further the studies shown here and for the biotechnological applications of Chapter 4 and Chapter 6, experiments have begun similar to those described in this chapter to validate the theory currently used to map out potential energy landscapes on Permalloy magnetic disk traps (see Chapter 3). Preliminary studies have shown that the position of a 2.8 μm bead localized on a 30 μm diameter disk will vary depending on the external field configuration (Figure 5.31). In Fig. 5.31 (a), the bead is held in an external field in which the out-of-plane field is higher than the in-plane field (H_{xy} = 80 Oe and H_z = 120 Oe). In Fig. 1 (b), however, the magnitudes of the two fields are reversed, such that $H_{xy} > H_z$. This change will adjust the direction of the bead's internal magnetic moment as well as the exact location of the trap, as shown in Fig. 5.31 (c). As is visible in the images, the bead is held closer to the center of the disk in Fig. 5.31 (a) and further outside the edge of the disk in Fig. 5.31 (b). The measured shift in the position of the center of the bead is 0.35 μm. As shown in Fig. 5.31 (c), this slight shift in position is predicted in the theory to be approximately 0.32 μm. This demonstrates that, as with the zigzag wires, the trap locations on the disks can also be adjusted by tuning the external magnetic fields. To further validate the theory, experiments that utilize high frame rate videos (~10,000 fps) to track the position of 2.8 μm microbeads upon reversal of the direction of the out-of-plane field, thus manipulating the particle away from the disk, can be used to determine the potential

energy landscapes involved with particle manipulation on the disks.

5.3 Conclusion and future work

The zigzag wires presented in this study show promise as one of a handful of micro-magnetic methods to capture, transport, and spatially localize targeted molecules. The work described in the present chapter has allowed for careful experimental mapping of the energy profile of these traps to test the current theoretical understanding of potential energy landscapes and associated forces. The experiments confirm that the theory is capable of predicting energy landscapes very well for various wire and bead sizes. The experimental force determination provides insight into the theoretical approximations that may need improvements, for example in accounting for the rolling motion at the start of the trajectory. This data offers a pathway for future modeling, which would include near-wall frictional effects that will differ depending on whether the bead is rolling or sliding [80].

The studies in this chapter probed energy landscapes exclusively along the length of the wire (Figure 5.32 (a)). However, both the point charge model and experimental trials confirm that deterministic forces on a bead are not constrained to the wire conduit [24]. This feature has many advantages because a silicon chip could be patterned with not one but many zigzag wires in an array (Figure 5.32 (b)), and magnetic beads may then be moved in various directions, such as that shown in Figure 5.32 (c). Within the present model, the trajectories will be remarkably similar to those observed and reported in this chapter, since only the distance between the vertices will change. The magnetic potential energy plots for two different distances are shown in Figure 5.32 (d-e). The path shown in Fig. 5.32 (e) is slightly longer, which simply changes the location of the final trap. One advantage of this is that beads may be manipulated in any direction across an array of wires rather than being limited to vertices along the length of a single wire. Furthermore, it was demonstrated earlier in this chapter that intermediate traps will form along the direction of the applied in-plane field for $|\mathbf{H}_{xy}| > |\mathbf{H}_z|$. Due to these intermediate traps, there are numerous locations at which a microbead may be localized on the array. These trapping

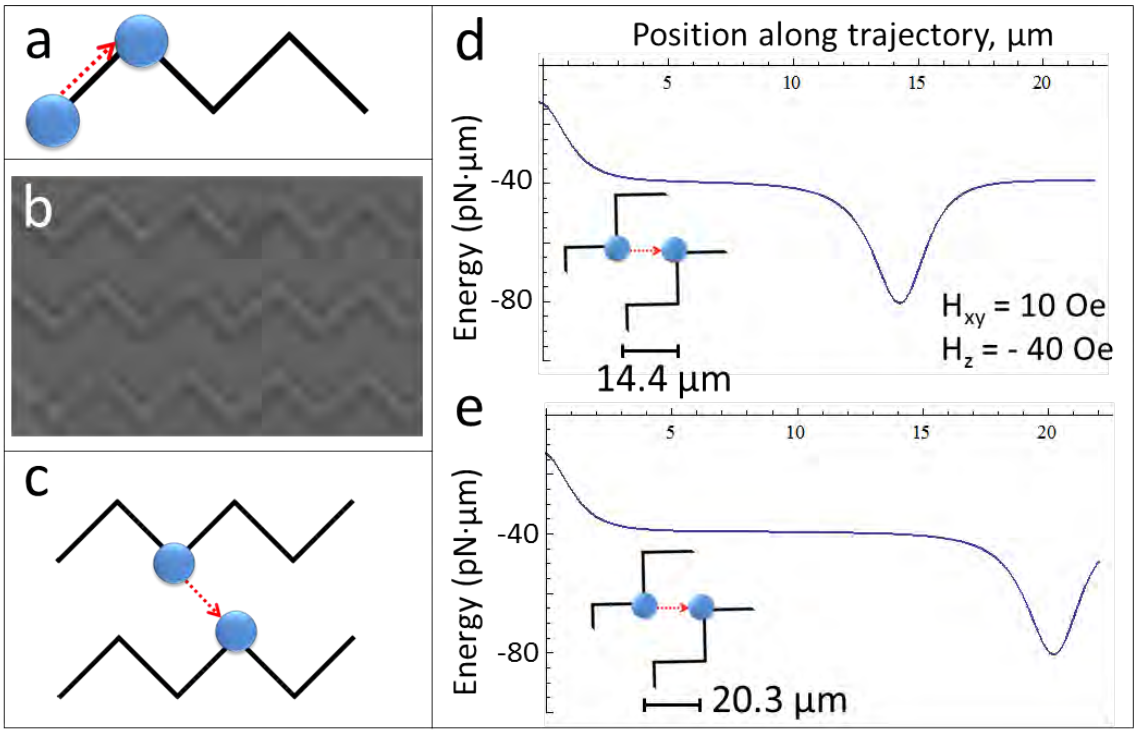

Figure 5.32: Zigzag wire transport capabilities. (a) Schematic of trajectories analyzed during this chapter. (b) Microscope image shows an array of CoFe wires patterned onto a surface. (c) Theory and experiments show that deterministic forces are not constrained to the wire itself (e.g. the bead could jump to a vertex of a nearby wire). Theoretical potential energy curves for a particle moving to the vertex of a nearby wire (d) if the spacing is 14.4 μm and (e.) if the spacing is 20.3 μm.

sites are not limited to the domain wall at the vertex. They may be situated along any path from one vertex to a neighboring vertex, both along the wire and outside the conduit. The locations for bead localization may be tuned by adjusting the strength and direction of the in-plane and out-of-plane components of the external field. The extent of this control shows promise for new micromagnetic trap designs based on the zigzag wire model that will be adaptable to more diverse biological applications.

Chapter 6
Integrating magnetic traps with nano- and micro-channel electroporation

Gene transfection into cells is an extremely important and broad field. In human cells, gene therapy is being investigated for the treatment and control of diseases such as cancer [82, 83, 84] by probing the cellular response to injections of various concentrations of molecules. It is capable of detecting targeted cellular contents such as mRNA and proteins, to better understand the purpose of such proteins, especially in contributing to diseases. The importance of gene transfer is not limited, however, to biomedical purposes. DNA transfer to plant cells allows for genetic modification such as herbicide and insecticide resistance and plant hybridisation [85]. Furthermore, bacterial cells naturally replicate DNA and synthesize proteins, and thus can be used as tiny "machines" to amplify DNA or create proteins [86, 87]. The strides made in the field of gene transfection are not possible without techniques to rapidly and effectively deliver genes and other entities into cells. To conduct statistically significant research, what were once single-cell experiments must be advanced to become more high throughput techniques. In this section, the incorporation of magnetic traps with methods of cellular transfection to enable high-throughput, multiplexed outcomes will be addressed.

6.1 Cellular injection techniques

In vivo, a cell depends on its phospholipid bilayer cell membrane (schematic shown in Figure 6.33 [88]) to regulate intake of extracellular material. The hydrophilic-hydrophobic-hydrophilic structure of the membrane ensures that water soluble materials cannot easily penetrate the cell. Thus genes, drugs and proteins are unable to easily enter a healthy living cell. The challenge of cellular injection techniques is therefore to penetrate this natural barrier and introduce foreign substances into the cell while preserving cell structure and vitality.

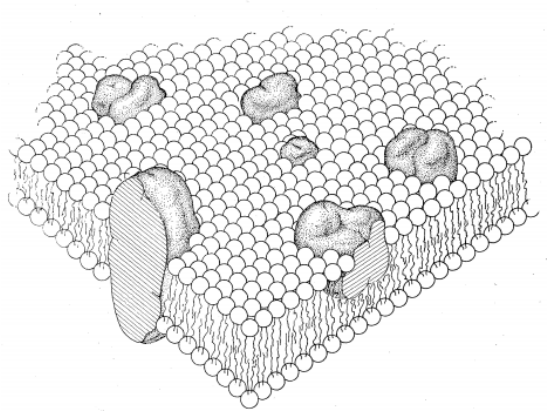

Figure 6.33: The cell membrane of a eukaryotic cell consists of a phospholipid bilayer in which hydrophobic tails are protected on either side by hydrophilic heads. Image from Singer and Nicolson, *Science*, 1972.

A wide variety of established techniques capable of introducing biomolecules into cells exist. They include, but are not limited to, viral vectors [89], physical bombardment [90], microinjection [20, 91], and electroporation [37, 40, 92, 93, 94, 95, 96]. These and other techniques are utilized to inject genes, drugs, fluorescent dyes, and other molecules into cells. To probe cellular response over time, it is critical for these techniques to have low cell mortality rates. It is also desireable for a technique to have the ability to control dosage, to be easily and inexpensively operated, and to deliver molecules into many individual cells simultaneously. Two common techniques, microinjection and bulk electroporation, will be briefly addressed below. The techniques of microchannel and nanochannel electroporation will then be presented.

6.1.1 Microinjection

Microinjection is one of the few techniques that allows for precise dosage injection into a single cell. For this process, a microneedle physically penetrates the membrane of a cell and pushes pre-loaded liquid containing a controlled amount of fluorescent dye, DNA, or

proteins through the needle tip and into the cell [91]. The cell may be attached to the surface of a petri dish (Figure 6.34 (a-c)) or suspended in solution with a micropipette (Figure 6.34 (d)). An optical microscope is used to view the experiment while micromanipulators attached to the injection needle allow for precise positioning of the needle, which permits the researcher to inject into either the nucleus or the surrounding cytosol.

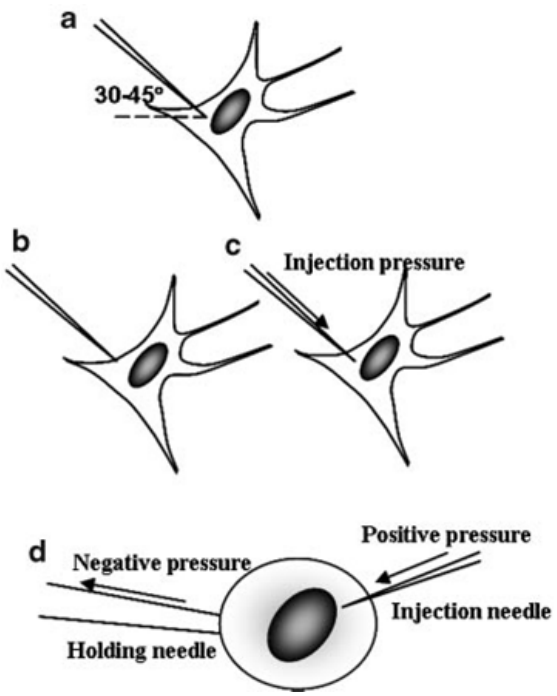

Figure 6.34: Single-cell microinjection. Microinjection may be performed on adhered cells (a-c) or suspended cells (d) localized with negative pressure through a micropipette. In both cases, an injection needle uses positive presssure to inject into cytosol or the nucleus. Image from Zhang and Yu, *BioEssays*, 2008.

Injection pressure and time must be carefully regulated in order to control the injected volume; the ability to do so and thus carefully regulate dosage is the most important advantage of this technique. A critical drawback, however, is that it is inherently a single-cell technique that requires manual injection for each cell. Some progress has been made to automate the technique and increase the rate of cell injection [20]. However, it nonetheless remains low-throughput as compared to other cellular injection techniques.

6.1.2 Bulk electroporation

The single-cell nature of microinjection suggests a need for techniques that can transfect large numbers (10^3 to 10^6) of cells simultaneously. Bulk electroporation, a commercialized lab technique [36], uses high voltage electric pulses applied between two electrodes in a cuvette filled with cells in solution to simultaneously transfect up to millions of cells. For any given cell in solution to porate, the voltage pulse must be high enough to increase the transmembrane potential of that cell past a critical value (shown to be around 200 mV [97]). The magnitude of this threshold voltage varies depending on the size and type of cell.

The resulting pores that form are likely on the order of tens to hundreds of nanometers in size [92], and small molecules will traverse the membrane via the pores to enter the cytosol. Molecules that are very small, such as propidium iodide dye (668 Da) diffuse through the pores unaided. Larger molecules, such as long strands of DNA (>4 kDa), however, are endocytosed into the cell in vesicles when electroporation takes place. To transfect any particular molecule into the cells with bulk electroporation, that molecule must be added to the solution containing cells in the cuvette. Following transfection of a molecule, it is critical that the cell membranes heal in a matter of minutes after the voltage is removed.

Although it is fast, easy, and transfects many cells simultaneously, there are two serious drawbacks to bulk electroporation. First, unlike microinjection, the dosage is almost completely uncontrolled. It is possible to somewhat increase the affected area of the cell surface by increasing the voltage (once above the critical applied voltage) and it is also possible to modify the extent of poration by adjusting the duration and number of pulses [37]. However, there is no precise control; the location of each cell in the cuvette contributes more than anything else to the extent of poration of each individual cell for a given voltage. As such, each cell will be transfected with a different dosage. The second major drawback of bulk electroporation is also highly location-dependent. A large fraction of the cells, particularly those near the electrodes, are lysed or damaged due to the non-uniform and hazardous electric fields. Indeed, electroporation can also be used as a cell lysing technique called electrical lysis [96, 98, 99]. The resulting high cell mortality rates in bulk electroporation limit the usefulness of this technique for clinical applications. The three critical aspects of transfection: namely, efficiency, gene delivery to targeted cells and cell viability, are not guaranteed with the bulk electroporation approach [41].

6.1.3 Nano- and micro-channel electroporation

The research presented here uses electroporation techniques to deliver molecules into cells but rather than bulk techniques, methods referred to as nano-channel and micro-channel electroporation are employed. In general, these methods [18, 41, 94, 100] often focus the voltage pulse through either a microchannel or a nanochannel onto an individual cell in the

channel or pressed directly against the channel. Cells can be manipulated and localized by optical tweezers [18], dielectrophoresis [101], vacuum [94, 102], or microfluidics [19]. Many micro- and nanochannel devices are single-cell or very low throughput techniques. However, in this research magnetic manipulation techniques are integrated with micro- and nanochannel electroporation devices, which allows for cell localization and manipulation during the experiment. These devices are consequently automated and high-throughput. The most beneficial aspects of electroporation, (1) simplicity of use, (2) ability to transfect into most cell types, and (3) high-throughput transfection are all preserved in this approach. Importantly, these techniques additionally overcome many of the inherent drawbacks of bulk electroporation including achieving a sharp reduction in cell mortality.

The use of magnetic manipulation techniques also provides a foundation for incorporation with downstream analysis in a combined device that may include on-chip labeling, sorting, and analysis.

6.2 Micro-channel electroporation

6.2.1 Introduction

Microchannel electroporation (MEP) provides a means to overcome the drawbacks associated with bulk electroporation by offering a gentler environment where each cell is porated under more controlled conditions [39, 41]. Devices often confine individual cells at micro-scale pores, resulting in electric field strengths across each pore that are orders of magnitude larger than those achieved by bulk electroporation [18, 95]. Thus safe, low voltages (<10 V) are sufficient for cell poration [40, 102, 103]. Furthermore, delivery into the cells is confined to regions determined by pore size, allowing for a more controlled environment than in bulk electroporation.

Currently, most MEP designs highlight single-cell electroporation [38, 39, 40, 104], which is inadequate for clinical applications that require high throughput. Recent approaches [38, 105] include microfluidic electroporation devices, which often operate in a sequential manner and thus are less conducive to scale-up for clinical applications [106]. On the

other hand, a technique called 3D microchannel electroporation (3D MEP) [41, 102, 107] is capable of achieving high throughput by handling thousands of cells on a planar membrane with an applied electric field in the vertical direction. MEP membranes could be a carefully patterned micro-pore array [94, 100, 102] or randomly distributed micro-pores [93].

A critical requirement for 3D MEP is an efficient approach to manipulate and localize large numbers of individual cells over an array of micro-pores. Previously reported 3D MEP studies utilize vacuum to trap cells at the micro-pores by applying a negative pressure underneath the MEP chip [93, 94, 100, 102]. This method, while efficient in cell-trapping, is however difficult to optimize in regards to trapping forces, leading to either poor alignment due to low pressures or serious cell membrane damage due to high pressures [108]. An alternative method of alignment of cells is optical tweezers, which precisely places individual cells at targeted micro-pores. However, the technique has limited throughput and laser-induced Joule heating can be a barrier as it contributes to cell damage and mortality [106].

For the micro-electroporation studies presented here, a versatile 3-dimensional magnetic tweezers based system capable of realizing the three important aspects: (a) individual-cell based electroporation, (b) high throughput transfection, and (c) retention of cell viability, was developed. To efficiently place individual cells at a single micro-pore, the magnetic tweezer platform is utilized to manipulate and align magnetically labeled cells. The multiplexed operation simultaneously controls the locations of tens of thousands of cells. The weak magnetic fields do not generate heat nor adversely damage the cells, thus removing cell damage concerns that arise with the optical tweezers and vacuum generated force manipulation schemes. The schematic for magnetic tweezers based 3D MEP is shown in Figure 6.35. The device is sized to fit within the electromagnetic setup (Fig. 6.35 (a)). The 3D MEP device (Figure 6.35 (b)) utilizes a bottom Au electrode that covers the entire base of the device. A PDMS spacer on the surface holds solution containing the molecule to be injected. On top of the PDMS spacer is the 3D MEP chip, a silicon wafer with an array of micron-sized pores etched through it. Aligned with the pore array is an array of magnetic disks (Figure 6.35 (c)) capable of localizing magnetically labeled cells directly over the pores. The disks also allow for manipulation of cells before and after transfection.

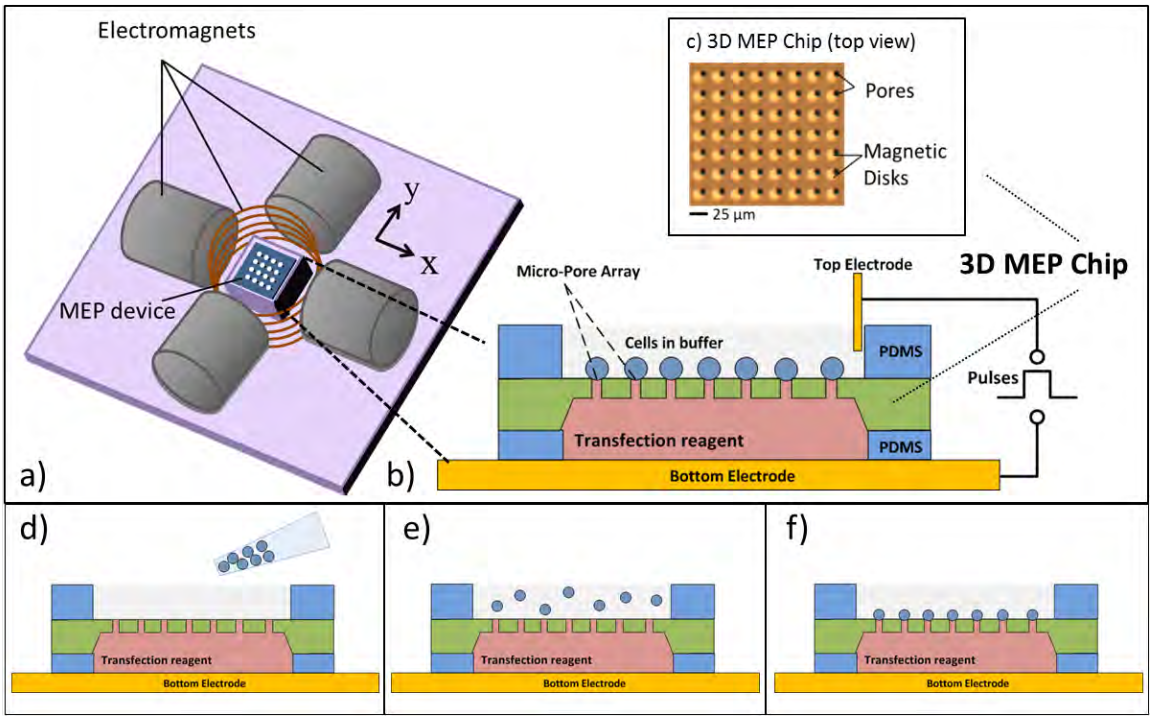

Figure 6.35: The 3D MEP- magnetic tweezer system setup. (a) The entire 3D MEP-MT device fits in the electromagnet stage described previously. (b) Schematic of the 3D micro-electroporation scheme. A gold substrate serves as the bottom electrode. A PDMS spacer holds the transfection reagents in solution. Above this spacer sits the 3D MEP wafer with etched pores and magnetic disks. Another PDMS spacer sits on top of the 3D MEP wafer to hold cells in solution, and a platinum electrode is placed in the solution. (c). Micrograph of a 3D MEP wafer, showing permalloy disks aligned with 5 micron diameter pores. Cell seeding is performed by simply (d) pipetting cells in PBS buffer solution into upper chamber and (e) allowing them to settle due to gravity with magnetic fields turned on so that they (f) are gently pulled to trap locations, aligned with the pores.

Seeding and aligning cells in the high-throughput device is rapid. A pipette is used to drop a predetermined concentration of cells in solution into the upper chamber of the device (Fig. 6.35 (d)). The cells are allowed to settle (Fig. 6.35 (e)) with magnetic fields turned on such that as the labeled cells approach the surface, they are gently pulled to pore locations at the periphery of the magnetic disks (Fig. 6.35 (f)). For example, if pores are aligned on the +x side of disks, $\mathbf{H}_{xy} = 50$ Oe along +x direction, and $\mathbf{H}_z = 50$ Oe in +z direction will guide the cells to desired locations above the pores with no further user interaction necessary to align the cells with micro-pores. Alignment efficiency and results will be described in more detail for both low-density and high density (high throughput) experiments in this device.

6.2.2 Fabrication

The processes used to create 3D MEP chips are more involved than the techniques described in Chapter 2 and will be described here. Two different chips, the low density micro-pore array and the high density micro-pore array, have been studied. Fabrication of these chips was done in collaboration with Mr. Lingqian Chang.

Low density micro-pore array chip

The first magnetic tweezers assisted 3D MEP design, termed the low density micro-pore array, has a high density of magnetic traps (~150,000 disks/cm^2) but a relatively low density of pores (~1,000 pores/cm^2). This micro-pore array chip was developed to test the performance of the magnetic tweezers on single-cell manipulation for 3D MEP.

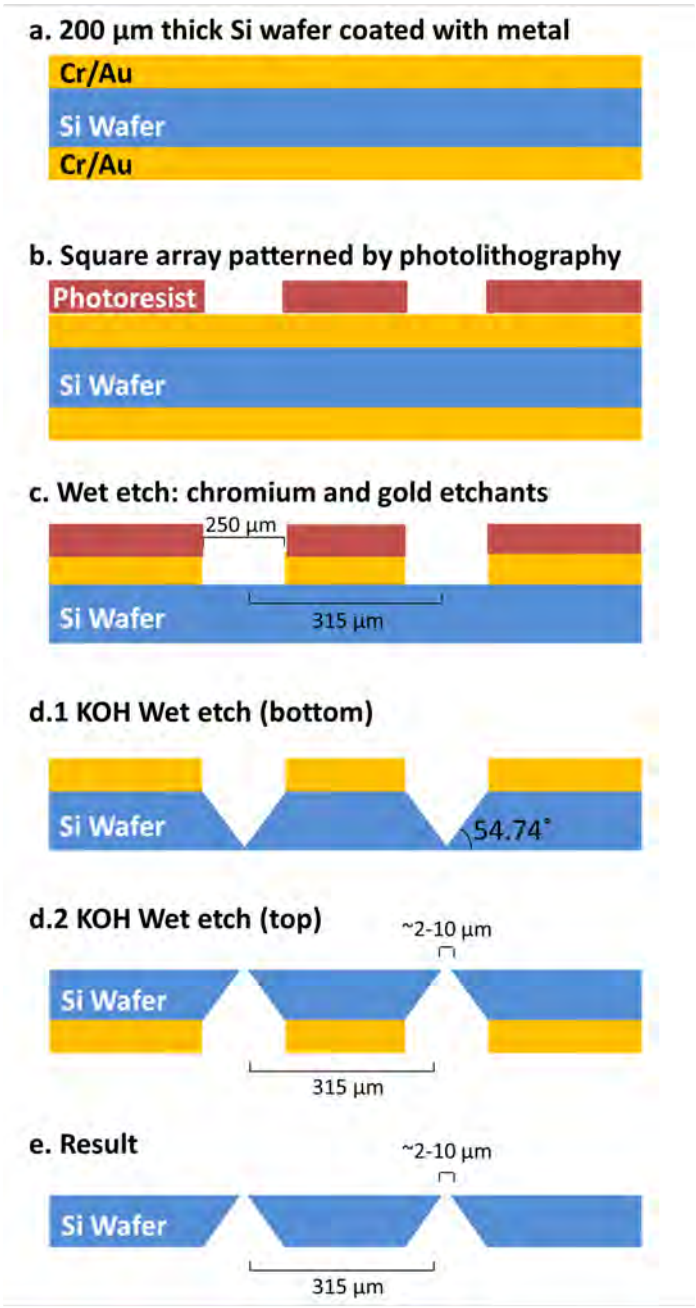

Figure 6.36: Fabrication procedure for the low density micro-pore array chip. Fabrication done in collaboration with Mr. Lingqian Chang

To fabricate the low density micro-pore array chip, pores are etched with a wet etch procedure (Figure 6.36). First, a metal mask layer (Cr/Au, 30

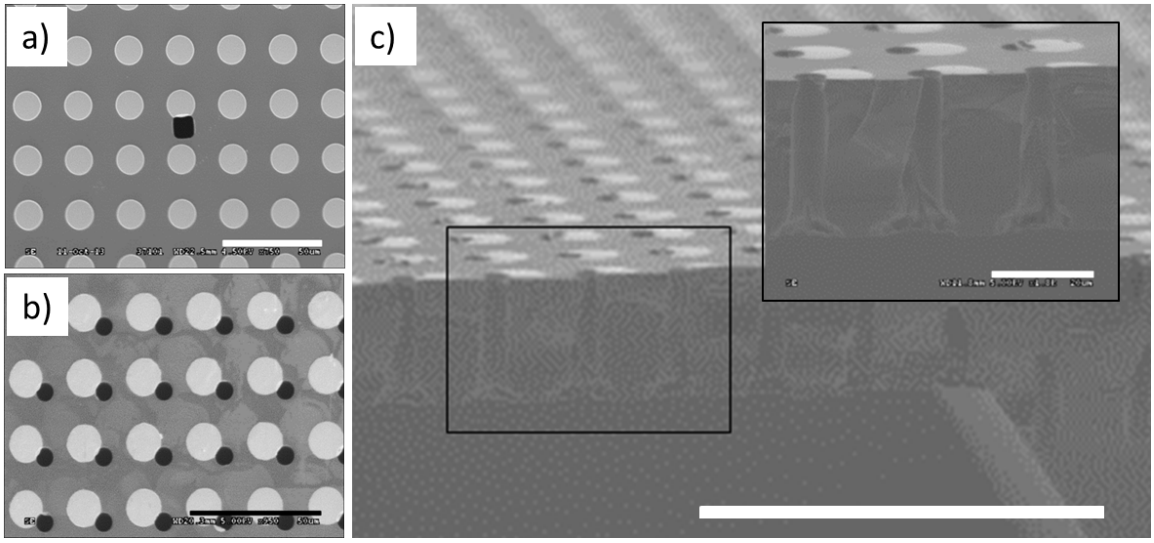

Figure 6.37: SEM micrographs of two types of 3D MEP chips. (a) the low density MPA chip shows one single square-shaped micro-pore (black) and a magnetic disk array (white). Scale bar = 50 μm. (b) On the high density micro-pore array chip, each magnetic disk is aligned with a micro-pore. Scale bar = 50 μm. (c) The cross section of the high density micro-pore array chip shows pores in the region of the terrace structure micro-trench. Scale bar = 100 μm. Insert shows zoomed-in cross section of three individual micro-pores, with scale bar = 20 μm.

nm/100 nm, E-gun evaporation, Denton DV 520A) is deposited onto both sides of a ~200 μm thick silicon substrate ((100) orientation, Double Side Polished) (Fig. 6.36 (a)). An array of squares (each square 250 μm in width, 315 μm center-to-center distance) is patterned on the mask layer by photolithography (S1813, Shipley, 1.4 μm, Fig. 6.36 (b)), followed by the use of chromium (CR-7S) and gold (GE-8111) etchants to transfer the square array to the metal mask (Fig. 6.36 (c)). The masked silicon wafer is placed in a KOH wet-etch tank (45%, 80°C) for several hours. Due to the anisotropic etch properties of silicon for each crystal plane, an array of inverted pyramid pits, with an angle of 54.7° to the (100) plane are created by the etch on the square array (Fig. 6.36 (d.1)) while the opposite surface of the wafer is simultaneously thinned (Fig. 6.36 (d.2)), resulting in a small square-shaped micro-pore hole (approximagely 1-10 μm length) at the bottom of each pyramid-pit (Fig. 6.36 (e)). The metal mask layer was removed by using both CR-7S and GE-8111. An SEM image of the square-shaped pore of the low-density micro-pore array chip is shown in Figure 6.37 (a).

Following the micro-pore array chip fabrication, the magnetic trap array (each circular

trap 15 μm in diameter, 50 nm thick, with 25 μm center-to-center distance) was fabricated with photolithography (see Chapter 2).

A SiO_2 dielectric film (~200 nm) was deposited on the chip by PECVD (Plasma Therm 770 SLR) for electrical isolation during the process of electroporation. The entire chip consists of an array of 5 μm pores with 315 μm center-to-center spacing, resulting in ~1,000 micro-pores per 1 cm^2, capable of transfecting ~1,000 cells under ideal trapping efficiency.

6.2.3 High density micro-pore array chip

The steps involved in the fabrication of the high density micro-pore array chip are shown in Figure 6.38. The first steps (Fig. 6.38 (a-c)) are similar to the protocol of the low density micro-pore array chip. However, a much larger array of squares is first etched from one side in KOH (each square ~500 μm - 800 μm in width), creating micro-trenches (Fig. 6.38 (d)). A micro-pore array (each pore 5 μm in diameter, 25 μm center-to-center distance) is then patterned on the opposite side of the silicon wafer using photolithography (SPR200-7, 6 μm thick, Fig. 6.38 (e)). Deep Reactive Ion Etch (DRIE) is used to etch the micro-pore array through the bottom of the terrace array (6.38 (f)). Bosch process (SF6: 12s/100 sccm gas flow/700 W ICP power/40 W RF power/30 mT APC pressure; C4F8: 7s/100 sccm gas flow/700 W ICP power/10 W RF power/30 mT APC pressure), with etch rate ~3 μm/min, is applied for DRIE (Oxford Plasma Lab 100). The length of the vertical micro-pores was determined

Figure 6.38: Fabrication procedure for the high density micro-pore array chip. Fabrication done in collaboration with Mr. Lingqian Chang.

to be about 30 μm by the thickness of the silicon wafer and the depth of the micro-trench (Inset of Figure 6.37 (c)). The portion of the pore connecting to the bottom of the micro-trench is the region of interest for the experiment. Once again, the magnetic disk trap array is patterned afterwards, this time with careful alignment (EVG 620 Aligner) to connect each micro-pore to an adjacent magnetic disk. Top view (Fig. 6.37 (b)) and side view (Fig. 6.37 (c)) SEM images show the high density micro-pore array chip.

In contrast to the low density micro-pore array chip, this chip has ~40,000 through micro-pores per 1 cm^2 and is patterned such that each micro-pore is adjacent to one magnetic disk. The alignment of pores with magetic traps is easily visualized in bright field while the locations of pores may be determined by looking at transmitted light through the pores, as shown in Figure 6.39. The high throughput nature of this chip closely aligns with transfection requirements that are suitable for clinical use.

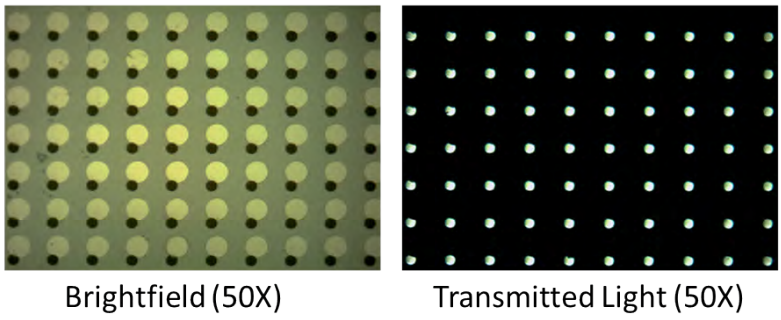

Figure 6.39: High-density micropore array chip. Brightfield images show pore-disk alignment while transmitted light images show locations of pores that go through the entire thickness of the wafer.

6.2.4 Experimental procedure and results

Materials

Four types of cells were used in the 3D MEP transfection experiments. Primary human white blood cells were purified from whole blood from the American Red Cross (Columbus, OH). KG1a (an acute myeloid leukemia cell line), K562 (human immortalised myelogenous leukemia) and Jurkat (human T lymphocyte cell lines) were obtained from American Type Culture Collection (ATCC). These three cell lines were cultured in RPMI 1640 (catalog No. 11875-093), with the addition of 10% (v/v) fetus bovine serum (FBS, heat-inactivated, cat. no. 26010).

Propidium Iodide (PI, cat. no. P3566, Invitrogen, excitation/emitting wavelength,

535/617 nm) was used for low throughput delivery experiments as well as for viability assessments on the high density delivery experiments, with staining applied ∼75 minutes after electroporation for transfection reagents other than PI. Fluorescein amidite (FAM)-labeled oligodeoxynucleotides (FAM-ODN, Alpha DNA company, cat. no. 427520, excitation/emitting wavelength, 492/517 nm) and GATA2 molecular beacon (GATA2 MB, 50 μM/ml, Sigma-Aldrich, excitation/emitting wavelength, 495/515 nm) were also delivered into cells to evaluate transfection efficiency. An inverted microscope (Nikon Elipse Ti) was used to check the fluorescent expression after electroporation. The nuclei of cells were stained with Hoechst (Sigma-Aldrich, cat. no. 654434, excitation/emitting wavelength, 350/461 nm) to indicate cell locations on the chip. The micro-pore array was visualized by phase contrast.

All four types of cells used for this study were labelled with anti-CD45 magnetic beads (see Chapter 2); various kits are also commercially available to label different cell types.

Low density micro-pore electroporation

For single cell techniques in the low density micro-pore array, a specific cell may be aligned on a pore using a pre-programmed disk manipulation routine. In Figure 6.40 (a), magnetic fields are first used to guide a magnetically labeled white blood cell directly onto the pore, demonstrating the complete control over cell manipulation and localization provided by this device. PI dye is delivered into the cell by low voltage electroporation (10V, 10 ms, 5 pulses) in just over 1 minute (Figure 6.40 (b)). (Micro-channel transfection has been shown to deliver molecules, even those larger than PI dye, more quickly to the cell than bulk electroporation, depending on the size of the pores, cell type, and molecule transfected [18]). After transfection, the cell is rapidly removed from the pore via protocols associated with the magnetic tweezers (Figure 6.40 (c)) [25]. This is a critical attribute of the device, as it allows for downstream analysis in lab-on-a-chip devices. This single-cell experiment demonstrates the robust capability of the magnetic tweezers to not only align cells on the pores, but also to manipulate them to or from any location on the array before and after transfection.

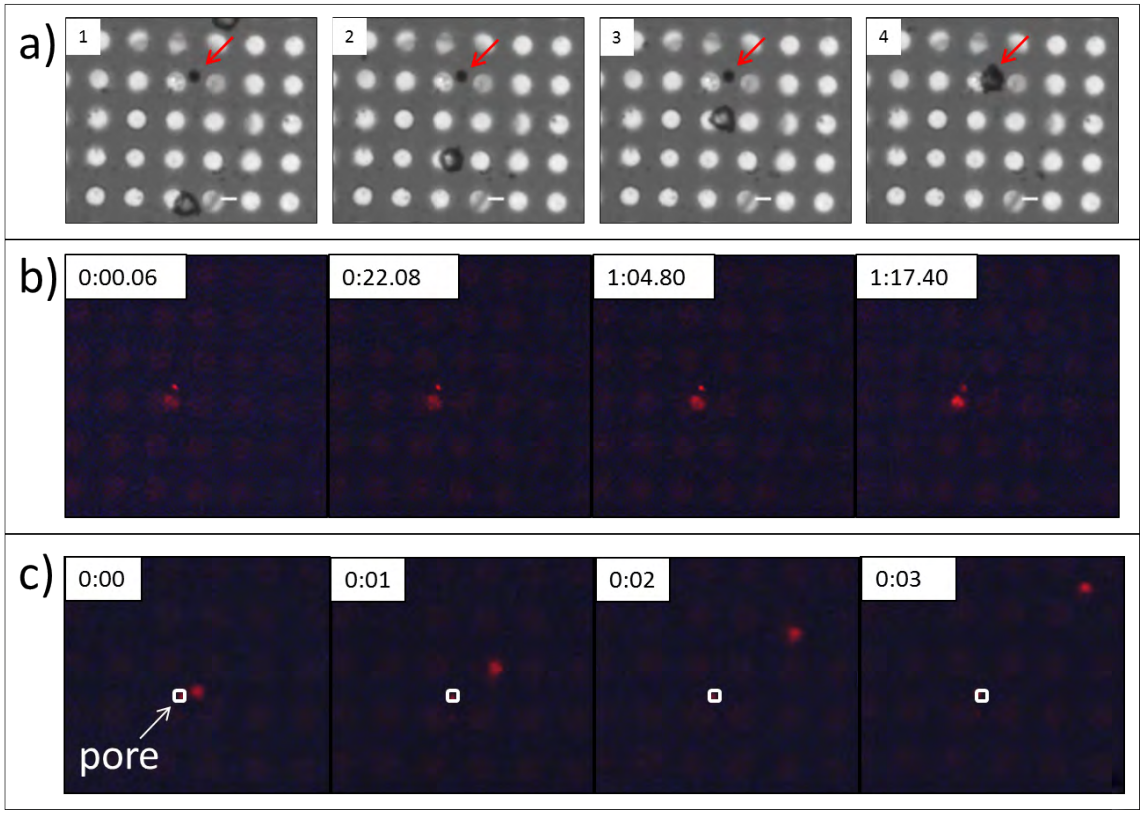

Figure 6.40: On-chip single cell manipulation by magnetic tweezers. (a) Programmed routines are utilized to manipulate a single magnetically labeled white blood cell toward a micro-pore (indicated by red arrow) and localize it on the pore (frame 4). (b) 10 V pulses are delivered, resulting in rapid PI dye uptake. (c) Post-transfection, the cell is rapidly removed from the pore (indicated by white square). Time units for (b) and (c) are minutes:seconds.

High density micro-pore array

To perform a high-throughput 3D MEP transfection experiment, alignment is done as described previously (Figure 6.35 (d-f)). After cells are aligned, 1-10 brief (10 ms) pulses are delivered to transfect all cells simultaneously.

6.2.5 Results

Alignment

The alignment of cells over pores for 3D MEP is critical. To demonstrate this, a control experiment was run using the high density 3D MEP chip without magnetic fields for a random seeding control experiment (Figure 6.41). Here the first panel shows pore location

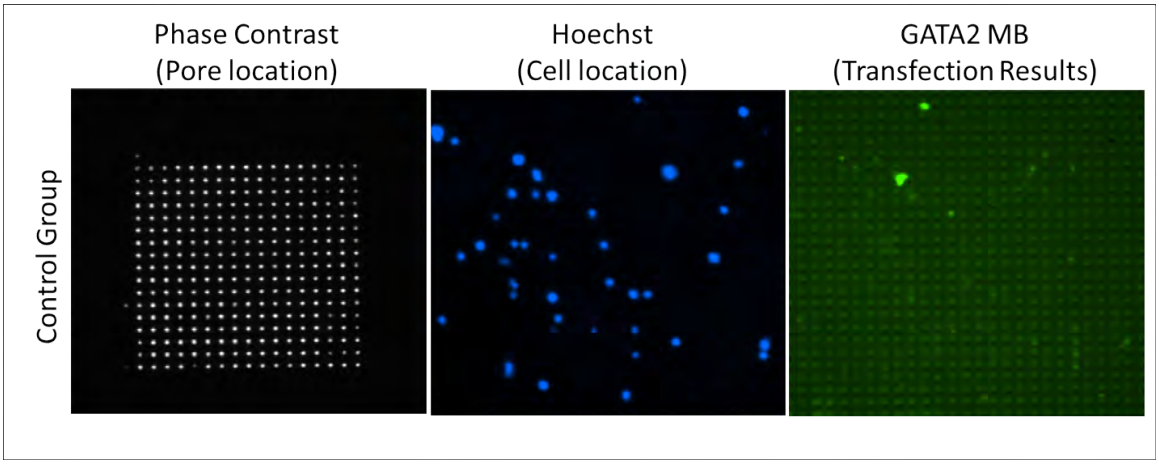

Figure 6.41: K562 transfection with GATA2 MB with random seeding (no magnetic tweezer trapping). Phase contrast (pore locations), Hoechst nuclear staining (cell locations), and GATA2 MB fluorescence expressed 75 min after electroporation (indicates transfection efficiency).

based on transmitted light and the second shows cell location from Hoechst nuclear staining. The third panel, showing FAM fluorescent imaging after ODN-FAM delivery under identical conditions to those used with the magnetic tweezers alignment (4 V, 50 ms pulse, 10 pulses). The third panel demonstrates the poor transfection efficiency resulting directly from poor alignment.

Magnetic tweezers-based alignment, on the other hand, as described previously in Figure 6.35 (d-f), is completely automated with the high-density micro-pore array. It is also rapid, taking only a few minutes, as shown in the sequential frames of Figure 6.42 (a), in which frames were taken starting several seconds after initial cell seeding (t = 0, in which 3 cells have already been aligned). Most of the cells are aligned (34 cells, circled in red) and only 2 misaligned (circled in dashed yellow) after 2 minutes and 23 seconds. Figure 6.42 (b) illustrates the cell array pattern resulting from the high throughput alignment. Pore location is determined by transmitted light in the first panel, and cell nuclei are stained with Hoechst for visualizing cell location in the second. These images are merged in the third panel to show alignment over the entire 17×17 pore array.

Quantification of the alignment efficiency (Figure 6.42 (c)) shows magnetic tweezer assisted cell alignment efficiency (in which an aligned cell completely covers a single pore),

as compared to random seeding (without magnetic fields). When cells randomly precipiate down to the chip, the chance of alignment to the micro-pores is low (∼25%) and the cells are then not localized firmly in position. With the magnetic tweezers, the alignment efficiencies are 87% for K562 cells, 88% for Jurkat cells, and 85% for KG1a cells. These numbers are dramatically larger than that of the random seeding and have a direct impact on the subsequent transfection. A transfection efficiency of 83.4% (Figure 6.42(d)) was achieved using magnetic tweezers for alignment and transfection of K562 cells with GATA2 MB. This is significantly higher than the ∼4.9% transfection efficiency of the randomly seeded control group. This result verifies findings from the transmembrane potential simulation, and underscores the importance of the magnetic tweezers in increasing the efficiency of cellular poration by aligning cells to the micro-pores.

For statistical analysis, two-sided student T-test was used to determine the significance for data with Gaussian distribution and equal variances. Groups with p values < 0.05 were considered statistically significant.

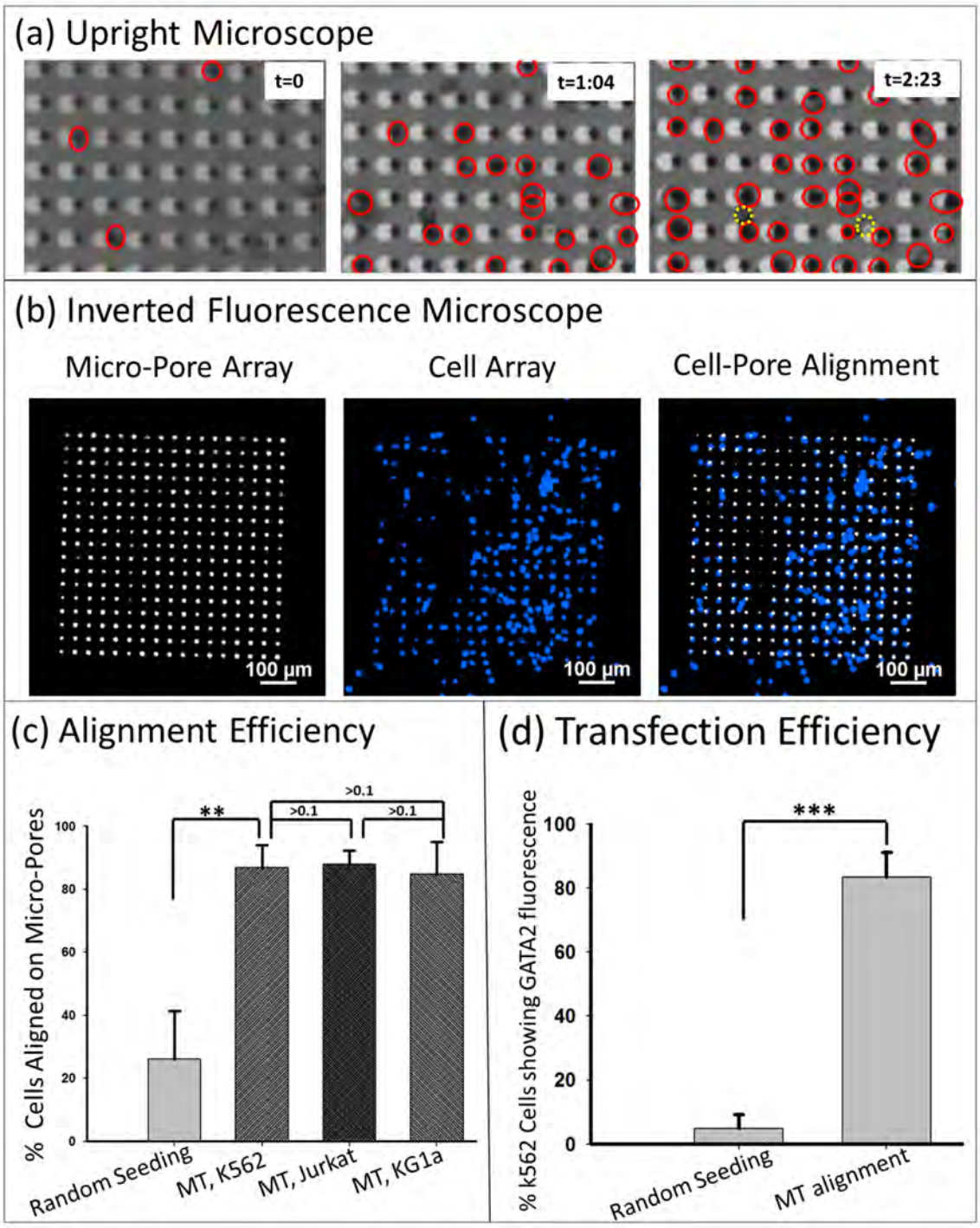

Figure 6.42: Magnetic tweezer-based alignment. (a) Sequential frames during cell seeding show alignment of cell array on pores (aligned cells circled in red, misaligned in dashed yellow) with magnetic tweezer assistance. (b) Resulting cell alignment on a 17 x 17 array of pores, shown with phase contrast (indicates location of through pores), Hoechst staining (indicates cell locations), and a merged image demonstrating cell-pore alignment. (c) Alignment efficiencies of K562, Jurkat and KG1a cells to the micro-pore by magnetic tweezers, compared to K562 random seeding (cell number n=300). (d) Efficiency of K562 transfection with GATA2 MB after magnetic tweezer assisted cell trapping, compared with random seeding (n= 500). ***: $p < 0.005$; **: $p < 0.01$.

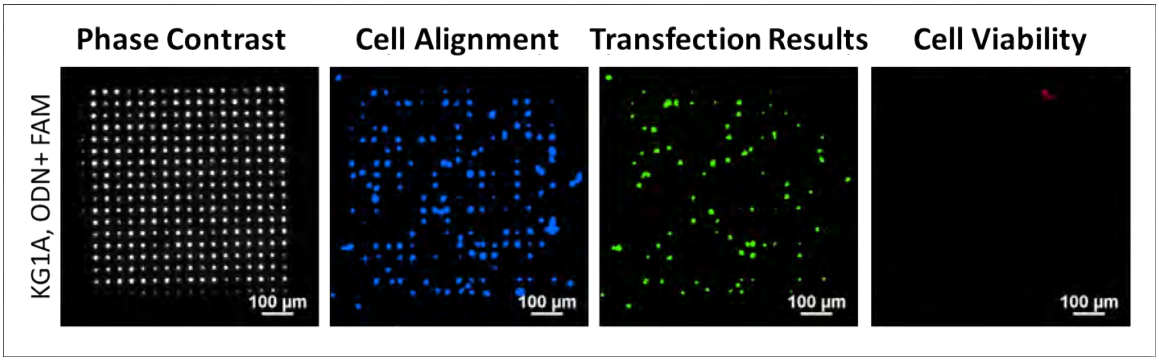

Figure 6.43: High throughput cell transfection on 3D MEP. Phase contrast (showing locations of pores), Hoechst staining (showing cell location by staining cell nuclei), green fluorescence (showing fluorescence of ODN or GATA2 MB), and PI staining (showing cell mortality/ viability) are shown for ODN + FAM delivery into KG1a cells.

High throughput ODN+FAM Delivery

The high throughput nature of the high density micropore array was first demonstrated by injecting oligodeoxynucleotide (ODN) with attached FAM dye into KG1a cells, as shown in Figure 6.43. Efficient alignment of the cell array onto the pores is confirmed with phase contrast imaging and Hoechst staining. The cells were transfected with low voltage (4 V), and the green fluorescence reported from FAM was visualized in most cells after the voltage pulse was delivered, indicating the intracellular delivery. These preliminary experiments demonstrate the high throughput functionality of the chip for DNA molecule delivery.

High throughput GATA2 molecular beacon delivery

The versatility of the magnetic tweezers-based 3D MEP approach is demonstrated through delivery of the intracellular probe, GATA2 molecular beacon (MB) for detection of the regulation level of GATA2 mRNA. Transcription factors of the GATA family play important roles in the proliferation and differentiation of pluripotent hematopoietic stem cells (HSCs) [109]. Among them is the GATA2 which is highly expressed in HSCs and progenitors to regulate hematopoitic development. Its disorder has been hypothesized to be one cause of leukemia [110, 111]. Detection of GATA2 is thus of great significance for the study of heterogeneities of HSCs. As a transcription factor, however, few accessible technologies to date can achieve intracellular detection for GATA2 within living cells. In this experiment,

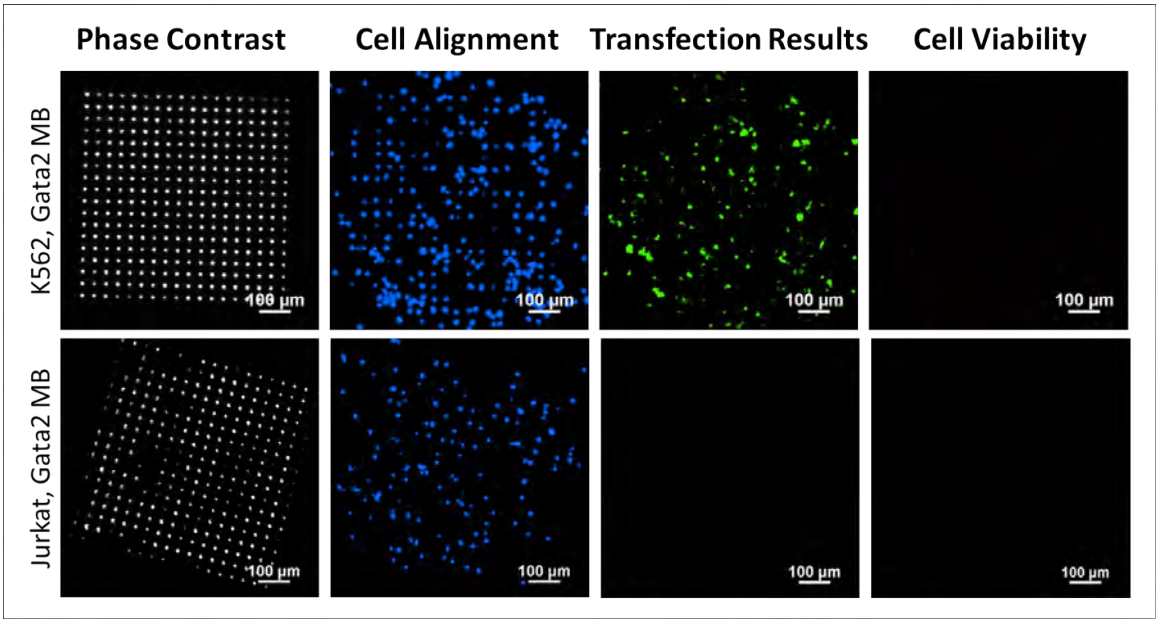

Figure 6.44: GATA2 MB delivery. Phase contrast (showing locations of pores), Hoechst staining (showing cell location by staining cell nuclei), green fluorescence (showing fluorescence of ODN or GATA2 MB), and PI staining (showing cell mortality/ viability) are shown for GATA2 MB delivery and fluorescence in K562 cells (GATA2 positive) and Jurkat cells (GATA2 negative). (See Figure 6.46 for quantification.)

a GATA2 molecular beacon was delivered into both K562 cells and Jurkat cells to detect the GATA2 gene. K562 is a human immortalised myelogenous leukemia cell line, a common myloid progenitor with high GATA2 expression. Jurkat is a T lymphocyte mature leukemic cell line with low level of GATA2 mRNA. The transfected GATA2-MB specifically hybridizes to GATA2 mRNA in the cytosol, increasing its fluorescence by unzipping the hairpin stucture, thereby distinguishing cells with a high GATA2 level from those with low GATA2 levels. The present study thus provides a platform to test the performance of the GATA2 MB on identifying intracellular GATA2 mRNA within a high throughput, statistically meaningful framework. The magnetic tweezers based 3D MEP system, in combination with molecular beacon probes, offers a novel fluorescence bio-sensing system for detection of intracellular markers within living cells.

The successful delivery of GATA2 MB into K562 and Jurkat cells is shown Figure 6.44, with phase contrast and Hoesch staining panels to demonstrate pore location and cell location, respectively.

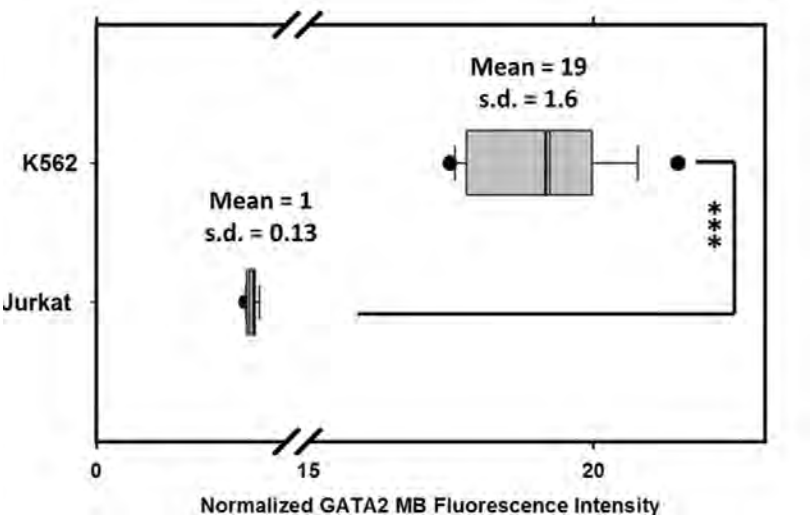

Figure 6.45: A normalized comparison of fluorescent intensity for GATA2 MB in K562 cells and Jurkat cells. (n=400, and the average fluorescence intensity of Jurkat is normalized to 1). ***: $p < 0.005$

The green fluorescence panels of Figure 6.44 show a remarkable expression of green fluorescence 1 hour after GATA2 MB delivery into the K562 cells, indicating the up-regulation of the GATA2 gene. In contrast, negative expression of the GATA2 MB fluorescence 1 hour after delivery into the Jurkat cells is also evident. Comparison of the relative normalized fluorescence intensity between K562 and Jurkat cells (Figure 6.45) shows that the GATA2 MB fluorescence from K562 is ∼19 times higher than that from Jurkat (p-value < 0.005). Relatively uniform amounts of MB are delivered into cells with the device, as evidenced by the small variation in fluorescence intensity (s.d. $= 1.6$). The fluorescence intensity from Jurkat cells is weak but uniform (s.d. $= 0.13$), forming a sharp contrast to the positive signals from K562. These results confirm that on-chip discrimination of GATA2 positive cells from negative cells at the single-cell level is possible through this approach. Importantly, it presents a method to detect mRNA using intracellular probes in a cytolysis-free manner.

Cell Viability

For each high-throughput cell transfection experiment, the cell viability was evaluated approximately 75 minutes after electroporation with propidium iodide (PI) dye. These experiments were performed in collaboration with Mr. Lingqian Chang. In solution, PI uptake will not occur in a cell with an intact membrane (excluding deliberate electroporation-based transfection, as described previously on the low density micro-pore array), but will rapidly enter a damaged cell membrane, intercalate into cellular nucleic acids and fluoresce brightly

in the red.

The images (4th panels of Figures 6.43 and 6.44) show no obvious PI fluorescence, thus confirming viable post-transfection cells with intact membranes. Quantitative results in Figure 6.46 (a) confirm viability of 92% for K562 cells, 89% for Jurkat cells, and 96% for KG1a cells. These experimental results show that magnetic labeling and low voltage pulses do not damage the cell membranes.

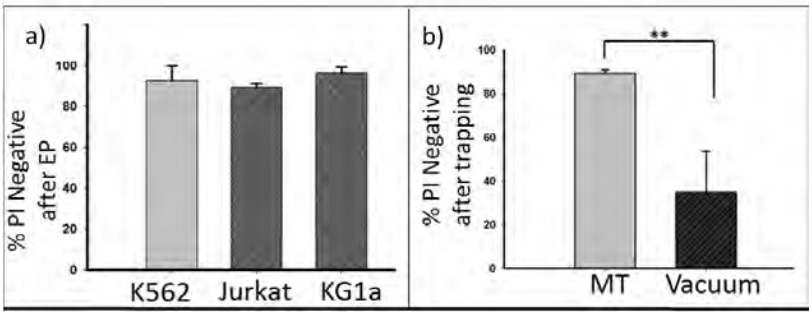

Figure 6.46: Cell viability. (a) Quantitative analysis of PI negative fluorescence, showing cell viability, is shown for K562 (92% viable), Jurkat (89% viable), and KG1a (96% viable) cells. Performed 75 min after electroporation. (n=1000) (b) A comparison of PI negative fluorescence, showing cell viability, for Jurkat cells aligned by magnetic tweezers (90% viable) and Jurkat cells aligned by vacuum (6∼8 Psi, 34% viable). Performed after trapping. n=600, **: $p < 0.01$

Experiments were also carried out using a conventional vacuum approach for trapping cells on the same 3D MEP chip in order to compare alignment efficiency and cell viability associated with this mode of localization. The instrument generating the vacuum is a filter bottle with a porous cork and a nozzle linked to a vacuum pump. The 3D MEP chip was placed on the porous cork while the vacuum pressure was adjusted by a control valve read out by a pressure gauge. For cell trapping, a droplet of cell buffer with a defined cell number was placed on the chip. Vacuum pressure drives the cells to the micro-pores, with many cells (∼15 μm diameter) eventually being trapped on micro-pores (5 μm diameter). It was difficult to optimize the vacuum pressure, as demonstrated in Figure 6.47. A high trapping efficiency (8 psi) was not possible without damaging the cell membrane. In the figure, phase contrast images for each case show the location of the micro-pore array, Hoechst nuclear staining illustrates cell locations on the array, and PI dye staining, applied 10 minutes after vacuum trapping, shows cell damage incurred due to vacuum generated force. If this force was too weak, e.g. for 4 psi - 6 psi, the hydrodynamics were insufficient to draw cells down to the micro-pore regions. Natural precipitation of cells eventually results in a random distribution without a clear array pattern. When the vacuum was increased from 6 psi to 8 psi, however, 90% of the cells were damaged. While adjusting the vacuum to the 6 $\sim$ 8 psi

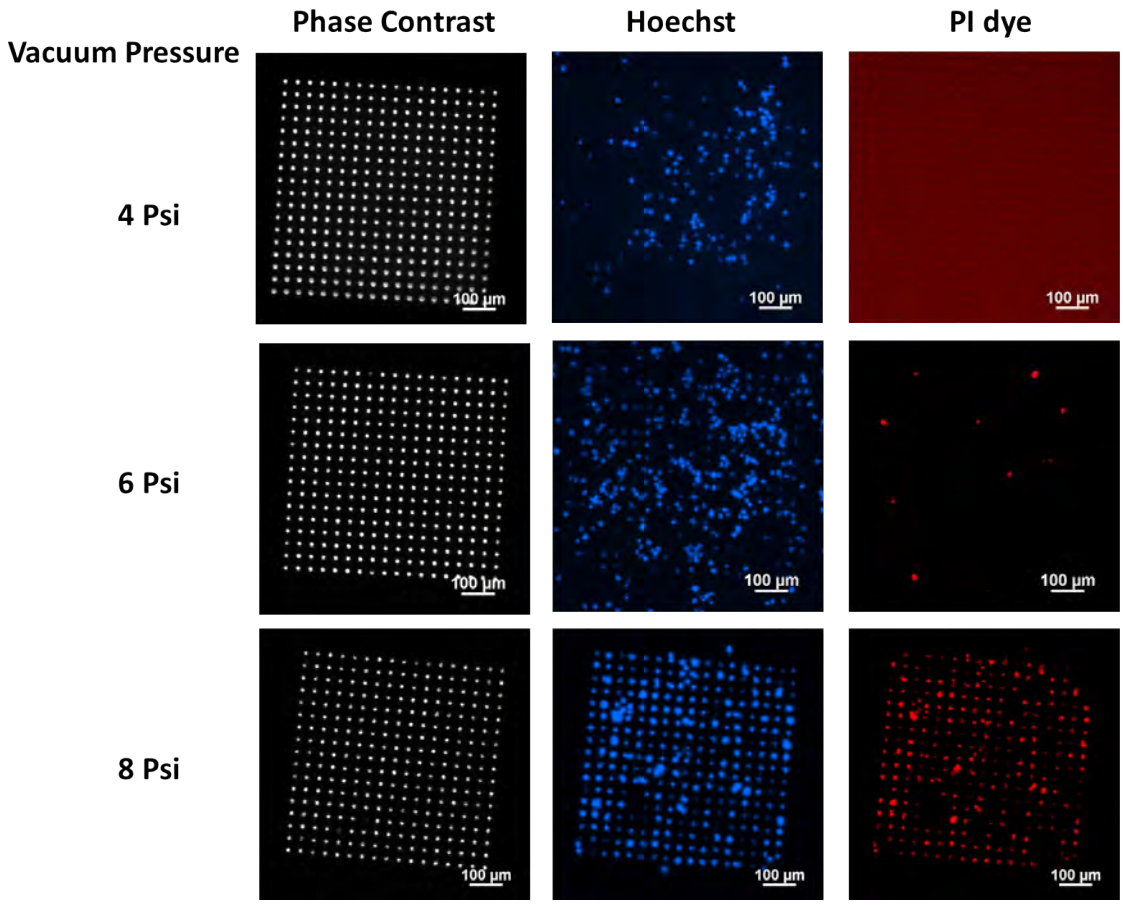

Figure 6.47: Trapping Jurkat cells on the MPA chip using vacuum with varying negative pressure. Phase contrast shows the location of the micro-pore array. Hoechst staining of the cell nuclei identifies the location of cells after vacuum application. Cells were stained with PI dye 10 min after trapping to show the cell damages induced by the different vacuum generated forces.

range yielded a 90% alignment efficiency in several attempts, the associated cell viability (Figure 6.46 (b)) clearly illustrates the magnetic tweezers to be far more effective in keeping cell membranes intact (∼90%) compared to the vacuum approach under the same trapping results (∼34% cell viability).

The difference between magnetic tweezers and vacuum-based cell trapping mechanisms illustrates one of the advantages of the magnetic tweezer platform. Since the effective range of the magnetic tweezer traps is short, the cells experience the trap force only after they gently precipitate down to the immediate vicinity of the micro-pore. In contrast, the vacuum generated forces are long-ranged and drive cells to flow with finite speeds until they

are abruptly brought to rest by the chip. The resulting momentum change upon reaching the edge of the micro-pore usually causes cell deformation and/or membrane rupture. In fact this method has been previously used to rupture cell membranes for gene delivery [108].

6.2.6 Conclusion and future work on 3D MEP

Magnetic tweezer-based 3D MEP is a safe, effective, and high-throughput cell transfection technique that offers the features necessary for statistically significant clinical studies. Furthermore, MEP offers the potential for versatile lab-on-chip systems that integrate cell-manipulation and real-time detection followed by cell transfer, thereby paving the road for comprehensive analysis of cellular behaviors in response to environment, signal pathways, cell-cell interactions and cellular dynamics in the post-transfection stage.

Current work is ongoing with the device, particularly with the goal of developing a 3D nanochannel electroporation device. This device ("3D NEP") would be nearly identical to the high-density micro-pore array 3D MEP device but with sub-micron diameter (∼400 - 900 nm) pores. The advantage of 3D NEP over 3D MEP is that the cellular delivery dosage of transfection reagent would be more controlled, as will be described in more detail in the following nanochannel electroporation section. This will lead to more advanced and more precise drug delivery and gene therapy capabilities. Furthermore, the smaller pores would enhance the tight focusing of electric fields, leading to less field leakage due to pore alignment and the ability to transfect much larger molecules (e.g. long strands of DNA).

One anticipated challenge of 3D NEP is difficulty in fabrication: aligning magnetic disks with sub-micron sized pores, due to optical microscope limitations. However, magnetic traps are critical in this 3D NEP technique because, in addition to the aforementioned benefits of magnetic tweezers over other methods of localization, vacuum generated forces are not sufficient to trap cells onto nano-pores (not shown).

6.3 Nano-channel electroporation

6.3.1 Introduction

As its name suggests, nanochannel electroporation (NEP) utilizes channels that are nanoscale in diameter for transfection; in the studies presented here, pores range from about 90 to 500 nm diameter. The technique was developed in 2011 [18] and advances both bulk electroporation and microchannel electroporation by allowing for dosage-controlled transfection, which, while possible in microinjection, is largely unattainable with any current high-throughput techniques. The technique presented is a two-dimensional technique (2D NEP).

Originally, this technique was developed as an optical tweezers-based device [18]. Although optical tweezers allow for very precise positioning of a single cell against a nanochannel, a major drawback is the low-throughput nature of the technique. To transfect more than one cell at once, each cell must be individually manipulated and localized one at a time against the nanochannel, and this time-intensive technique is not feasible in a clinical setting. Therefore, a multiplexed method for cell localization against the nanochannels is required to enable this technique to be high throughput. As with the microchannel electroporation discussed in the previous section, magnetic tweezers offer the multiplexing abilities required for advancing the device to a high throughput technique.

6.3.2 Materials and Methods

The devices for 2D NEP consist of quartz chips patterned with micro-magnetic traps bonded to PDMS with molded micro- and nano-channels. This device sits within the electromagnetic setup required for magnetic tweezer manipulation (see Chapter 2). Electrodes are made of electrochemically inert materials such as gold or platinum. A power supply capable of delivering a square wave pulse of high (100-300 V) voltage is used to deliver the pulse (Gene Pulser Xcell^{TM}, Bio-Rad [36]). The transfection reagent must be taken into consideration to determine the position of the electrodes. For example, PI dye is positively charged while DNA carries a negative charge.

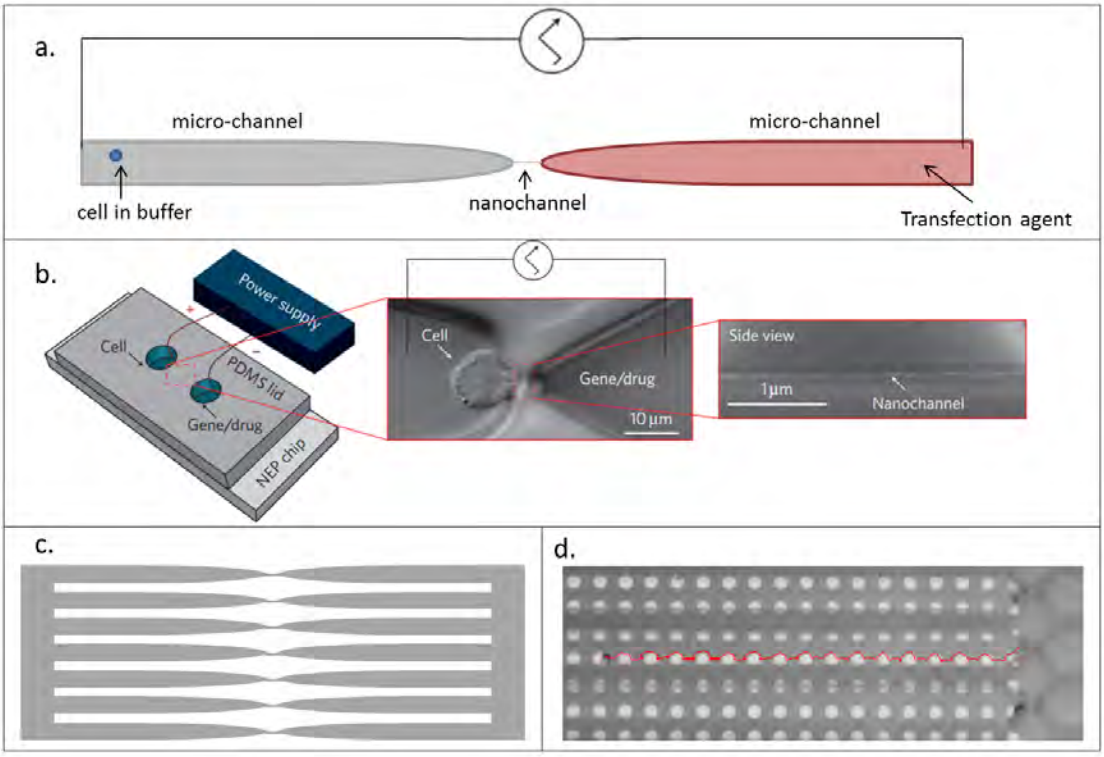

Figure 6.48: The basic construct of 2D NEP. The device consists of (a) two micro-channels connected by a nano-channel. One of these micro-channels contains the cell while the other contains the transfection reagent. A voltage pulse is delivered across this construct for transfection. (b) Schematic shows that the cells and transfection reagent are loaded into the device and the electrodes connect the channels via reservoirs cut into the PDMS. A Jurkat cell is shown adjacent to the nano-channel (manipulated with optical tweezers). Image from Boukany et al, *Nature Nanotechnology*, 2011. (c) Schematic of multiplexed device, in which large reservoirs connect microchannels, allowing simultaneous transfection across all microchannels. (d) Micro-magnetic disk traps imprinted beneath the microchannels allow cells to be manipulated to the nanochannels. One cell's movement is tracked in red in the image; cells in the two adjacent microchannels have already been localized at the nano-channels.

First generation 2D NEP device

Various device designs were utilized for 2D NEP. The first, developed by Boukany et al [18] for optical tweezers-based electroporation, is based on the microchannel-nanochannel-microchannel construct shown in Figure 6.48 (a). The channels are molded onto a PDMS device, which is bonded onto a quartz wafer. A cell and transfection reagent are introduced into the micro-channel (∼40 μm diameter) on the left and right, respectively. The micro-channels are connected by a nano-channel (∼90-400 nm diameter, 5-10 μm long), shown in Figure 6.48 (b). To multiplex, each 2D NEP device can contain hundreds of microchannel-nanochannel-microchannel constructs (Figure 6.48 (c)). This allows a single

pulse (or multiple pulses) to be delivered simultaneously across all microchannels.

In the magnetic tweezer-based method presented here, an array of magnetic disks is patterned on the quartz NEP chip and manually aligned with the magnetic traps under one side of the PDMS device, with a disk aligned at each nanochannel for cell localization during the experiment. The PDMS is bonded to the quartz wafer with the permanent bonding (oxygen plasma method) described in Chapter 2. The chip is then treated with PEG silane to reduce cell adhesion. Magnetically labeled cells are placed into the cell-side reservoir and magnetic traps are used to transport them to the nanochannels (Figure 6.48 (d)) through remotely activated protocols. Post transfection, the cells may be removed from the device with the same protocols via the same reservoir. This provides a simple means of moving all cells simultaneously into and out of the device.

Second Generation 2D NEP Device

Although capable of transfecting nearly 100 cells in one experiment, one drawback of the first generation 2D NEP device is that transfected cells are not sorted from those that have not been transfected. They are removed from the microchannels using the same pathway through which they entered, thus mixing un-transfected cells with transfected cells. To overcome this, a new design was developed (two versions shown in Figure 6.49 (a-c)). This device consists of a single microchannel on the cell side, with an input and output reservoir at either end; the dye side is similar to the original design.

In the second generation design, all cells start at one end of the device (labeled "Input Reservoir," Fig. 6.49 (d)), are manipulated along the microchannel by the traps, aligned with nanochannels (Fig. 6.49 (e)) and localized for transfection. Post transfection they are manipulated out of the device in the same direction as they were moved in (toward "Output Reservoir"). With all output cells being transfected, this technique offers the ability to easily study cells that were transfected separately from those that were not. In current studies, sorting is often a very desireable feature in lab-on-chip experiments [112, 113], whether it is the singular purpose of the device or just one aspect of a multistep process. This sorting technology offers a simple combination of two steps (transfection + sorting) into one.

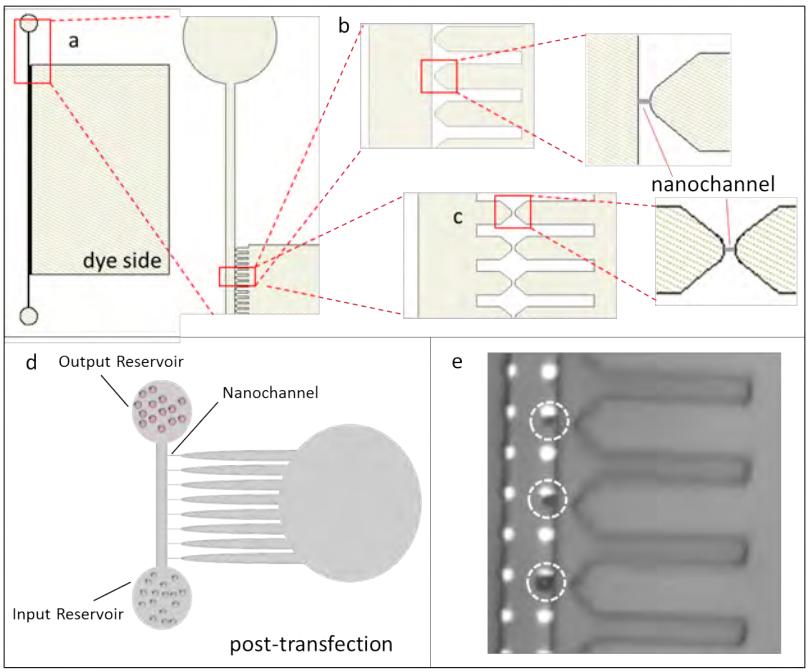

Figure 6.49: Second generation 2D NEP devices. (a-c) Two devices are shown, with the entire device (a) as well as zoomed-in schematics (b and c). (d) Schematic shows the sorting capabilities of this device. The transfection reagent is placed in the reservoir on the right, cells are placed in the input reservoir. Post-transfection, only transfected cells are manipulated to the output reservoir. (e) Micrograph of three magnetic beads of various sizes (circled in dashed white) aligned by magnetic traps with the nanochannels in second generation device described by schematic (b).

In all devices, PDMS is bonded to the quartz surface using the protocol described in Chapter 2. Before use, all devices are treated with PEG-silane to reduce cell adhesion to the surface. They are also sterilized with UV light (UV-ozone) prior to long-term cell experiments. The use of non-conductive substrate (quartz) electrically isolates the two sides. It is important that the disks are not located underneath the nanochannels because the uneven surface (disks ~60-70 nm above the surface) results in poor bonding near the nanochannels, often leading to leakage of transfection reagent and poor electrical isolation of the two sides.

6.3.3 Results

First generation 2D NEP device results

Preliminary studies integrating the magnetic traps with the 2D NEP device were performed with the first generation device, which had approximately 98 microchannels on each side. Cells labeled with magnetic microbeads were placed in the reservoir and manipulated toward the nanochannels with the magnetic traps as shown in Figure 6.48 (d).

Some challenges presented with this device are that air bubbles, debris, or clumps of cells can cause blockage at the inlet of a microchannel. This results in some channels not

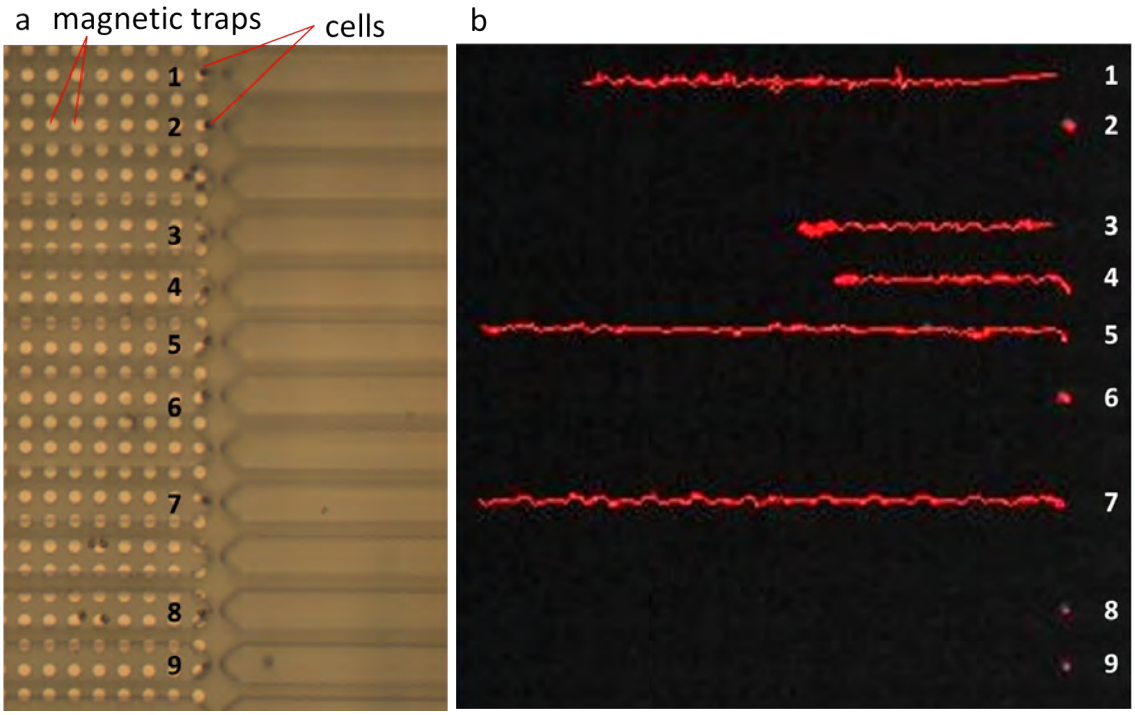

Figure 6.50: Transfection with 2D NEP. (a) Brightfield microscopy image shows 9 cells aligned with the nanochannels. Three of the microchannels also have more than one cell in the channel, further from the nanochannel. These will not be affected by the voltage pulse and thus will not be transfected. (b) After the pulse, all nine of the cells are transfected, shown in a single frame of a video under fluorescence. The red traces for cells 1,3,4,5, and 7 show traces of the motion of the cells out of the microchannels after transfection. Cells 2,6,8, and 9 were transfected but had adhered to the surface of the chip and the magnetic traps were unable to remove them.

containing cells. Furthermore, in channels with no clogging, it is possible that too many cells could enter the channel. It is thus critical to wash cells to remove unlabeled cells and to mix cells well prior to placing them in the reservoir to reduce cell-cell adhesion. Furthermore, cell concentration should be adjusted depending on the number of microchannels in the device. For these experiments in the 98-microchannel devices, channels were first filled with ~50-100 μL buffer followed by addition of ~1-10 μL of cells in buffer (at a concentration of 10^6 cells/mL).

Figure 6.50 (a) shows an image taken after cell localization in a section of the 2D NEP device prior to transfection. The cells are human white blood cells, purified from whole blood from the American Red Cross (Columbus, OH), labeled with 1 μm diameter anti-CD45 magnetic microbeads (Stemcell Technologies CD45 depletion kit, cat. no. 18259 and

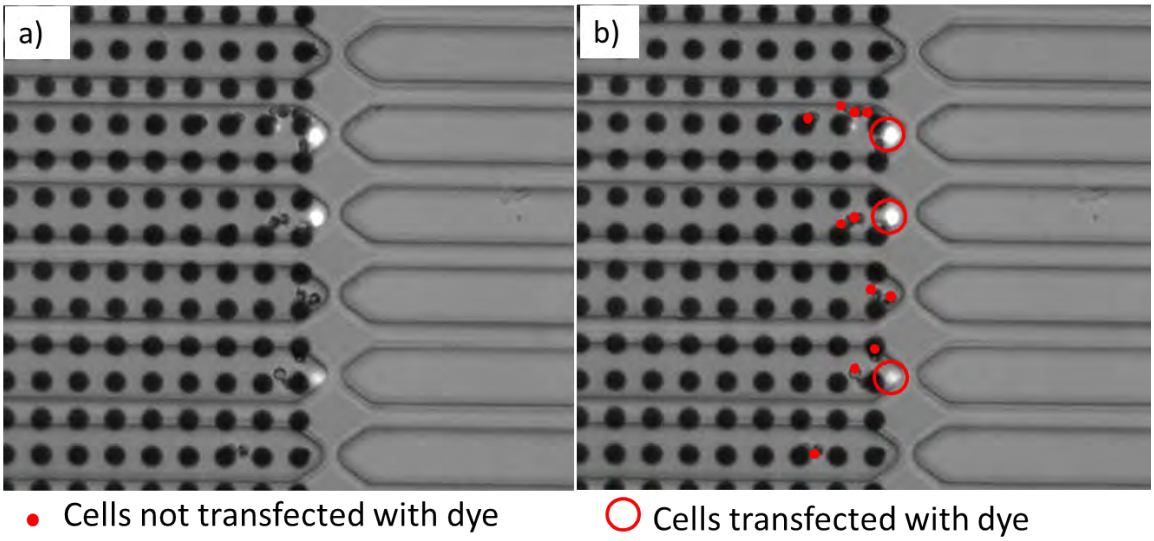

Figure 6.51: Precise nanochannel transfection. (a) A micrograph taken on an inverted microscope after transfection shows micro-channels with several white blood cells in each. However, only the cell located directly against the nano-channel was transfected, as labeled in (b). Magnetic disks (black) are 15 μm in diameter.

D particles, cat. no. 19250). A section of the 98-channel device is shown, in which 9 cells are aligned next to the nano-channels. Using the 10^6 cells/mL concentration, it is shown that although three micro-channels contain more than one cell, most of the channels contain only one cell and that cell is aligned well with the nano-channel.

The transfection reagent for this experiment was propidium iodide (PI, cat. no. P3566, Invitrogen, excitation/emitting wavelength, 535/617 nm) dye. A single voltage pulse (240 V, 20 ms) was delivered and Figure 6.50 (b) shows the transfection results. A video of pulse delivery and subsequent manipulation of cells out of the device indicated that all 9 cells aligned with the nanochannels in the frame were transfected. Cells identified 1, 3, 4, 5, and 7 were then remotely manipulated out of the device with the magnetic traps; the red traces of Fig. 6.50 (b) track the paths of each. Cells 2, 6, 8, and 9 were not removed from the device as they seemed to have adhered to the surface and the magnetic traps were unable to overcome the adhesion forces.

Following the experiment, the entire 98 channels of the device were viewed. Approximately 30 cells were fluorescing (i.e. transfected). (Note, however, that this scan was taken

after cells were manipulated out of the device and therefore only includes the cells that had remained in the channels due to adhesion to the surface.)

For nano-channel electroporation, it is critical that the cell is pressed directly against the nanopore to promote safe, controlled transfection [18]. This allows for the pore to directly control the maximum size of nano-pores formed on the cell membrane, as well as the affected area of the membrane. It also prevents leakage of transfection reagent into the surrounding solution, thus contributing to proper dosage control.

Figure 6.51(a) shows a merged image (bright field + fluorescence) demonstrating that only the cells that were directly pressed against the nanochannels were transfected. These are circled in red for clarity in the same image in Fig. 6.51 (b), whereas cells that were not transfected are identified by red dots.

Second generation 2D NEP device results

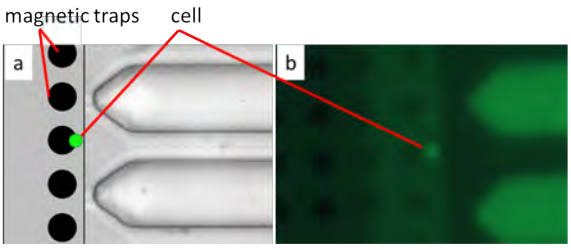

Figure 6.52: ODN-FAM transfection. A schematic (a) and fluorescent image (b) are shown of a single cell that was transfected with ODN+FAM in the second generation 2D NEP device. Post transfection, the cell was moved away from the nanochannel and is seen here localized on a magnetic trap some distance away from the nanochannel used for transfection.

Experimental work is ongoing with the second generation device. As shown previously in Figure 6.49 (e), alignment of various sizes of cells is possible even without focused microchannels. Preliminary studies show that transfection through the nanochannels in this design is possible. Figure 6.52 shows a single human white blood cell that was transfected with ODN+FAM. In this experiment, the cell was localized adjacent to a nanochannel, transfected (3 pulses, 200 V and 10 ms each), and then manipulated out of the channel. The post-transfection image (Fig. 6.52 (b)) and corresponding schematic (Fig. 6.52 (a)) show a snapshot of the transfected cell at a random location in the channel, localized by a magnetic trap.

Challenges introduced with this new design relate to hydrodynamics within the single microchannel on the cell side. Because there is a reservoir at either end filled with fluid, additional hydrodynamic forces are introduced which can either assist in cell loading or

oppose it. Assistance with cell loading occurs when a gentle fluid flow in the direction of loading causes the cells to enter the channel and flow through until they are picked up by magnetic traps. However, even when these forces assist with cell loading, they often fluctuate, likely due to slight changes in pressure from one reservoir or the other. This is a common challenge with microfluidic devices [2, 114] and can be controlled more carefully by using a syringe pump capable of very low flow rates (i.e. nl/min - nl/hr).

6.3.4 A theoretical model

Modeling the effects of a voltage pulse on a cell membrane in the nanochannel electroporation device can be done with an equivalent circuit (Figure 6.53) [39, 100, 115, 116]. The model shown here was originally presented in Boukany et al [18]. The cell membrane is divided into two sections, M_1 (the portion directly adjacent to the nanochannel) and M_2 (the rest of the membrane). Each section of the membrane is modeled as a capacitor in parallel with a resistor. In the model of 2D nanochannel electroporation, the microchannels filled with PBS act as current-carrying wires due to relatively low resistance (< 1 MΩ), as estimated using

$$R = G^{-1} = \frac{l}{\sigma \cdot A}$$

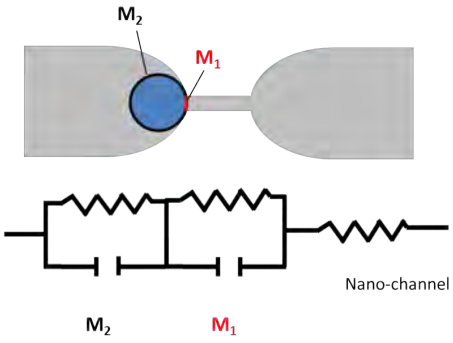

Figure 6.53: Equivalent circuit for a single cell against a nanochannel for the first generation 2D NEP device. The nanochannel is represented by a resistor. The cell membrane is divided into M_1 (adjacent to nanochannel) and M_2, each represented by a resistor in series with a capacitor.

where R, G, l, and A are the resistance, conductance, length and area of the channel, respectively, and σ is the conductivity of the solution in the channel (PBS), $\sigma \sim 1.5$ S/m [18]. A nanochannel, which has a very small cross-sectional area, will act as a resistor (∼100-500 MΩ, depending on the diameter). Approximate values for this model, including equivalent resistances and capacitances of M_1 and M_2, are listed in Table 6.1.

Capacitances are calculated based on membrane

capacitance $C_m = 1.0 \times 10^{-2} \frac{F}{m^2}$ [117] and cell diameter 5 μm (corresponding to the purified white blood cells used for 2D NEP). Resistances are calculated based on membrane resistace $R_m = 1 \times 10^4\ \Omega cm^2$.

Upon application of the voltage pulse, M_1 will quickly charge and porate upon reaching the membrane threshold voltage. Once M_1 has porated, the current will travel through the cytosol ($\sigma \sim 0.2$ - 0.5 S/m [18, 118]), essentially shorting the resistor at M_1 in the model. A short time afterwards, M_2 will then charge, reach threshold voltage, and porate as well.

Estimated Values, Nanochannel Electroporation	
Channel length	5 µm
Channel diameter	200 nm
Equivalent capacitance C_1	0.0003 pF
Equivalent resistance R_1	3 x 10^7 MΩ
Equivalent capacitance C_2	0.8 pF
Equivalent resistance R_2	1 x 10^4 MΩ
Nanochannel resistance R_{NC}	106 MΩ

Table 6.1: Estimated values associated with the equivalent circuit theoretical model of nanochannel electroporation for experiments discussed in this chapter.

The small length and cross-sectional area of the nanochannel will limit additional diffusion during and after the pulse, which allows for successful dosage control in NEP.

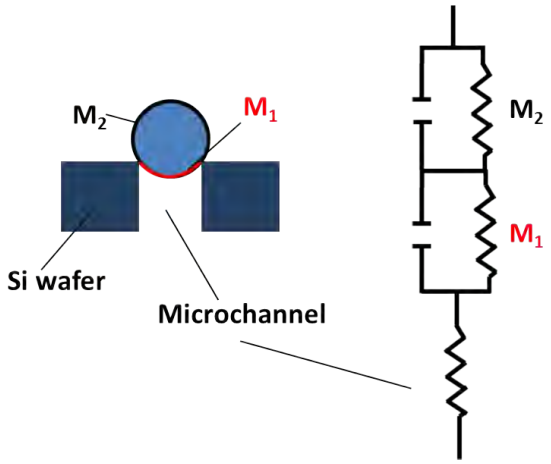

Figure 6.54: Equivalent circuit for a single cell against a microchannel for 3D MEP. The microchannel represents a resistor (∼6 MΩ) and the section of cell membrane adjacent to the microchannel (M_1) and the rest of the cell membrane (M_2) are each represented by a resistor in parallel with a capacitor.

The circuit model used to describe nanochannel electroporation can be utilized to explain some of the inherent differences between nanochannel and microchannel electroporation. Figure 6.54 describes the same circuit, now applied to microchannel electroporation (see also Table 6.2). Here, the area of membrane adjacent to the channel (M_1) is much larger than in the case of the nanochannel. The larger area of the microchannel will result in a significantly lower resistance (∼1 MΩ) and thus only a slight reduction in voltage from the applied voltage. This is why much lower voltages (1-10 V) must be used to preserve cell viability.

Once M_1 has porated, the transfection reagent is free to diffuse through the microchannel

and into the cell until the pores once again close, which could take several seconds or even minutes.

Diffusion was much more limited in the NEP design due to the smaller diameter of the nanochannel. Experimentally, the amount of time it took to visualize the dye in the cells after transfection (on the order of minutes compared to the nearly instantaneous visualization of dye in cells during NEP) confirmed this diffusion-based transfection.

Estimated Values, Microchannel Electroporation	
Channel length	30 µm
Channel diameter	5 µm
Equivalent capacitance C_1	0.2 pF
Equivalent resistance R_1	5 x 10^4 MΩ
Equivalent capacitance C_2	0.6 pF
Equivalent resistance R_2	1.7 x 10^4 MΩ
Microchannel resistance R_{MC}	1 MΩ

Table 6.2: Estimated values associated with the equivalent circuit theoretical model of microchannel electroporation for experiments discussed in this chapter. Note that these values estimate a cell diameter of 5 μm for comparison with NEP estimates. In reality, slightly larger cells are generally used for the 5 μm pore size.

It has been noted in some studies that perhaps more complex models are required to fully explain the system of cell electroporation for both microchannel [119] and nanochannel [115] electroporation. Nonetheless, these models offer both a qualitative description of the MEP/NEP process and a method of determining voltages applied to the membrane based on the experimental design parameters.

6.4 Conclusion

Applications of 2D NEP and 3D MEP, which range from transformation of bacteria for gene amplification to detection of a family of mRNA in cancer cells, are broad and varied [42]. The robust devices described in this chapter have the ability to transfect many different types of charged molecules into various prokaryotic and eukaryotic cells, including cells that do not lend themselves easily to other types of injection. We have demonstrated automated cell loading for both single cell and high throughput applications, rapid and simple transfection, and the possibility for integration into complex lab-on-chip devices. The weak magnetic fields and low voltages applied to the cells do very little to no damage to the cells, thus leaving them viable after the experiment, which is not the case with many current high throughput technologies.

Chapter 7
Conclusion

The previous chapters of this thesis have demonstrated the advancement of thin film-based micromagnetic traps, which have provided an effective manipulation platform for both cells and DNA. Critical attributes of this platform that are particularly useful in biomedical applications have enabled multiplexed manipulation and localization, an experimentally verified understanding of the applied forces, and a demonstration of the ease of integration into lab-on-a-chip devices.

Multiplexed manipulation and localization

While many techniques are capable of manipulating and/or localizing a single or a few molecules, a current critical need of clinical relevance is methods that carry out each of these operations in parallel on tens of thousands of biological entities. Performing such experiments on large populations of cells is also required for statistically significant results. Scale-up of conventional techniques is challenging; for instance traditional magnetic tweezers are generally limited to unidirectional forces applied normal to the platform on a few cells or molecules. Vacuum-generated forces, on the other hand, while able to multiplex the function of localization (see Chapter 6), are not capable of manipulation. In contrast the magnetic tweezers platform described in this thesis provides precise localization and manipulation capable of multiplexed maneuvers on biomolecules (Chapter 4) as well as on cells (Chapter 6).

As described in Chapter 6, the magnetic tweezers are capable of simultaneously exerting identical forces on tens of thousands of cells, enabling their parallel manipulation and

localization. Currently, such a 1 cm × 1 cm magnetic tweezers based electroporation chip can transfect 40,000 cells simultaneously. Clearly, by simply increasing the size of the chip (e.g. a 2 cm x 2 cm chip), it is possible to drastically scale up the number of cells that are concurrently transfected. Alternatively, by slightly changing the design on the same size chip, the number of cells transfected could be increased. For example, 14 μm diameter disks with 20 μm center-to-center spacing would render the chip capable of transfecting ~60,000 cells/cm^2. Instead of changing the sizing of the disks, a second array of appropriately placed pores could also be added such that two cells are aligned on each disk, with one on either side [25]. This design would increase the number of transfected cells to ~80,000 cells/cm^2.

Understanding of forces applied

In addition to multiplexing, it is critical for the forces exerted onto biological entities to be well characterized. This is important for validating measurements (e.g. DNA elasticity) and for preserving the viability of cells. As our magnetic tweezers platforms continue to be implemented into more complex biotechnologies, experimental justification of mathematical models of the applied forces become important. The experiments in Chapters 4 and 5 have shown that the generated forces lie in the pico-Newton regime, a range characteristic of typical intracellular forces, thereby rendering the mobile magnetic traps capable of influencing responses without damaging the targeted objects.

Ease of integration into lab-on-a-chip devices

Cells and biomolecules must be magnetically labeled through a simple procedure prior to their use on the magnetic tweezers platforms. The benefit of this step is that the unit may be easily integrated with other lab-on-chip components that also take advantage of magnetic signatures. In Chapter 6, labeling prior to electroporation technologies allowed the traps to not only localize cells for transfection but also to subsequently manipulate them out of the device following transfection. The magnetic labeling and presence of magnetic traps throughout a complex lab-on-chip device thus enables simple, user-controlled, multiplexed manipulation of entities from one process to the next. Moreover, because these tasks are

controlled by pre-programmed routines, limited user input is required for operation of the device.

Future work

It has been demonstrated that micromagnetic tweezers, which can be seamlessly integrated into various microfluidic devices to serve as a foundation for cell and molecule manipulation in complex technologies, is now capable of probing intracellular components. These developments open up much potential for future work. Any microscopic magnetic material or biological entity labeled with magnetic microbeads (e.g. cells or DNA) may be manipulated and analyzed on this platform. This could, for example, lead to fluorescent imaging of biomolecule stretching or supercoiling, observed in real-time on one horizontal plane. With the added functionality of manipulating magnetic beads away from the conduit of the zigzag wire, as discussed in Chapter 5, different precise stretch lengths can be realized. Furthermore, the various methods of tethering DNA to beads and surfaces allow for different models to be used to stretch molecules. Surface tethering in this device would also be further improved by patterning locations for DNA attachment on the surface [8].

The ability of this system to access not only the exterior but also the interior of cells through integration with electroporation techniques opens up possibilities to transfect different types of cells with genes, drugs or molecular beacons, as demonstrated in Chapter 6. The 2D NEP and 3D MEP systems improve upon major drawbacks of other transfection techniques. The rapid, high-throughput nature of 3D MEP makes it a candidate for experiments in which studies of large populations of cells yield statistically significant results, such as clinical studies on gene therapies for cancer [84]. On the other hand, 2D nanochannel electroporation, which is not as high-throughput as 3D MEP but capable of delivering controlled dosages into cells, is useful for studies requiring more careful control either for the safety of the cell or for dosage-related studies [18]. Furthermore, implementation of 3D microelectroporation with smaller nanochannels could lead to dosage-controlled 3D NEP in the future. Since cells may be manipulated by micromagnetic traps before and after transfection, this device could be combined with downstream magnet-based analyses.

Finally, these devices are capable of transfecting nearly any cell (at least 5 μm diameter for 3D MEP and any size for 2D NEP). In the field of microbiology, bacteria transformed with plasmids are used as nanofactories to amplify DNA and create proteins; bacteria with magnetic traits or capable of being magnetically labeled could therefore be integrated into this device.

The remote operation of the device, implemented in Chapter 6 for automated alignment of cells on the high-density micropore array for 3D microelectroporation, demonstrates the ease of use of the device. Future work in voice control and preprogrammed routines could further enhance ease of use for electroporation and in other multiplexed biomedical devices.

References

[1] Deniz, A. A., Mukhopadhyay, S., and Lemke, E. A. "Single-molecule biophysics: at the interface of biology, physics and chemistry". *Journal of the Royal Society Interface* **5**, 15–45 (2008). Cited on page 1.

[2] Yun, H., Kim, K., and Lee, W. G. "Cell manipulation in microfluidics". *Biofabrication* **5**, 022001 (2013). Cited on pages 1, 5, 6, and 79.

[3] Tan, S. J., Li, Q., and Lim, C. T. "Manipulation and isolation of single cells and nuclei". *Methods in Cell Biology* **98**, 79–96 (2010). Cited on pages 1 and 6.

[4] Hochmuth, R. M. "Micropipette aspiration of living cells". *Journal of Biomechanics* **33**, 15–22 (2000). Cited on pages 1 and 6.

[5] Ramser, K. and Hanstorp, D. "Optical manipulation for single-cell studies". *J. Biophoton.* **3**, 187–206 (2010). Cited on pages 1 and 7.

[6] Zhang, H. and Liu, K.-K. "Optical tweezers for single cells". *Journal of the Royal Society Interface* **5**, 671–690 (2008). Cited on pages 1, 2, and 6.

[7] Wuite, G. J. L., Davenport, R. J., Rappaport, A., and Bustamante, C. "An integrated laser trap/flow control video microscope for the study of single biomolecules". *Biophysical Journal* **79**, 1155–1167 (2000). Cited on pages 1 and 6.

[8] Vlaminck, I. D., Henighan, T., van Loenhout, M. T. J., Burnham, D. R., and Dekker, C. "Magnetic forces and dna mechanics in multiplexed magnetic tweezers". *PLOS ONE* **7** (2012). Cited on pages 1, 7, 28, 30, 35, and 84.

[9] Vlaminck, I. D. and Dekker, C. "Recent advances in magnetic tweezers". *Annu. Rev. Biophys.* **41**, 453–472 (2012). Cited on pages 1 and 7.

[10] Crick, F. H. C. and Hughes, A. F. W. "The physical properties of cytoplasm: A study by means of the magnetic particle method. part i. experimental". *Experimental Cell Research* **1**, 37–80 (1950). Cited on page 1.

[11] Zlatanova, J. and Leuba, S. H. "Magnetic tweezers: a sensitive tool to study dna and chromatin at the single-molecule level". *Biochemistry and Cell Biology* **81**, 151–159 (2003). Cited on page 1.

[12] Crick, F. H. C. "The physical properties of cytoplasm: A study by means of the magnetic particle method. part ii. theoretical treatment". *Experimental Cell Research* **1**, 37–80 (1950). Cited on page 1.

[13] Kollmannsberger, P., Mierke, C. T., and Fabry, B. "Nonlinear viscoelasticity of adherent cells is controlled by cytoskeletal tension". *Soft Matter* **7**, 3127–3132 (2011). Cited on pages 1, 7, and 8.

[14] Chen, A., Byvank, T., Chang, W.-J., Bharde, A., Vieira, G., Miller, B. L., Chalmers, J. J., Bashir, R., and Sooryakumar, R. "On-chip magnetic separation and encapsulation of cells in droplets". *Lab on a Chip* **13**, 1172–1181 (2013). Cited on page 1.

[15] Riethdorf, S., Fritsche, H., Müller, V., Rau, T., Schindlbeck, C., Rack, B., Janni, W., Coith, C., Beck, K., Jänicke, F., Jackson, S., Gornet, T., Cristofanilli, M., and Pantel, K. "Detection of circulating tumor cells in peripheral blood of patients with metastatic breast cancer: a validation study of the cellsearch system". *Clinical Cancer Research* **13**, 920–928 (2007). Cited on page 1.

[16] Nagrath, S., Sequist, L. V., Maheswaran, S., Bell, D. W., Irimia, D., Ulkus, L., Smith, M. R., Kwak, E. L., Digumarthy, S., Muzikansky, A., Ryan, P., Balis, U. J., Tompkins, R. G., Haber, D. A., and Toner, M. "Isolation of rare circulating tumour cells in cancer

patients by microchip techology". *Nature Letters* **450**, 1235–1239 (2007). Cited on page 1.

[17] Choi, S., Karp, J. M., and Karnik, R. "Cell sorting by deterministic cell rolling". *Lab on a Chip* **12**, 1427–1430 (2012). Cited on page 1.

[18] Boukany, P. E., Morss, A., Liao, W.-C., Henslee, B., Jung, H., Zhang, X., Yu, B., Wang, X., Wu, Y., Li, L., Gao, K., Hu, X., Zhao, X., Hemminger, O., Lu, W., Lafyatis, G. P., and Lee, L. J. "Nanochannel electroporation delivers precise amounts of biomolecules into living cells". *Nature Nanotechnology* **6**, 747–754 (2011). Cited on pages 1, 3, 13, 53, 54, 61, 72, 73, 78, 79, 80, and 84.

[19] Zhan, Y., Wang, J., Bao, N., and Lu, C. "Electroporation of cells in microfluidic droplets". *Anal. Chem.* **81**, 2027–2031 (2009). Cited on pages 1 and 54.

[20] W.H. Wang, X.Y. Liu, Y. "High-throughput automated injection of individual biological cells". *IEEE Transactions on Automation Science and Engineering* **6**, 209–219 (2009). Cited on pages 1, 51, and 52.

[21] Ashok, P. C. and Dholakia, K. "Optical trapping for analytical biotechnology". *Current Opinion in Biotechnology* **23**, 16–21 (2012). Cited on page 1.

[22] Dochow, S., Krafft, C., Neugebauer, U., Bocklitz, T., Henkel, T., Mayer, G., Albert, J., and Popp, J. "Tumour cell identification by means of raman spectroscopy in combination with optical traps and microfluidic environments". *Lab on a Chip* **11**, 1484–1490 (2011). Cited on page 1.

[23] Chan, J. W. "Recent advances in laser tweezers raman spectropscopy (ltrs) for label-free analysis of single cells". *J. Biophotonics* **6**, 36–48 (2013). Cited on page 1.

[24] Vieira, G., Henighan, T., Chen, A., Hauser, A. J., Yang, F. Y., Chalmers, J. J., and Sooryakumar, R. "Magnetic wire traps and programmable manipulation of biological cells". *Physical Review Letters* **103**, 128101 (2009). Cited on pages 1, 2, 8, 10, and 48.

[25] Henighan, T., Chen, A., Vieira, G., Hauser, A. J., Yang, F. Y., Chalmers, J. J., and Sooryakumar, R. "Manipulation of magnetically labeled and unlabeled cells with mobile magnetic traps". *Biophysical Journal* **98**, 412–417 (2010). Cited on pages 1, 2, 8, 61, and 83.

[26] Chen, A., Byvank, T., Vieira, G. B., and Sooryakumar, R. "Magnetic microstructures for control of brownian motion and microparticle transport". *IEEE Transactions on Magnetics* **49**, 300–308 (2013). Cited on page 1.

[27] Clarke, R. W., White, S. S., Zhou, D., Ying, L., and Klenerman, D. "Trapping of proteins under physiological conditions in a nanopipette". *Agnew. Chem. Int. Ed.* **44**, 3747–3750 (2005). Cited on pages 2 and 6.

[28] Ying, L., White, S. S., Bruckbauer, A., Meadows, L., Korchev, Y. E., and Klenerman, D. "Frequency and voltage dependence of the dielectrophoretic trapping of short lengths of dna and dctp in a nanopipette". *Biophysical Journal* **86**, 1018–1027 (2004). Cited on pages 2 and 6.

[29] Zheng, X. T. and Li, C. M. "Single cell analysis at the nanoscale". *Chem. Soc. Rev.* **41**, 2061–2071 (2012). Cited on page 2.

[30] Weihs, D., Mason, T. G., and Teitell, M. A. "Bio-microrheology: A fronteir in microrheology". *Biophysical Journal* **91**, 4296–4305 (2006). Cited on page 3.

[31] Gal, N. and Weihs, D. "Intracellular mechanics and activity of breast cancer cells correlate with metastatic potential". *Cell Biochem Biophys* **63**, 199–209 (2012). Cited on page 3.

[32] Na, Y.-R., Kim, S. Y., Gaublomme, J. T., SHalek, A. K., Jorgolli, M., Park, H., and Yang, E. G. "Probing enzymatic activity inside living cells using a nanowire-cell "sandwich" assay". *Nano Letters* **13** (2013). Cited on page 3.

[33] Tyagi, S. and Kramer, F. R. "Molecular beacons: probes that fluoresce upon hybridization". *Nature Biotechnology* **14**, 303–308 (1996). Cited on page 3.

[34] Huang, K. and Martií, A. A. "Recent trends in molecular beacon design and applications". *Anal Bioanal Chem* **402**, 3091–3102 (2012). Cited on page 3.

[35] Fang, X., Mi, Y., Li, J. J., Beck, T., Schuster, S., and Tan, W. Molecular beacons: Fluorogenic probes for living cell study, (2002). Cited on page 3.

[36] http://www.bio-rad.com/en-us/category/electroporation, (2014). Bio-Rad Laboratories, Inc. Cited on pages 3, 52, and 72.

[37] Escoffre, J.-M., Portet, T., Wasungu, L., Teissie, J., Dean, D., and Rols, M.-P. "What is (still not) known of the mechanism by which electroporation mediates gene transfer and expression in cells and tissues". *Mol Biotechnol* **41**, 286–295 (2009). Cited on pages 3, 51, and 53.

[38] Valero, A., Post, J. N., van Nieuwkasteele, J. W., ter Braak, P. M., Kruijer, W., and van den Berg, A. "Gene transfer and protein dynamics in stem cells using single cell electroporation in a microfluidic device". *Lab on a Chip* **8**, 62–67 (2008). Cited on pages 3 and 54.

[39] Khine, M., Lau, A., Ionescu-Zanetti, C., Seo, J., and Lee, L. P. "A single cell electroporation chip". *Lab on a Chip* **5**, 38–43 (2005). Cited on pages 3, 54, and 79.

[40] Huang, Y. and Rubinsky, B. "Micro-electroporation: Improving the efficiency and understanding of electrical permeabilization of cells". *Biomedical Microdevices* **2**, 145–150 (1999). Cited on pages 3, 51, and 54.

[41] Wang, S. and Lee, L. J. "Micro-/nanofluidics based cell electroporation". *Biomicrofluidics* **7**, 011301 (2013). Cited on pages 3, 53, 54, and 55.

[42] Chang, L., Howdyshell, M., Liao, W.-C., Chiang, C.-L., Gallego-Perez, D., Yang, Z., Lu, W., Byrd, J. C., Muthusamy, N., Lee, L. J., and Sooryakumar, R. Magnetic tweezers-based 3d microchannel electroporation for high-throughput gene transfection. To be submitted. Cited on pages 4 and 81.

[43] Dickson, M. N., Tsinberg, P., Tang, Z., Bischoff, F. Z., Wilson, T., and Leonard, E. F. "Efficient capture of circulating tumor cells with a novel immunocytochemical microfluidic device". *Biomicrofluidics* **5**, 034119 (2011). Cited on page 5.

[44] Wang, G., Mao, W., Byler, R., Patel, K., Henegar, C., Alexeev, A., and Sulchek, T. "Stiffness dependent separation of cells in a microfluidic device". *PLOS One* **8**, 1–10 (2013). Cited on page 5.

[45] Bhagat, A. A. S., Hou, H. W., Li, L. D., Lim, C. T., and Han, J. "Pinched flow coupled shear-modulated inertial microfluidics for high-throughput rare blood cell separation". *Lab on a Chip* **11**, 1870–1878 (2011). Cited on page 5.

[46] Rahimizadeh, J., Meng, F., Sachs, F., Wang, J., Verma, D., and Hua, S. Z. "Real-time observation of flow-induced cytoskeletal stress in living cells". **301** (2011). Cited on page 5.

[47] Ashkin, A., Dziedzic, J. M., Bjorkholm, J. E., and Chu, S. "Observation of a single-beam gradient force optical trap for dielectric particles". *Optics Letters* **11**, 288–290 (1986). Cited on page 7.

[48] Vieira, G., Chen, A., Henighan, T., Lucy, J., Yang, F., and Sooryakumar, R. "Transport of magnetic microparticles via tunable stationary magnetic traps in patterned wires". *Phys. Rev. B* **85**, 174440 (2012). Cited on pages 8, 24, and 37.

[49] Rapoport, E. and Beach, G. S. D. "Magneto-mechanical resonance of a single superparamagnetic microbead trapped by a magnetic domain wall". *Journal of Applied Physics* **111**, 073B10 (2012). Cited on page 8.

[50] Rapoport, E., Montana, D., and Beach, G. S. D. "Integrated capture, transport, and magneto-mechanical resonant sensing of superparamagnetic microbeads using magnetic domain walls". *Lab on a Chip* **12**, 4433–4440 (2012). Cited on page 8.

[51] Rapoport, E. and Beach, G. S. D. "Dynamics of superparamagnetic microbead trans-

port along magnetic nanotracks by magnetic domain walls". *Applied Physics Letters* **100**, 082401 (2012). Cited on page 8.

[52] Donolato, M., Gobbi, M., Vavassori, P., Leone, M., Cantoni, M., Metlushko, V., Ilic, B., Zhang, M., Wang, S. X., and Bertacco, R. "Nanosized corners for trapping and detecting magnetic nanoparticles". *Nanotechnology* **20**, 385501 (2009). Cited on page 8.

[53] Donolato, M., Vavassori, P., Gobbi, M., Deryabina, M., Metlushko, M. H. V., Ilic, B., Cantoni, M., Petti, D., Brivio, S., and Bertacco, R. "On-chip manipulation of protein-coated magnetic beads via domain-wall conduits". *Advanced Materials* **22**, 2706–2710 (2010). Cited on page 8.

[54] Donolato, M., Torti, A., Kostesha, N., Deryabina, M., Sogne, E., Vavassori, P., Hansen, M. F., and Bertacco, R. "Magnetic domain wall conduits for single cell applications". *Lab on a Chip* **11**, 2976–2983 (2011). Cited on page 8.

[55] Guan, J., Boukany, P. E., Hemminger, O., Chiou, N.-R., Zha, W., Cavanaugh, M., and Lee, L. J. "Large laterally ordered nanochannel arrays from dna combing and imprinting". *Advanced Materials* **22**, 3997–4001 (2010). Cited on page 13.

[56] www.lifetechnologies.com. Dynabeads, LifeTechnologies. Cited on pages 16 and 37.

[57] Mørup, S., Hansen, M. F., and Frandsen, C. Magnetic nanoparticles. Oxford: Academic Press. Cited on page 16.

[58] Lu, A.-H., Salabas, E. L., and Schüth, F. "Magnetic nanoparticles: Synthesis, protection, functionalization and application". *Agnew. Chem. Int. Ed.* **46**, 1222–1244 (2007). Cited on page 16.

[59] Bentzen, E. L., Tomlinson, I. D., Mason, J., Gresch, P., Warnement, M. R., Wright, D., Sanders-Bush, E., Blakely, R., and Rosenthal, S. J. "Surface modification to reduce nonspecific binding of quantum dots in live cell assays". *Bioconjugate Chem* **16**, 1488–1494 (2005). Cited on page 20.

[60] Pfister, D. and Morbidelli, M. "Process for protein pegylation". *Journal of Controlled Release* **180**, 134–149 (2014). Cited on page 20.

[61] Purcell, E. M. "Life at low reynolds number". *American Journal of Physics* **45** (1977). Cited on page 25.

[62] McNaughton, B. H., Kehbein, K. A., Anker, J. N., and Kopelman, R. "Sudden breakdown in linear response of a rotationally driven magnetic microparticle and application to physical and chemical microsensing". *J. Phys. Chem B* **110**, 18958–18964 (2006). Cited on page 25.

[63] Phillips, R., Kondev, J., and Theriot, J. *Physical Biology of the Cell*. Garland Science, Taylor & Francis Group, LLC, (2009). Cited on pages 25 and 46.

[64] Strick, T., Allemand, J.-F., Croquette, V., and Bensimon, D. "Twisting and stretching single dna molecules". *Progress in Biophysics & Molecular Biology* **74**, 115–140 (2000). Cited on page 26.

[65] Bustamante, C., Bryant, Z., and Smith, S. B. "Ten years of tension: single-molecule dna mechanics". *Nature* **421**, 423–427 (2003). Cited on pages 26, 35, and 46.

[66] Moffitt, J. R., Chemla, Y. R., Izhaky, D., and Bustamante, C. *Proceedings of the National Academy of Sciences* **103**, 9006–9011 (2006). Cited on page 26.

[67] Scholl, Z. N., Li, Q., and Marszalek, P. E. "Single molecule mechanical manipulation for studying biological properties of proteins, dna, and sugars". *WIREs Nanomed Nanobiotechnol* **6**, 211–229 (2014). Cited on pages 26 and 28.

[68] Vilfan, I. D., Lipfert, J., Koster, D. A., Lemay, S. G., and Dekker, N. H. Magnetic tweezers for single-molecule experiments. In *Handbook of single-molecule biophysics*, 371. Springer (2009). Cited on pages 26 and 28.

[69] Smith, S. B., Finzi, L., and Bustamante, C. "Direct mechanical measurements of the elasticity of single dna molecules by using magnetic beads". *Science* **258** (1992). Cited on pages 26, 28, and 35.

[70] Perkins, T. T., Smith, D. E., Larson, R. G., and Chu, S. "Stretching of a single tethered polymer in a uniform flow". *Science* **268** (1995). Cited on pages 26 and 35.

[71] Rickgauer, J. P., Fuller, D. N., and Smith, D. E. "Dna as a metrology standard for length and force measurements with optical tweezers". *Biophysical Journal* **91**, 4253–4257 (2006). Cited on page 26.

[72] Ribeck, N. and Saleh, O. A. "Multiplexed single-molecule measurements with magnetic tweezers". *Review of Scientific Instruments* **79**, 094301 (2008). Cited on page 35.

[73] Castro, C. E., Kilchherr, F., Kim, D.-N., Shiao, E. L., Wauer, T., Wortmann, P., Bathe, M., and Dietz, H. "A primer to scaffolded dna origami". *Nature Methods* **8**, 221–229 (2011). Cited on page 35.

[74] Rothemund, P. W. K. "Folding dna to create nanoscale shapes and patterns". *Nature* **440**, 297–302 (2006). Cited on page 35.

[75] Zhou, L. F., Marras, A. E., Su, H. J., and Castro, C. E. "Dna origami compliant nanostructures with tunable mechanical properties". *ACS Nano* **8**, 27–34 (2014). Cited on page 35.

[76] Fonnum, G., Johansson, C., Molteberg, A., Morup, S., and Aksnes, E. "Characterisation of dynabeads®by magnetization measurements and mossbauer spectroscopy". *Journal of Magnetism and Magnetic Materials* **293**, 41–47 (2005). Cited on page 37.

[77] www.spherotech.com, (2014). Spherotech, Inc. Cited on page 37.

[78] Sinha, B., Anandakumar, S., Oh, S., and Kim, C. "Micro-magnetometry for susceptibility measurement of superparamagnetic single bead". *Sensors and Actuators A: Physical* **182**, 34–40 (2012). Cited on page 37.

[79] Mirowski, E., Moreland, J., and Russek, S. E. "Integrated microfluidic isolation platform for magnetic particle manipulation in biological systems". *Applied Physics Letters* **84**, 1786–1788 (2004). Cited on page 37.

[80] Braun, O. "Simple model of microscopic rolling friction". *Physical Review Letters* **95**, 126104 (2005). Cited on pages 46 and 48.

[81] Svodoba, K. and Block, S. M. "Force and velocity measured for single kinesin molecules". *Cell* **77**, 773–784 (1994). Cited on page 46.

[82] Luo, D. and Saltzman, W. M. "Synthetic dna delivery systems". *Nature Biotechnology* **18**, 33–37 (2000). Cited on page 50.

[83] Yang, N. S. and Sun, W. H. "Gene gun and other non-viral approaches for cancer gene therapy". *Nat. Med.* **1**, 481–483 (1995). Cited on page 50.

[84] Grupp, S. A., Kalos, M., Barrett, D., Aplenc, R., Porter, D. L., Rheingold, S. R., Teachey, D. T., Chew, A., Hauck, B., Wright, J. F., Milone, M. C., Levine, B. L., and June, C. H. "Chimeric antigen receptor-modified t cells for acute lymphoid leukemia". *The New England Journal of Medicine* **368** (2013). Cited on pages 50 and 84.

[85] Davey, M. R., Rech, E. L., and Mulligan, B. J. "Direct dna transfer to plant cells". *Plant Molecular Biology* **13**, 273–285 (1989). Cited on page 50.

[86] Cohen, S. N. "Bacterial plasmids: their extraordinary contribution to molecular genetics". *Gene* **135**, 67–76 (1993). Cited on page 50.

[87] Hershfield, V., Boyer, H. W., Yanofsky, C., Lovett, M. A., and Helinski, D. R. "Plasmid cole1 as a molecular vehicle for cloning and amplification of dna". *Proceedings of the National Academy of Sciences* **71**, 3455–3459 (1974). Cited on page 50.

[88] Singer, S. and Nicolson, G. "The fluid mosaic model of the structure of cell membranes". *Science* **175**, 720–731 (1972). Cited on page 51.

[89] Wolff, J. A. and Lederberg, J. "An early history of gene transfer and therapy". *Human Gene Therapy* **5**, 469–480 (1994). Cited on page 51.

[90] Villemejane, J. and Mir, L. M. "Physical methods of nucleic acid transfer: general

concepts and applications". *British Journal of Pharmacology* **157**, 207–219 (2009). Cited on page 51.

[91] Zhang, Y. and Yu, L.-C. "Single-cell microinjection technology in cell biology". *Bioessays* **30**, 606–610 (2008). Cited on pages 51 and 52.

[92] Chang, D. C. and Reese, T. "Changes in membrane structure induced by electroporation as revealed by rapid-freezing electron microscopy". *Biophys. J.* **58**, 1–12 (1990). Cited on pages 51 and 53.

[93] Fei, Z., Wang, S., Xie, Y., Henslee, B. E., Koh, C. G., and Lee, L. J. "Gene transfection of mammalian cells using membrane sandwich electroporation". *Anal. Chem* **79**, 5719–5722 (2007). Cited on pages 51 and 55.

[94] Fei, Z., Hu, X., Choi, H., Wang, S., Farson, D., and Lee, L. J. "Micronozzle array enhanced sandwich electroporation of embryonic stem cells". *Anal. Chem.* **82**, 353–358 (2010). Cited on pages 51, 53, 54, and 55.

[95] Gao, K., Li, L., Hinkle, K., Wu, Y., Ma, J., Chang, L., Zhao, X., Perez, D. G., Eckardt, S., Mclaughlin, J., Liu, B., Farson, D. F., and Lee, L. J. "Design of a microchannel-nanochannel-microchannel array based nanoelectroporation system for precise gene transfection". *Small* **10**, 1015–1023 (2014). Cited on pages 51 and 54.

[96] Tsong, T. "Electroporation of cell membranes". *Biophys. J* **60**, 297–306 (1991). Cited on pages 51 and 53.

[97] Teissie, J. and Rols, M.-P. "An experimental evaluation of the critical potential difference inducing cell membrane electropermeabilization". *Biophysical Journal* **65**, 409–413 (1993). Cited on page 52.

[98] Brown, R. B. and Audet, J. "Current techniques for single-cell lysis". *Journal of The Royal Society Interface* **5**, S131–S138 (2008). Cited on page 53.

[99] Lu, H., Schmidt, M. A., and Jensen, K. F. "A microfluidic electroporation device for cell lysis". *Lab on a Chip* **5**, 23–29. Cited on page 53.

[100] Huang, Y. and Rubinsky, B. "Microfabricated electroporation chip for single cell membrane permeabilization". *Sensors and Actuators A* **89**, 242–249 (2001). Cited on pages 53, 55, and 79.

[101] MacQueen, L. A., Buschmann, M. D., and Wertheimer, M. R. "Gene delivery by electroporation after dielectrophoretic positioning of cells in a non-uniform electric field". *Bioelectrochemistry* **72**, 141–148 (2008). Cited on page 54.

[102] Khine, M., Ionescu-Zanetti, C., Blatz, A., Wang, L.-P., and Lee, L. P. "Single-cell electroporation arrays with real-time monitoring and feedback control". *Lab on a Chip* **7**, 457–462 (2007). Cited on pages 54 and 55.

[103] Kurosawa, O., Oana, H., Matsuoka, S., Noma, A., Kotera, H., and Washizu, M. "Electroporation through a micro-fabricated orifice and its application to the measurement of cell response to external stimuli". *Measurement Science and Technology* **17**, 3127–3133 (2006). Cited on page 54.

[104] Wang, M., Orwar, O., Olofsson, J., and Weber, S. G. "Single-cell electroporation". *Anal. Bioanal. Chem.* **397**, 3235–3248. Cited on page 54.

[105] Wang, H.-Y. and Lu, C. "Electroporation of mammalian cells in a microfluidic channel with geometric variation". *Analytical Chemistry* **78** (2006). Cited on page 54.

[106] Lindström, S. and Andersson-Svahn, H. "Overview of single-cell analyses: microdevices and applications". *Lab on a Chip* **10**, 3363–3372 (2010). Cited on pages 54 and 55.

[107] Huang, Y. and Rubinsky, B. "Flow-through micro-electroporation chip for high efficiently single-cell genetic manipulation". *Sensors and Actuators A* **104**, 205–212 (2003). Cited on page 55.

[108] Sharei, A., Zoldan, J., Adamo, A., Sim, W. Y., Cho, N., Jackson, E., Mao, S., Schneider, S., Han, M. J., Lytton-Jean, A., Basto, P. A., Jhunjhunwala, S., Lee, J., Heller, D. A., Kang, J. W., Hartoularos, G., Kim, K. S., Anderson, D. G., Langer,

R., and Jensen, K. F. "A vector-free microfluidic platform for intracellular delivery". *P.N.A.S.* **110**, 2082–2087 (2013). Cited on pages 55 and 71.

[109] Nagai, T., Harigae, H., Ishihara, H., Motohashi, H., Minegishi, N., Tsuchiya, S., Hayashi, N., Gu, L., Andres, B., and Engel, J. D. "Transcription factor gata-2 is expressed in erythroid, early myeloid, and cd34+ human leukemia-derived cell lines". *Blood* **84**, 1074–1084 (1994). Cited on page 66.

[110] Ikonomi, P., Rivera, C. E., Riordan, M., Washington, G., Schechter, A. N., and Noguchi, C. T. "Overexpression of gata-2 inhibits erythroid and promotes megakaryocyte differentiation". *Experimental Hematology* **28**, 1423–1431 (2000). Cited on page 66.

[111] Ostergaard, P., Simpson, M. A., Connell, F. C., Steward, C. G., Brice, G., Woollard, W. J., Dafou, D., Kilo, T., Smithson, S., Lunt, P., Murday, V. A., Hodgson, S., Keenan, R., Pilz, D. T., Martinez-Corral, I., Makinen, T., Mortimer, P. S., Jeffery, S., Trembath, R. C., and Mansour, S. "Mutations in gata2 cause primary lymphedema associated with a predisposition to acute myeloid leukemia (emberger syndrome)". *Nature Genetics* **43** (2011). Cited on page 66.

[112] Bhagat, A. A. S., Bow, H., Hou, H. W., Tan, S. J., Han, J., and Lim, C. T. "Microfluidics for cell separation". *Medical and Biological Engineering and Computing* **48**, 999–1014 (2010). Cited on page 74.

[113] Didar, T. F. and Tabrizian, M. "Adhesion based detection, sorting and enrichment of cells in microfluidic lab-on-chip devices". *Lab on a Chip* **10**, 3043–3053 (2010). Cited on page 74.

[114] Kang, Y. J. and Yang, S. "Fluidic low pass filter for hydrodynamic flow stabilization in microfluidic environments". *Lab on a Chip* **12**, 1881–1889 (2012). Cited on page 79.

[115] Smith, K. C., Gowrishankar, T. R., Esser, A. T., Stewart, D. A., and Weaver, J. C.

"The spatially distributed dynamic transmembrane voltage of cells and organelles due to 10-ns pulses: meshed transport networks". *IEEE Transactions on Plasma Science* **34**, 1394–1404 (2006). Cited on pages 79 and 81.

[116] Gowrishankar, T. R. and Weaver, J. C. "An approach to electrical modeling of single and multiple cells". *PNAS* **100**, 3203–3208 (2003). Cited on page 79.

[117] Kotnik, T., Bobanović, F., and Miklavĉiĉ, D. "Sensitivity of transmembrane voltage induced by applied electric fields–a theoretical analysis". *Bioelectrochemistry and Bioenergetics* **43**, 285–291 (1997). Cited on page 80.

[118] Krassowska, W. and Filev, P. D. "Modeling electroporation in a single cell". *Biophysical Journal* **92**, 404–417 (2007). Cited on page 80.

[119] Shagoshtasbi, H. and Lee, Y.-K. A new equivalent circuit model for micro electroporation systems, (2011). Cited on page 81.

Appendix A: Functionalization of surface with Antidigoxigenin

This protocol is used within a flow channel (either compression channels or PDMS channels, see Chapter 2) to coat the surface with antidigoxigenin (Anti-digoxigenin, Fab fragments from sheep, Roche Diagnostics cat. no. 11214667001), for attaching digoxigenin-labeled DNA (see Chapter 5). The first steps (chip processing) should be done prior to placing the chip in the flow channel.

1. Si Chip Processing

   (a) Rinse the sample in ethyl alcohol, then DI water, dry with nitrogen gas to remove particulate matter

   (b) Sonicate in toluene 30 minutes

   (c) Dip in DI water to rinse, dry with nitrogen gas. Keep samples covered at all times on bench to reduce dust and particulate matter

   (d) Potassium hydroxide (KOH, Amresco®) etch in constant temperature (50^oC) water bath. Use a quartz or pyrex beaker for the KOH etch. 30% KOH in water. Etch should be approximately 50 nm per hour (note that the surface being etched here is SiO_2, from the silicafilm, see Chapter 2). Etch for ∼20-60 minutes.

   (e) Place chip in DI water, then rinse in DI water and dry well (in incubator overnight is best).

   (f) Silanize surface after KOH etch: place in a beaker and cover with 60 mL chromasolve acetone. Place on rotator for gentle agitation for 10 minutes. Add 1.2 mL silane drop by drop while rotator is still agitating solution. Allow to mix for 3 minutes. Then place the chip into 50:50 ratio chromasolve acetone to MilliQ (2 minutes) water followed by just MilliQ water (2 minutes). Dry in incubator for 1 hour.

   (g) Now place chip inside microfluidic channel.

2. Microfluidic channel should be well sealed and a syringe pump is used to regulate fluid

flow rate (usually limited to around 1 μL/s with DNA tethered, and as high as 10 μL/s for coating a compression channel). Begin with air flow through channel.

3. Flow $\sim$100 μL DI water slowly through, ensuring that there are no air bubbles
4. Flow in 100 μL of PBS at room temperature, degassed
5. Flow $\sim$100 μL 8% glutaraldehyde (in PBS) through flow cell.
6. Allow the device to incubate at room temperature (15 minutes)
7. Flow $\sim$100 μL distilled water through the cell
8. Flow $\sim$100 μL PBS through channel
9. Flow 100 μL 0.1 mg/ml antidigoxigenin in PBS through channel. Clip ends of tubing and incubate 30 minutes at room temparature.
10. Flow 50-100 μL BSA through channel (10 mg/ml)
11. Incubate for 15 min at room temperature. It is best to use this the same day.
12. For long-term storage, flow 200 μL PBS + NaN_3 and refrigerate until use

Appendix B: Functionalization of carboxyl magnetic microbeads with antidigoxigenin

1. Wash 2.5 μL 5% w/v 1-1.4 m Carboxyl particles (Spherotech cat. no. CP-10-100) in sodium acetate buffer, 0.01 M, pH 5.0
2. Add 0.02 mg 1-Ethyl-3-(3-dimethylaminopropyl)carbodiimide hydrochloride (EDC Thermo Scientific, Product no. 22980) to the pellet and mix (pipette in and out)
3. Incubate at room temperature for 1 hour
4. Vortex and incubate for 2 hrs at room temperature on a rotary mixer
5. Centrifuge at 3000g for 15 minutes
6. Remove the supernatant carefully
7. Resuspend the pellet in 40 μL of PBS
8. Repeat steps 7 and 8 once and resuspend in 20 μL PBS

note: MES buffer could be used in the place of sodium acetate buffer.

Appendix C: Labeling of lambda DNA with two microbeads

This protocol utilizes previously prepared lambda DNA labeled with digoxigenin on one end and biotin on the other end. Antidigoxigenin-coated nonmagnetic microbeads (see Appendix B) are attached to one end and streptavidin-coated magnetic microbeads (Dynabeads® M280, cat. no. 11205D) are attached to the other.

1. Wash Streptavidin-coated M280 beads in 0.5×TE buffer
   (a) Vortex beads and remove 1 μL
   (b) Combine with ∼20 μL 0.5×TE
   (c) Spin for 1-2 minutes on centrifuge
   (d) Rotate tube 180 degrees, spin for 1-2 minutes
   (e) Gently remove supernatant immediately after the spin
2. Add 20 μL 0.5×TE, spin 1-2 minutes again, and remove supernatant again
3. Resuspend in 20 μL 0.5×TE.
4. Prepare lambda DNA
   (a) Remove from freezer and allow DNA to thaw
   (b) Mix thoroughly: pipette in and out for 3-5 minutes
   (c) Test DNA on nanodrop UV-Vis spectrophotometer (3x) for concentration. Record average reading and calculate amount to add from this concentration (suggested values shown below)
5. Combine the 20 l 0.5 x TE and 1 μL beads from the previous step with 2 μL DNA at 2.9 ng/μL and 1 μL NaCl (2M in 0.5xTE)
6. Gently pipette in and out several times
7. Incubate at room temp in rotisserie for ∼30 minutes.
8. Vortex and add 4 μL antidig-coated beads in 0.5×TE (see Appendix B)

9. Incubate at room temp in rotisserie for ∼30 minutes.

10. Refrigerate on rotisserie to reduce clumping